A draft report on
Issues and challenges for polarimetric measurement of weather with an agile-beam phased array radar

(D. S. Zrnic, V. M. Melnikov, and R. J. Doviak)

Preamble

This report is about technical issues concerning agile-beam phased array radars for weather observation. Specifically we draw parallels with the performance of the polarimetric WSR-88D, the radar of the US National network which in due time will need replacement. The replacement, when it arrives, must not degrade any of the performance measures of the network at the time of replacement and must offer significant additional advantages for the observation of weather. The Multifunction Phased Array Radar (MPAR) is being considered for fulfilling the need of the FAA, NOAA/NWS and possibly Homeland Security. Therefore industry will soon be engaged to participate in preparatory work towards MPAR solutions and/or studies of alternatives. This "draft report" has been posted to alert the commercial sector about intricacies of weather observations. Although some of the material is available in formal publications it is indirect and more complicated to follow. Moreover, our thoughts on the MPAR topic have evolved since the publication of the said papers. This work reflects this evolution; it is a work in-progress and will be updated from time to time. This draft report is an outgrowth from a set of notes and tutorials aimed at consolidating our thoughts, guide our immediate priorities, and point out issues needing further inquiry. The authors are solely responsible for the content which does not represent official NOAA consensus on the subject. For explanations and other information you can contact Dusan.zrnic@noaa.gov or Dick.doviak@noaa.gov or Valery.melnikov@noaa.gov.

TABLE OF CONTENTS

1. Introduction

This is an update to the previous online report identifying challenges that weather observations present to agile beam polarimetric phase array radar. Some of the issues are highlighted and identified as subject study. This might help focus NSSL's engineers' work in this area. Also it should be beneficial to our partners in industry who are not very familiar with demands that polarimetric measurements of weather impose on phased array radars.

The phase array radar (PAR) with solid state transmitters and digital receivers can have tremendous flexibility in transmitter waveforms and in scanning strategy. In principle the radar could also offer great flexibility in polarization measurements. Of critical importance to dual polarization measurement is the type of radiating element and configuration of the phased array antenna (Section 2.4). Two types of dual polarization elements are under investigation. One is the electrical dipole type radiators which can be built as a pair of orthogonal conductors each with a voltage or current source. The electric field of the electric dipole type radiator is tangent to the meridian of the sphere in which the dipole is centered on the diameter connecting the poles. Two such orthogonal dipoles produce a field tangent to their respective meridians as depicted in Fig 1.1a. And it is clear that the E fields are orthogonal only in the principal planes. For clarity (and when needed) we will abbreviate these types of PAR antennas (and systems wherein the electric field resembles the one from a pair of dipoles) as PAR_{EE}.

The other radiator type is a parallel combination of magnetic and electric dipoles for which the electric fields are orthogonal in all directions from the source (Fig. 1.1 b); it will be designated as PAR_{EM}. The magnetic dipole's electric field lines are represented by the parallels (longitudinal circles) on a sphere whereas the electric dipole's field lines are represented with the meridians. Magnetic dipoles are approximated, for example, by slots in a waveguide (slotted). More detailed discussion about electric and magnetic dipoles for use as polarimetric array antenna elements and their simulated performances are given in section 2.4.1.
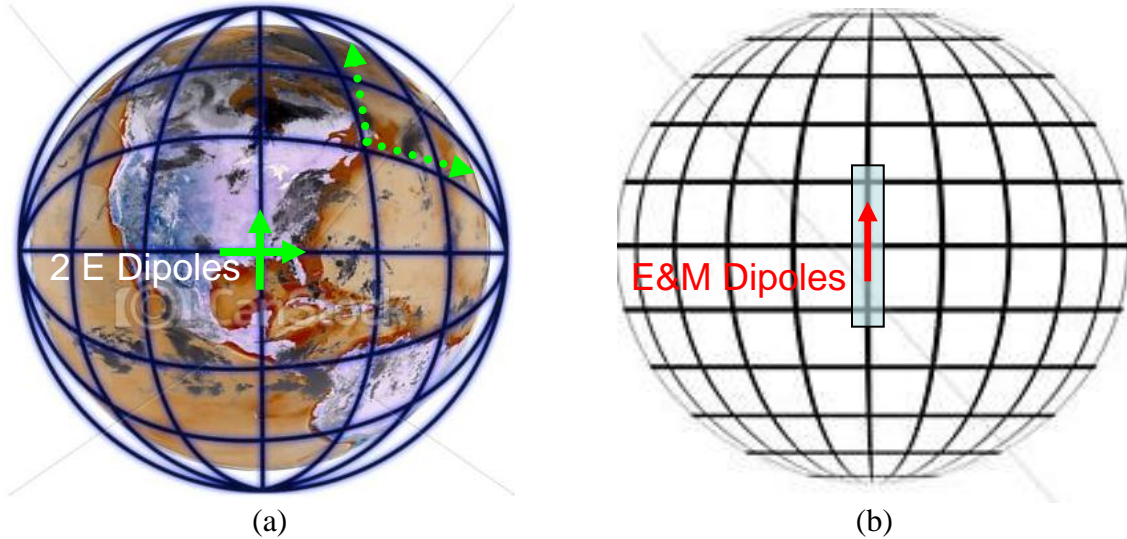
Fig. 1.1 a) Two crossed electric dipoles and the electric field lines (blue great circles) they produce. The electric fields are tangent to the lines and orthogonal to each other in the principal planes (i.e., the equatorial and meridional planes). Dotted lines illustrate the non orthogonality of the fields outside of the principal planes. b) An electric dipole is collinear with a magnetic dipole (orientation of both is marked with the red arrow). The magnetic dipole is built as a slot in a conducting surface (represented with the rectangle) and the electric dipole is in front of the slot.

Cylindrical antennas with orthogonal electric dipoles as radiators also produce orthogonal electric fields everywhere and this configuration will be abbreviated with PAR$_{CYL}$. PAR without subscript will be used in general discussions and technical descriptions where the type of radiators and planar vs cylindrical configurations are not critical. Combination of magnetic and electric dipoles is under development by Lockheed Martin and Basic Commerce Industries (BCI) companies. Cost of these radiators is considerably higher. Cylindrical phased array antennas with electric dipole (or patch, slots etc.) radiators and step beam steering (by commutating) would produce orthogonal electric fields in all directions. This type of PAR is being explored by University of Oklahoma engineers.

Of critical importance to any PAR antenna is the isolation between the copolar H and V fields (i.e., E_ϕ, E_θ in the spherical coordinate system centered on the radar and with a vertical polar axis), and their respective cross-polar radiation (amplitude and phase). To define the cross-polar field we use definition 2 of Ludwig (1973). With this definition the spherical coordinates remain fixed at the antenna location as the antenna rotates, or the PAR beam is steered. For example, if the H port of the antenna is excited, the copolar field everywhere is defined as the H (i.e., E_ϕ) component, and the cross-polar field is the V component (i.e., E_θ) everywhere. The economically achievable level of cross coupling will likely dictate a preferred mode for polarimetric measurement on the PAR.

On weather radars with parabolic reflector antennas two modes of polarimetric measurements have been employed. The AHV mode refers to alternate transmission and simultaneous reception of Horizontally and Vertically polarized fields and it was the

option typically used in the early days of weather observations with polarimetric radar. Isolation requirements for the AHV mode are much less stringent than for the SHV (i.e., Simultaneous transmission and simultaneous reception of H and V; Zrnić et al. 2010, Galletti and Zrnić 2011), and compensation of coupling is relatively simple to achieve. But in the AHV mode Doppler measurements are coupled with polarimetric measurements and dwell times are longer than for the SHV mode (Zrnić et al. 2011). The PAR_{EE} could use the SHV mode in directions where coupling is minimal and AHV mode elsewhere. Moreover, the radar could transmit single polarization to acquire only Doppler and reflectivity which could be interleaved with dual polarization data acquisition. With adaptive scans and pulse compression (Sections 4.2 and 4.3), very quick probing of weather over most of the observation space should be possible. But regions with ground clutter constrain the speed of volume scans. Superior clutter filtering as on the WSR-88D requires uniform PRTs and ample dwell time. A study is needed to determine if spatial filtering (feasible on the PAR but not on the WSR-88D) combined with shorter dwell time could lead to performance as good as presently obtained with the WSR-88D. We set aside the clutter issue for special consideration and examine other aspects of rapid scanning.
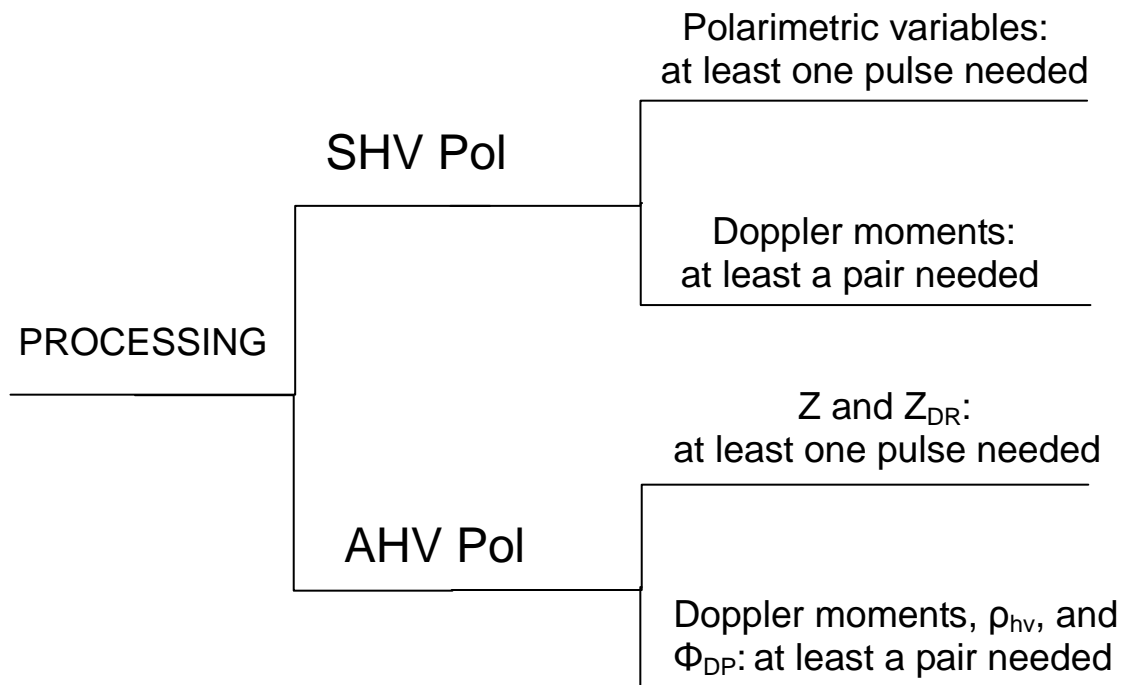
Fig. 1.2 Conceptual flow chard of processing possibilities for a planar antenna PAR.

Figure 1.2 illustrates some processing options which might be available on a PAR system and explanation follows. Suppose SHV is used. Then the Doppler variables (velocity and spectrum width) are decoupled from the Polarimetric variables (Z, Z_{DR}, ρ_{hv} and Φ_{DP}). Therefore, it would be possible to estimate all four polarimetric variables from a single return using pulse compression techniques to increase the number of independent

samples. For estimating the Doppler variables at least a pair of pulses is needed. In the AHV mode the Doppler variables are coupled with the correlation coefficient hence for these at least a pair of returns of each polarization is needed. The Z and Z_{DR} can be estimated from a single pulse alternately transmitted in each polarization. Mitigating range/velocity ambiguities in SHV mode would be different than in the AHV mode. Principal point derived from Fig. 1.2 is that under favorable conditions (no clutter) all polarimetric variables can be estimated from single H, V echoes using the SHV mode of data acquisition, whereas in the AHV mode only Z and Z_{DR} can be so estimated. This motivates us to examine estimation of the returned power using a single transmitted pulse and the Doppler spectral moments using two transmitted pulses (Sections 4.2, 4.3). Obviously such estimates are obtained in the fastest possible way. Other complexities (for R/V mitigation, clutter filtering) would add to the acquisition time and the increase is a good metric for comparing various schemes.

2. PAR Technologies and Issues for the Surveillance of Weather

2.1 Introductory remarks

The WSR-88D has provided acceptable measurements of hydrometeors' reflectivity, radial velocity, and spectrum width (i.e., a measure of differential motion related to turbulence and shear), and research continues to improve the estimates of these parameters and to provide reliable display of these parameters free of clutter and ambiguities. The WSR-88D should, with the upgrades to the dual polarimetric mode of operation now being implemented on the network of WSR-88Ds, provide better interpretation of the type of precipitation (i.e. snow, rain, hail, etc.), and should improve the accuracy of precipitation fall rates.

It is likely the WSR-88D will continue to provide high quality data for at least the next couple of decades. Nevertheless, the infrastructure to provide continuous support of the WSR-88D technology (e.g., single high-power klystron transmitter providing exceptionally coherent signals, and a mechanically steered beam formed by a reflector antenna) could be in jeopardy. For example, the phased array radar (PAR) has been undergoing development and deployment by the military for past 40 to 50 years and is replacing the well-established 1950 radar technology that uses reflector type antenna and a single high-power transmitter. There are many reasons for this transition, but most important is the versatility of the PAR (e.g., rapid adaptive scanning), and its reliability (i.e., phased array antennas accommodate distributed low-power solid state transmitters lessening the reliance on a single high-power transmitter). Single point failures for the PAR are typically not as catastrophic as that for radars using a single high-power transmitter chain. Furthermore, phased array antennas can allow replacement of parts while the system continues to operate with minor degradation of performance.

Another motivation for considering a PAR for weather surveillance is the potential to significantly decrease the updates (e.g., from the present 5 minutes to less than 1 minute) between scans of important weather events. Research suggests that short term numerical storm prediction can be improved if storms are scanned in times significantly less than 1 minutes (Heinselman and Torres, 2011; Zrnić, et al., 2007). Simulation experiments demonstrate assimilation of PAR observations at 1-min intervals over a short 15-min period yields significantly better analyses and ensemble forecasts than those produced using WSR-88D observations (Nusrat and Stensrud, 2010). Thus there is the potential to increase the tornado warning lead time beyond the present 10 to 15 minutes. Presently the lead time is about 12 minutes because it takes about six minutes for a volume scan and thus six minutes to return to the position of the first radar sighting of the tornado (two consecutive radar observations of tornado vortex signatures (TVS) are required before a tornado is confirmed to be observed). Beam-agile phased array radar has a definite advantage because the beam can return in seconds to the position of the first TVS detection to rescan the location. Hence more than 5 minutes can be added to the lead time of tornado warnings.

Although the military has extensive experience using hundreds of PARs for the detection and tracking discrete point targets dating back to the 1960s (e.g., Brookner,

1988, 2006) there has been little effort to apply PAR to the observation of weather. This is principally due to the high cost of the antenna, which is one of the most important elements of weather radar. The first steps in bringing PAR technology to the radar meteorology community began in the last years of the last century when Lockheed Martin Corp. integrated a weather processing data system to the AN/SPY-1A radar of the Aegis system [Brookner, 1988] and compared storm data collected at sea with that simultaneously observed with a coastal WSR-88D (Mease et al. 2001).

Next the National Severe Storms Laboratory (NSSL) acquired, on loan from the Navy, an agile-beam phased-array antenna, having phase-phase electronic beam steering in azimuth and elevation, for weather radar research to explore advantages that might be derived from phased array technology . This antenna is one face of the four-face antenna used with the AN/SPY-1A radar. With collaboration of Lockheed Martin, the principal contractor of the AN/SPY-1A radar, this antenna has been mated to a WSR-88D weather radar transmitter modified to match the operational band of the antenna. Because the beam can only be electronically steered over a $\pm 45^o$ azimuth angle relative to broadside, the antenna is mounted on a turntable which allows the broadside to be mechanically steered to any azimuth relative to north. This phased array weather radar is now the National Weather Radar Testbed (NWRT). In 2007, the NSSL brought this large aperture PAR weather radar into operation to evaluate the performance advantages of PARs for observing weather (Heinselman, et al., 2008; Heinselman and Torres, 2011). Some advantages of a PAR for weather surveillance are listed in Table 2.1.

Table 2.1 POTENTIAL ADVANTAGES OF AGILE-BEAM PHASED ARRAY RADAR

1) MUTI-MISSION APPLICATIONS
2) FASTER UPDATE RATES
3) EFFICIENT USE OF THE RADIO SPECTRUM
4) GAPS IN COVERAGE AT HIGH ELEVATION ANGLES CAN BE FILLED
5) BETTER GROUND CLUTTER CANCELLING and COMPENSATION
6) EFFECTS OF BEAM BLOCKAGE CAN BE MITIGATED
7) NO BEAM BROADENING EFFECTS DUE TO A SCANNING BEAM
8) RESOLVING SHEAR AND TURBULENCE
9) SUPPRESSING MOVING GROUND AND SEA CLUTTER
10) RESOLVING INDIVIDUAL OBJECTS
11) LOWER SIDELOBE LEVELS

Multi-mission applications: Because, a phased array antenna can accommodate more than a single transceiver and have two or more independent beams, one for each transceiver, a multiple beam PAR can accommodate multiple missions (i.e., a Multi-mission PAR; MPAR) such as the surveillance of weather and en route aircraft as well as to detect and track non-cooperative aircraft over the U. S. (Weber, et al., 2007, Zrnić et al., 2007). Two MPAR networks are being considered; one having large apertures for long range surveillance of aircraft (both cooperative and non-cooperative aircraft; principally an FAA responsibility) and weather (principally a NOAA/NWS responsibility), and a second network of smaller aperture MPARs for the observation and

tracking of aircraft in the terminal areas, and for the monitoring of weather hazards (both principally a FAA responsibility) to the safety of flight in the approach and departure corridors (Cho and Duffy, 2011). The replacement of a multiple network of radars with two MPAR networks could result in a 36% potential reduction in the number of radars in the U.S.A. When MPAR capabilities are compared with those of conventional radar technology, the technical advantages of MPAR are substantial.

Faster volume coverage: MPAR has the potential for considerably faster updates because the four-faced planar array as envisaged in publications (Weber, et al., 2007; Zrnić, et al., 2007) is actually eight radars at one site all sharing the common four-faced planar array. Each face of a four-faced planar array is served by a pair of transmitters and receivers; one for aircraft surveillance and another for weather. Because the beam-agile PAR can steer the beam direction as rapidly as the PRF, the PAR, further reduction in scan time for weather observations can be achieved in directions where ground clutter is not a problem (clutter cancellation typically requires a stream of contiguous transmitted pulses). In those directions where clutter is insignificant, beam multiplexing (BMX) can be implemented to obtain the fewer independent samples needed to estimate Doppler and polarimetric parameters of weather signals (Yu, et al. 2007). Some of these techniques and other high-temporal resolution capabilities of the PAR are presented in Heinselman and Torres (2011). Perhaps more importantly, localized regions of significant weather (e.g., regions of significant circulating air that can generate tornadoes) can be scanned more often to improve warning performance.

On the other hand, tornadoes and other intense small scale phenomena are driven by larger scale moisture, wind, and temperature fields. Thus longer lead times of significant weather might be better derived by combining the multiple scans of the larger scale phenomena (e.g., mesoscale cyclones), observed with larger temporal spacing (e.g., on the order of a minute vs. seconds needed to observe the rapid changes taking place in a tornado), and combining radar observations with numerical models to predict the evolution of significant small scale weather hazards.

Efficient use of the Radio Spectrum: A PAR could require less bandwidth than other rapid scan approaches such as those using a multi-beam multi-frequency radar (e.g., Brookner 1988, p.54; Wurman and Randall 2001), or ultra wide band transmissions to increase the number of range samples. On the other hand, in order that radiation from one face does not interfere with operation of another face, a four-faced PAR might require more than one frequency for each mission. Thus a MPAR might require a larger frequency allocation than the present surveillance radars that use a single frequency for each mission. Alternatively, synchronized beam scanning might not require any additional frequencies because beams can always be orthogonal to each other. This approach would then sacrifice the beam multiplexing capability inherent to the beam-agile PAR, but would be mimicking the present capabilities of surveillance radars, but at a faster update rate.

Closing data gaps: Gaps in weather surveillance at higher elevation angles that are imposed using the WSR-88D can be mitigated or eliminated because the PAR's beam width naturally increases at higher elevation angles where high angular resolution is not required for weather surveillance. Furthermore, the PAR's aperture distribution can be modified to increase the beamwidth, at high elevation angles, and thus PAR can eliminate gaps in coverage. If sensitivity and resolution is not a significant issue (typically at higher

elevation angles and in stratiform weather), broader beams can be transmitted and multiple beams with full angular resolution on reception can acquire data at faster update rates.

Better ground clutter cancelling: Canceling ground clutter presents a formidable obstacle to rapid scans by any type of radar. An inherent advantage of the PAR is the antenna beam is stationary during a dwell time, and therefore there is no increase in spectrum width due to beam scanning. Although the spectrum width of clutter is smaller for the PAR, it is not necessarily much smaller under windy conditions (Curtis 2009, Fig. 2.27). By using a judicious combination of spatial and temporal filters, the agile beam PAR might reduce the dwell time normally required to achieve adequate ground clutter suppression if only a temporal filter is used. Furthermore, a PAR can form a different receive beam pattern at each range gate, something completely out of reach by radars using parabolic reflector antennas. That is, the two-way antenna field pattern of a PAR can be expressed as

$$f^2(\theta, \phi) = f_t(\theta, \phi) f_r(r, \theta, \phi)$$

where the subscripts t and r refer to the pattern on transmission and reception. Finally, techniques such as multi-pattern measurements (Zhang et al. 2011a) have been applied to improve the suppression of non-weather clutter, especially clutter associated with moving scatterers such as vehicles, aircraft, and airborne biological scatterers.

Beam blockage mitigation: Effects of beam blockage can be mitigated using the PAR as noted by Zhang et al., (2012). Thus further efficiency in using radar resources is obtained by not collecting data in regions where the beam is blocked.

Beam broadening: Use of a PAR for weather surveillance eliminates the effective increase in azimuth beam width due to beam scanning as shown in Doviak and Zrnić (2006, section 7.8). On the other hand, the beam width of a planar PAR is a function of beam direction and a larger aperture would be required to match the present WSR-88D's angular resolution when the PAR beam is directed azimuthally far (e.g., 45°) from the broadside. Beam width of a cylindrical PAR does not change as a function of azimuth (Zhang et al., (2010).

Resolving shear and turbulence: Under some simplifying conditions, shear and turbulence can be separated using the flexibility the array elements can have in controlling the aperture distribution (Zhang and Doviak, 2007).

Suppressing moving clutter: Because scatterers on the sea surface do not uniformly fill the radar's resolution volume V_6 (Doviak and Zrnić 2006, Section 4.4.4), the capability to control the aperture distribution can be used to detect moving clutter (Zhang et al., 2011a), such as sea clutter, so that a cancellation method can be implemented.

Resolving locations of individual objects: The theory of spaced-antenna interferometry (SAI) has been formulated to detect and locate deterministic objects and reflectivity inhomogeneity embedded within the phased-array weather radar's resolution Volume (Zhang and Doviak, 2008). There is an analogy between monopulse tracking of airborne objects for aviation and missile defense application and SAI used in studies of the atmosphere (Fukao and Hamazu, 2013).

Lower sidelobe levels: Blockage of radiation by feed support spars is eliminated using PAR, and thus ridges of enhanced sidelobe levels are no longer present. However, these sidelobe ridges occupy only a small solid angle and are not necessarily as important as the sidelobes outside the ridges. WSR-88D two-way sidelobe levels (two-way

sidelobes are a matter of importance for weather observations) outside the ridges are shown, through theoretical computations and measurements, to be about 100 dB below the peak of the beam (Doviak and Zrnic, 1998). On the other hand sidelobe levels of a PAR can be significantly larger than theoretically calculated if phase shifters do not meet specifications. Phase shifter errors are analogous to surface distortions in a parabolic reflector antenna, and need to be carefully controlled.

Although the advantages of a PAR appear compelling, the weather community expects not only to have the advantages offered by a PAR, but to retain all of the present capabilities of the polarimetric WSR-88D (Smith et al., 2008; Zrnić et al., 2007). Therefore, before a decision is made between continuing with single-mission radar networks or to upgrade to a network of MPARs, some specific technical issues need further testing to demonstrate that the needs of the NWS and FAA can be met with a polarimetric MPAR. Some of these technical issues for the observation of weather are addressed in this report.

2.2 Considerations for the use of PAR to observe weather

Over the last 50 years, the biggest improvement to weather radars has come from the use of coherent klystron transmitters (i.e., for high quality Doppler measurements, ground clutter filtering, and ambiguity resolution), signal processing, digital receivers, and upgrades to dual polarimetric operation, but the antenna and transmitter remain much as it has been for the last 50 years.

Yet, given the extensive development of phased array technology, and its successful implementation by the military, it has yet to be proven that phased array technology can meet, at an acceptable cost, the rigorous demands of present and pending (i.e., polarimetric) weather measurements made by the network of WSR-88Ds. It is the very nature of weather signals that imposes limitations and tradeoffs. Weather signals easily span 80 dB of echo power at the same range, and because signals are random, quantitative results (i.e., precipitation rates, Doppler velocity, etc.) cannot be obtained from one or two echo samples (no matter how high is the signal to noise ratio), but typically require tens of samples. This constrain is imposed by the strong amplitude and phase fluctuations that are characteristic of echoes from precipitation. Significantly less number of transmitted pulses would be required and faster scan rates would ensue if bandwidth limitations were not imposed on the weather radar. But a large number of samples (i.e., long dwell times of the order of 50 ms) are yet required to filter ground clutter, and to resolve range and velocity ambiguities. Furthermore, because weather is distributed quasi-continuously over large spatial regions (from tens to hundreds of kilometers), measurements need to be made at millions of locations in a few minutes or less.

Furthermore, to meet meteorological requirements, the weather radar is designed not only to detect weather but to make accurate and unambiguous measurements of the reflectivity factor Z, mean radial velocity v of the precipitation particles within V_6, and the variation of particle motion (i.e., due to turbulence and/or shear) about this mean. High quality polarimetric measurements for quantitative precipitation data also impose additional strict requirements on the accurate and reliable estimates of multiple polarimetric parameters (e.g., differential reflectivity, Z_{DR}, copolar correlation coefficient magnitude ρ_{hv}, and specific differential phase $K_{DP,}$ etc.; Doviak and Zrnic, 2006). These

polarimetric parameters are calculated from measurements of the horizontally and vertically polarized backscatter from hydrometeors illuminated (either alternately or simultaneously) with horizontally and vertically polarized waves (Doviak et al., 2000).

2.2.1 Accuracy requirements for weather measurements

The polarimetric variables: Z_{DR}, $K_{DP,}$ and ρ_{hv} represent differences in the amplitude and phase of the horizontally (H) and vertically (V) polarized backscatter from hydrometeors. The differences, however, are usually very small because the scatterer's axis ratio, for example of the typically oblate rain drops, is not too different from unity. High measurement accuracy is therefore required to provide meaningful information for hydrometeor classification (i.e., rain, snow, hail, etc.) and quantitative estimation of precipitation fall rates. For example, the measurement error for Z needs to be less than 1 dB, Z_{DR} needs to be estimated within 0.1 dB (Sachidananda and Zrnić 1985; Zrnić et al. 2010), and the error of ρ_{hv} measurements should be less than 0.005. These are big challenges for phased array radar because the respective H and V polarized beam patterns could be unmatched when the beam is directed away from broadside. The unmatched beam patterns for H and V is due to the differences in the elemental radiation patterns for the H and V antenna elements. This mismatch can cause bias errors larger than the specified accuracies for polarimetric measurements such as the copolar correlation coefficient and the differential reflectivity. Only aligned electric and magnetic dipoles have radiation patterns that match for all beam directions. In that case the H and V electric field ratio is independent of pointing direction although the antenna gain will vary with beam direction.

Therefore, it is important to understand the principle of phased array polarimetric radar for weather measurements in order to quantify the polarization characteristics of the radar and hydrometeors so that high quality, useful data are available to meteorologists. To meet accuracy and reliability requirements, weather radars must be continuously calibrated, and phase measurement need to be accurate to a degree or less. For example the WSR-88D self-calibrates every volume scan, and the stability of the transmitted signal is such that phase noise is less than 0.2^{o} (Zrnić and Doviak 2005). Fig.2.1a shows the spectrum of echoes from a tower that illustrates the corresponding spectral noise floor is about 70 dB below the carrier of a WSR-88D (KOUN; the first WSR-88D having polarimetric capability) transmitter. Such low phase noise is critical to mitigate range and velocity ambiguities using phase coding and Staggered PRT methods, and in achieving 50 dB of ground clutter cancellation. Other requirements placed on the PAR for weather observations, and further discussions, are given in the NSSL report by Zrnić and Doviak (2005). Calibrating the PAR beam needs to be done for every direction of observation; this is a challenging problem.

The low phase noise of the WSR-88D transmitter has also been observed (Fig.2b) by Curtis (2009) on the NWRT which has a WSR-88D transmitter feeding an array of 4480 elements of a 3.7 m diameter phased array antenna. Not only does Fig.2b show the phase noise floor also to be about 70 dB below the carrier, these measurements with the NWRT also show the broadening of a clutter spectrum due to a simulated beam scanning a ground target. The NWRT is the first large aperture ground-based phased-array radar available for weather radar research. Here a scan rate of only $0.5^{o} \, s^{-1}$ was simulated using the electronic beam steering capability of the NWRT; the faster scan rates of about $20^{o} \, s^{-1}$

13

for the WSR-88D beam will show even more significant change especially in broadening the spectrum at the higher levels of spectral power. Thus it is expected the PAR will have better capabilities for ground clutter cancelling and for the mitigation of ambiguities.

The implementation of polarimetric weather measurements imposes stricter requirements on the antenna's performance to attain quantitative precipitation measurements and to classify precipitation types. This is even a more significant problem for the antenna of a Polarimetric PAR (PPAR) that has thousands of beams, of varying gain and beam width, each of which require precise calibration. Among the most critical antenna specification is having low cross-polar fields (Zrnić et al., 2011). It is the polarimetric capability that the 2nd MPAR Symposium (http://www.ofcm.noaa.gov/mpar-symposium, 17-19 November, 2009) identified as the most challenging technical issue for future Multi-mission Phased Array Radar (MPAR) for which the surveillance of weather is one function.
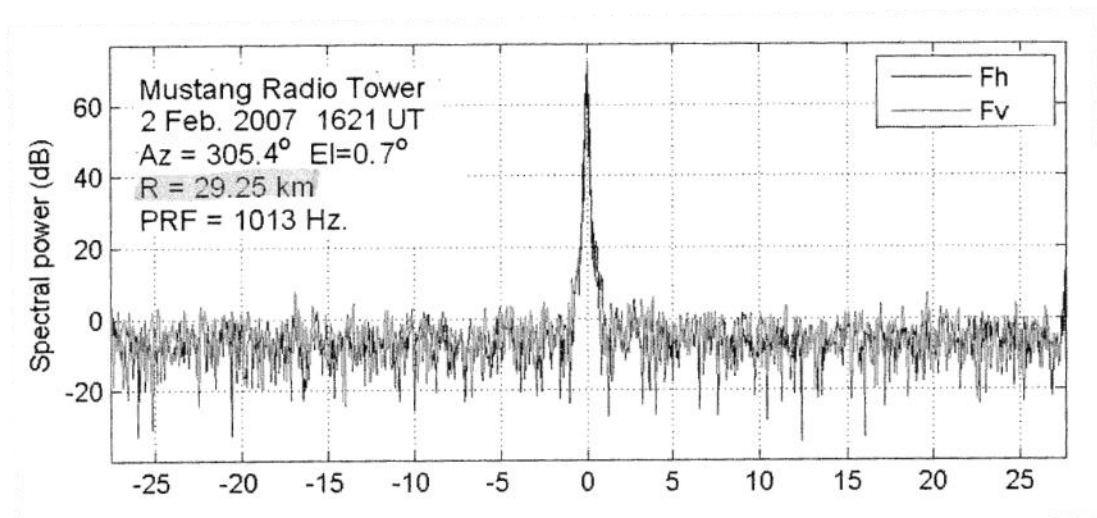

Fig.2.1a Power spectrum of horizontally F_h and vertically F_v polarized echoes from a radio tower illuminated with WSR-88D (KOUN) radiation. Antenna is not rotating, and the abscissa is the radial velocity in m s^{-1}.
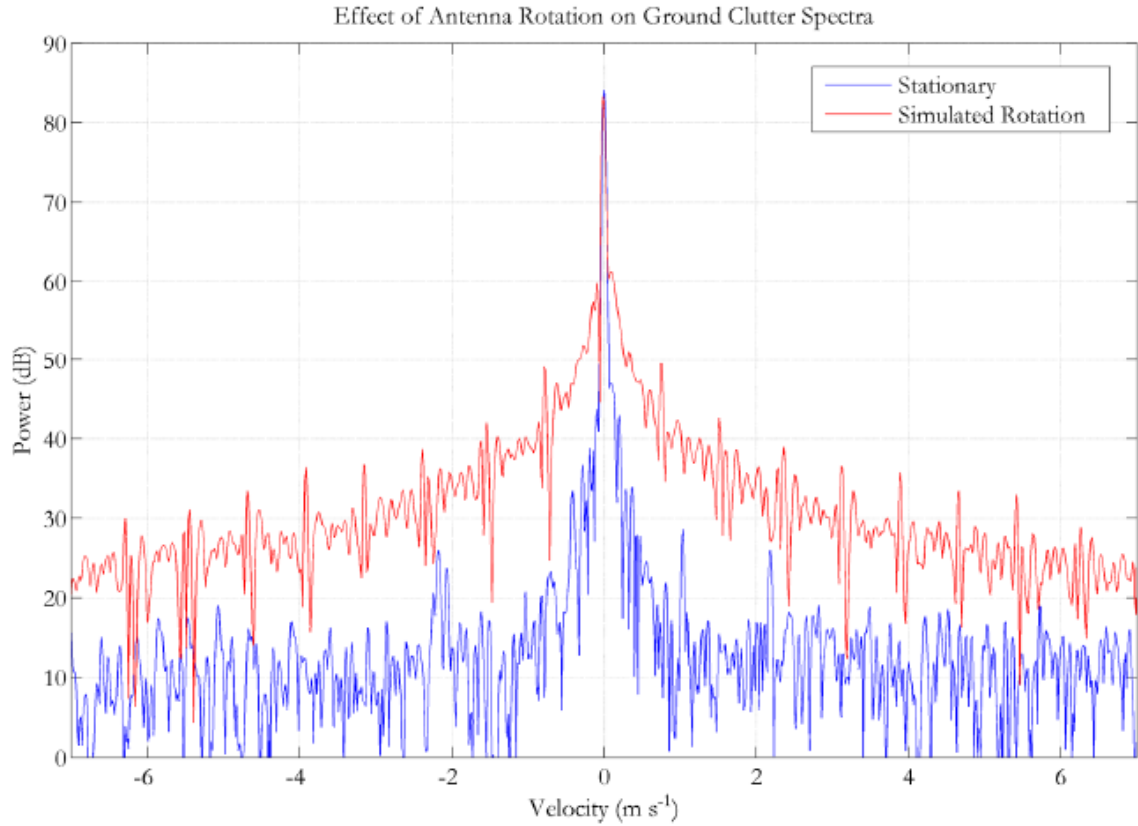
Fig.2.1b The power spectrum of clutter observed with NSSL's 3.7 m diameter PAR (i.e., the NWRT) for ground objects illuminated with a fixed beam (lower trace) and with a scanning beam (angular rate of 0.5° s^{-1}).

2.2.2 Cross-polar radiation requirements for weather radar antennas

Accurate polarimetric measurement has two principal purposes: (1) to classify types of precipitation and (2) to provide quantitative estimates of precipitation accumulation. But accurate estimates of precipitation accumulation imposes strict requirements on the required accuracy of polarimetric parameter estimates. For rain rates as high as 10 mm h^{-1} the following relation (Ryzhkov et al. 2005a),

$$R = \frac{1.70 \times 10^{-2} \, Z_h^{0.714}}{0.4 + 5.0 \, | \, Z_{dr} - 1 \, |^{1.3}} \quad \text{(mm h}^{-1}\text{)}, \tag{1}$$

has been used where Z_h is the reflectivity factor in units of mm^6 m^{-3}, and $Z_{dr} = 10^{0.1 Z_{DR}}$ where Z_{DR} is the differential reflectivity in dB. This equation and Fig.8.23 of Doviak and Zrnić (2006) suggest Z_H can be as large as 40 dBZ and Z_{DR} as large as 1 dB. Comparisons of Z_H and Z_{DR} for rain measured by radar and that calculated from disdrometer measurements also suggest Z_{DR} is mostly less than 1 dB if Z_H is about 40

15

dBZ or less (Brandes et al. 2003). Thus it has been shown that Z_{DR} bias needs to be less than 0.1 dB to keep the rain rate bias less than 15% (Zrnić et al., 2010).

Z_{DR} larger than 1 dB and Z_H larger than 40 dBZ imply higher rate rates, and therefore (1) cannot be used. At moderate rain rates (i.e., $10 < R < 50$ mm h^{-1}), two polarimetric parameters (i.e., Z_{DR} and specific differential phase K_{DP}) are used to measure rain rates with radar (Ryzhkov et al. 2005a). However, it can be shown that the relative error in rain rate is larger for light rain rates. Therefore, attention here is focused on accurate estimates of differential reflectivity of light rain.

The level of differential reflectivity bias depends strongly on the patterns and intensity of the copolar and cross-polar radiation emitted by the antenna, as well as the mode of data collection. There are two data collection modes that are commonly used by weather radars having a dual polarimetric capability; 1) SHV (Simultaneously energizing the H and V antenna ports on transmit, and simultaneously receiving H and V backscatter radiation) and 2) AHV (Alternately energizing the H and V antenna ports on transmit, but simultaneously receiving echoes). Operation in the AHV mode, popular among weather radar researchers, allows measurement of all polarimetric parameters. But the SHV mode is used operationally by the NWS's WSR-88D primarily because of practical considerations (Section 2.2.3 discusses comparison of SHV and AHV attributes).

Operation in either of these modes can produce biased Z_{DR} estimates, but data collected in the SHV mode is more susceptible to bias due to cross-polar radiation. Bias is a more significant error than zero mean random errors that can be spatially averaged to increase precipitation rate accuracy. If the SHV data collection mode is used, it has been shown (Zrnić et al., 2010) Z_{DR} bias in dB is given by

$$\delta Z_{DR} = 10(A_1 + A_2)\log e \text{ (dB)} , \tag{2a}$$

where,

$$A_1 = \frac{2\int_\Omega F_{hh}^3 \text{Re}\{F_{hv}e^{j\beta} - F_{vh}e^{-j\beta} + \rho_{hv}[e^{-j\Phi_{DP}}(Z_{dr}^{-1/2}F_{vh}^*e^{-j\beta} - Z_{dr}^{1/2}F_{hv}e^{-j\beta})]\}d\Omega}{\int_\Omega F_{hh}^4 d\Omega} , \tag{2b}$$

$$A_2 = \frac{\int_\Omega F_{hh}^2 \left\{ \begin{matrix} |F_{hv}|^2 - |F_{vh}|^2 + Z_{dr}^{-1}|F_{vh}|^2 - Z_{dr}|F_{hv}|^2 + \\ 2\rho_{hv}\text{Re}\{e^{-j\Phi_{DP}}[Z_{dr}^{-1/2}(F_{vh}^{*2} + F_{hv}F_{vh}^*) - Z_{dr}^{1/2}(F_{hv}^2 + F_{hv}F_{vh}^*)]\} \end{matrix} \right\}d\Omega}{\int_\Omega F_{hh}^4 d\Omega} \tag{2c}$$

The term A_1 contains integrals of F_{hv} to first order and A_2 contains the integrals of F_{hv} to second order. F_{hv} (or F_{vh}) is the horizontally 'h' (or vertically 'v') polarized electric field pattern (i.e., the cross-polar field intensity as a function of the zenith and azimuth angles) if only the vertical 'V' (or horizontal 'H') port of the antenna is energized to transmit vertically (or horizontally) polarized fields (i.e. the copolar field). F_{vv} (or F_{hh}) is the

copolar pattern when the V (or H) port is energized ($F_{vv} = F_{hh}$ was assumed in deriving Eq. 2). Note for a PAR, the field patterns F_{hh}, F_{hv}, etc. change as a function of beam direction whereas for the conventional parabolic reflector antenna used with the WSR-88D, these patterns remain independent of beam direction. This complicates enormously the calibration because there the PAR has thousands of beams that require calibration.

For weather radar the electric field $\vec{E}$ radiation is principally vertically polarized (i.e., E_θ in a spherical coordinate system having the polar axis vertical) if the vertical port V is energized to form a transmitted V copolar field along the beam axis. "Vertically" polarized means the electric field vector lies in the vertical plane. In this case (i.e., the V port is energized) the horizontally polarized field (i.e., E_ϕ) is defined as the transmitted cross-polar field (Balanis, 2005, p.72). Likewise, if the H antenna port is energized, the horizontal field (i.e., E_ϕ) is the copolar field and the "vertical" field component (i.e., E_θ) is the cross-polar field.

For weather radar using a center-fed parabolic reflector antenna, as for the WSR-88D, the cross-polar radiation along the beam axis is always H if the V port is energized and vice versa. *This is not necessarily so for the electronically steered beam of a PPAR* because the orientation of intended "H" or "V" fields (i.e., the fields when the H or V ports or elements are energized) depends on the radiation pattern of array elements and the pointing direction. For example, a horizontal dipole will produce a vertical component in directions outside the principal planes. To have purely V or H polarized waves along the electronically steered beam when the beam is steered away from the principal planes, both ports might need to be energized. Otherwise both H and V waves could be present along the beam axis if only one of the ports is energized. In either case, more complex data processing techniques are required to retrieve the intrinsic polarimetric parameters when using a PAR (Zhang et al., 2009, Zrnić et al., 2011).

An ideal center fed parabolic reflector antenna has no cross-polar radiation along its beam axis, irrespective of the beam direction or the port being energized. However, if one port of a PAR (e.g. the V port) is energized, substantial cross-polar H radiation can be generated along the beam axis for most array elements if the beam is steered away from the principal planes as shown in Section 2.3.2. Although an ideal parabolic reflector antenna has no cross-polar radiation along its beam axis, imperfections in manufacture of the feed horn, errors in mounting it, and imperfections in the parabolic reflector can cause cross-polar radiation along its beam axis. But even if these errors did not exist, cross-polar radiation is still emitted, albeit in directions other than the beam axis, by the center-fed parabolic reflector.

For a center-fed parabolic reflector, four principal cross-polar lobes of radiation with peaks approximately 35 dB below the copolar peak are symmetrically located around the copolar beam axis, and are displaced nearly a beamwidth from the axis (Zrnic et al. 2010). Although there might not be cross-polar radiation along the beam axis, there is still cross-polar radiation within the beam as well as outside the beam. Because Z_{DR} bias is related to the integral of the product of copolar and cross-polar beam patterns (i.e., Eq.2), there will be, in general Z_{DR} bias even if there is no cross-polar radiation along the beam axis. Although bias is a function of the copolar and cross-polar radiation integrated over the entire spherical surface, the most detrimental cross-polar radiation is that

contained within the copolar beam, especially if the cross-polar radiation has a peak along the beam axis.

For example, if cross-coupling within the antenna causes an on-axis coaxial cross-polar lobe of width equal to that of the copolar beam and with a directive gain 40 dB below the copolar peak, and if the SHV data collection mode is used (i.e., the mode used by the WSR-88D), it is shown differential reflectivity Z_{DR} bias can be as much as ± 0.35 dB for rain rates R ≤ 10 mm h^{-1} (Zrnić, et al., 2010). Such a large bias vitiates improvement in rainfall measurements that could be attained using polarimetric data. To keep the relative rain rate bias less than 15%, Z_{DR} bias needs to be less than about 0.1 dB.

Eq.2 shows bias is a function of propagation differential phase Φ_{DP}, and thus is range dependent. Furthermore, bias also depends on the relative phase β of the copolar H and V fields as well as the relative phase γ of the copolar and cross-polar fields. If cross-polar radiation has a lobe coaxial with the copolar beam, the requirement that Z_{DR} bias should be less than 0.1 dB places stringent limits on the cross-polar field. For example, using Eq.2 it can be shown the worst case Z_{DR} bias is obtained if $\beta = 90^{\circ}$ and $\gamma = 90^{\circ}$. In this case, the coaxial cross-polar peak needs to be 50 or more dB below the copolar peak to insure bias is less than 0.1 dB anywhere along the beam. If there is control over the relative phase β of the H and V transmitted signals, and if they can be adjusted so $\beta = 0^{\circ}$ or 180° (i.e., polarization is linear at a slant of 45° or 135°), the acceptable cross-polar peak can be increased to 45 dB below the copolar peak, a relatively small 5 dB improvement.

On the other hand, the largest relaxation in the peak level of a coaxial cross-polar lobe is attained if the cross-polar and copolar fields are either in or out of phase with each other (i.e., $\gamma = 0^{\circ}$ or 180°). In this case the peak level of the cross-polar radiation is relaxed to about 26 dB below the copolar peak, and the maximum Z_{DR} bias is independent of β ! The reason that the maximum bias is independent of β is due to the fact that β and Φ_{DP} are additive. Furthermore, because differential phase Φ_{DP} monotonically increases as the wave propagates through rain, there is little to be gained in potential bias reduction by transmitting slant 45° radiation. Although γ has significant effect over the limits on the cross-polar radiation (i.e., increasing the limit of the coaxial cross-polar peak by about 20 dB), it typically cannot be controlled because it is an intrinsic property of the antenna design, and the level of cross-polar radiation often depends on the accuracy in fabrication and assembly of the array. Furthermore, a cross-polar lobe coaxial with the copolar beam can be produced by reflection from the ground when the beam is pointing at low elevation angles.

In summary, only if coaxial cross-polar radiation is 45 dB or more below the copolar peak, and only if the H, V copolar phases can be adjusted so that a slant 45° polarized radiation is transmitted, will the worst case differential reflectivity bias be less than 0.1 dB, a level required to produce a maximum relative rain rate bias less than 15%. Nevertheless, this worst case situation is least likely to occur because it requires the juxtaposition of the cross-polar field to be in phase quadrature with the copolar field and the specific differential phase Φ_{DP} to be 0°; thus the 45 dB upper limit of coaxial cross-polar radiation could be relaxed a few dB (i.e., 42 or 43 dB might be a reasonable upper limit to insure Z_{DR} bias remain small for most all regions of precipitation).

Having cross-polar radiation along the beam axis to be less than 45 dB below the copolar peak typically requires a null in the cross-polar radiation pattern. Such a null is inherent in a well manufactured and assembled parabolic reflector antenna as the one on the WSR-88D. Measurements made on the WSR-88D antenna suggest a null of cross-polar radiation is present along the axis of the copolar beam (Zrnić et al. 2011). Furthermore, polarimetric measurements made with KOUN (i.e., NSSL's WSR-88D), operating in the SHV mode, show no significant evidence of a Z_{DR} bias in measurements of precipitation rates, suggesting there is not significant cross-polar radiation lobe coaxial with the copolar beam.

On the other hand, in the case of an ideal center-fed parabolic reflector of the type used by the WSR-88D, four equal amplitude principal cross-polar lobes appear. But these are in phase opposition in adjacent quadrants and displaced significantly from the copolar peak. In this case, as has been deduced (Zrnić et al. 2010) from Eq.(2), bias is significantly reduced. For example, even if the four cross-polar peaks are as large as 20 dB below the copolar peak, Z_{DR} biases are at acceptable levels. Such nulls of cross-polar radiation are only possible for a PAR if the cross-polar field for H or V antenna ports is zero everywhere the electronically steered beam is pointed as shown in Section 2.3.1

Because hydrometeors typically have a vertical axis of symmetry, and because of other significant attributes (Table 2.2), the SHV mode for polarimetric data collection is being implemented on the network of WSR-88Ds. The advantages of this mode are also applicable to a PPAR. However, for a PPAR antenna, obtaining such low cross-polar radiation along each of the thousands of copolar beams is a challenging task (Section 2.3), especially if cost of the antenna is a driver. If on-axis cross-polar radiation cannot be guaranteed to be 45 dB below the copolar peak, precise measurements of the amplitude and phase of the cross-polar field must be made for each of the electronically steered beam directions so that corrections can be made to remove Z_{DR} bias (Zhang et al., 2009, Zrnić et al., 2011). Off-axis cross-polar lobes are not as effective in biasing Z_{DR} because at those locations the copolar field is weak. Nevertheless, complete patterns of copolar and cross-polar amplitude and phase fields will have to be made on any PAR before the prototype design is accepted as a Polarimetric PAR for weather measurements.

But such strict control, or precise measurements of on-axis cross-polar radiation is needed only if the radar is operated in the SHV mode. An alternative mode of polarimetric data collection, the AHV mode can be used. In the AHV mode, the maximum Z_{DR} bias is less than $\pm 0.1 dB$ if the on-axis cross-polar radiation is no more than -22 dB below the peak of the copolar beam. But there some disadvantages (section 2.2.3) in using the AHV mode

Although the military has a lengthy experience with many types of PARs (Brookner 1988) there are far less PARs that have incorporated dual polarization technology, and cross-polar data for PAR is sparse. Because years of research and field programs have proven polarimetric radar has the capability to increase the accuracy for the nation-wide measurement of precipitation rates and to classify precipitation types, the NWS is upgrading the USA's network of WSR-88Ds to have polarimetric capability. Thus, a PAR with polarimetric capability is extremely important for weather observations.

Section 2.3 presents some phased array alternatives using 1D and 2D electronic beam steering that suggest cross-polar fields coaxial with the copolar beam, and more than 40 dB below the copolar peak, can be obtained along the principal planes of

radiation. If significant cross-polar radiation is present along the copolar beam of a PAR as the beam is steered from the principal planes, corrections will be necessary to remove biases in the estimates of polarimetric variables. For example, if the relative amplitude and phase of the cross-polar and copolar fields within the copolar beam is known, or can be measured accurately for each of the thousands of beams, Z_{DR} bias might be correctable, using the theoretical approach outlined by Zhang et al., (2009) and Zrnić, et al., (2011), to sufficient accuracy (i.e., $\pm 0.1 dB$) irrespective whether the SHV or AHV mode is used.

2.2.3 Relative Merits of the SHV and AHV modes of polarimetric data collection

As stated earlier, there are two approaches in the design of radar to implement polarimetric measurements (i.e., SHV and AHV). There are many reasons why the SHV mode was favored to be implemented on the WSR-88D and some of these are listed in Table 2.2. The most significant was to avoid using a costly and relatively unreliable high power ferrite switch, or to avoid using two high-power transmitters (one for H and the other for V). On the other hand, switching within a PPAR can be done at much lower powers and concerns of cost and reliability are strongly mitigated.

Table 2.2

Relative Merits of SHV and AHV

SHV:
- Smaller estimate errors
- A 360° unambiguous Interval for Φ_{DP} phase unwrapping
- Nyquist velocity v_a twice as large
- Decoupling of Φ_{DP} and Doppler velocity
- Direct measurement of ρ_{hv}
- No degradation of ground clutter filter performance
- Better mitigation of range/velocity ambiguities
- All signal designs and algorithms developed for the WSR-88D are directly applicable

• AHV:
- Better sensitivity (3 dB better)
- 20-30 dB suppression of 2nd trip echoes
- Fully Polarimetric
- Cross-polar radiation effects are smaller
- Effects due to depolarization during propagation can be corrected

Doppler spectral moment estimate errors can be smaller in the SHV mode because there are twice as many samples (i.e., H and V samples) per dwell time than are available in the AHV mode. But if H and V signals are highly correlated (i.e., $\rho_{hv} \approx 1$) as they typically are for backscatter from rain and snow, there is little to be gained by processing both the H and V signals to improve spectral moment estimates. Nonetheless, errors in polarimetric variables are smaller in the SHV mode (Section 3 and appendix A.2).

Polarimetric radar operating in the SHV mode has twice the unambiguous phase interval of radar operating in the AHV mode. This larger unambiguous interval considerably eases resolving aliased phase measurements of Φ_{DP}. Furthermore, the

20

decoupling of the Doppler and Φ_{DP} is much easier because the unambiguous phase interval for the SHV mode is 2π whereas for the AHV mode it is π. Although phase ambiguities of π can be resolved with help of phase continuity in range, often overlaid echoes disrupt the continuity of data and the resolution of phase ambiguities is more difficult to achieve with the smaller unambiguous phase interval.

Because there is no need to make any assumptions of the shape of the correlation function, estimates of the copolar correlation coefficient ρ_{hv} has less bias using data collected with the SHV mode, and errors in estimates are lower.

Another advantage of the SHV mode is that the clutter filter cancels weather signals only if the Doppler velocity of weather signals is at or close to zero or at twice the Nyquist velocity. The cancelling of portions of the weather spectrum creates undesired bias in the weather data field. But if the AHV mode is used the Nyquist interval is halved. In that case twice as many spectral coefficients are canceled and thus more of the weather data products (i.e., reflectivity, Doppler velocity, etc.) can be useless or biased. On the other hand, if a very effective ground clutter detection scheme is employed, the damage by the clutter filter to weather echoes would occur only if weather returns are mistaken for clutter or if weather and clutter overlap in the spectral domain.

The mitigation of range/velocity ambiguities is better accomplished using the SHV mode in conjunction with either the phase coding method (used at low elevation angles and with long PRTs) or the staggered PRT method (used at higher elevation angles and with pairs of shorter PRTs). This better performance is related to the fact that both methods resolve ambiguities in the spectral domain, and the separation of overlaid echoes has better performance using larger Nyquist velocities. In the case of the SHV mode the Nyquist velocity is proportional to the reciprocal of the PRT whereas for the AHV mode it is smaller by a factor of two. The presently used methods to mitigate range and velocity ambiguities, and those methods to cancel ground clutter based upon the larger spectral domain, afforded by the SHV mode, have been developed and extensively tested, and results are presented in a series of 15 Reports (NSSL 1997-2012) which can be found on the NSSL web site at nssl.noaa.gov.

After years of developing, testing, and evaluating the signal processing software for the SHV data, the National Weather Service is implementing the SHV mode of operation on its radars to acquire polarimetric data. On the other hand, research suggests acceptable results using the AHV mode with dual high-power transmitters (Brunkow, et al., 2000), or a single transmitter with a high-speed high-power mechanical switches (e.g., Randall, et al., 1997). Thus the AHV mode can be used with a PAR because it does not require high power switches or transmitters. But there will have to be changes to the signal processing software used by the NWS, whereas, none of the legacy signal processing software is affected using the SHV mode. That is, signal processing using data from either the H or V channels to get Doppler moments, resolve ambiguities etc., are the same. This signal processing performance has been scrutinized by hundreds of NWS radar meteorologists over 20 years; it works well, is improving, and constantly evolving. Changing software that has been field tested and evaluated based on data collected in the SHV mode for many years, requires similar extensive testing and evaluation in all types of severe storm environments before there is a nationwide deployment of the AHV mode for 24/7 service.

There are advantages using the AHV mode. Operation in the SHV mode means half the power is transmitted from each of the channels whereas in the AHV mode full power is alternately applied to the H and V antenna ports. Thus the per-pulse SNR is 3 dB higher for the AHV mode. Furthermore, because the polarization is alternately switched, second trip echoes from the previous polarized H (or V) transmitted signal is a cross-polar signal in the V (or H) receiver channel and thus the second trip echoes are significantly suppressed.

Another advantage of the AHV mode is that it is fully polarimetric. This means measurements can be made of the linear depolarization ratio and of the correlation between the copolar and cross-polar weather signals. These products could benefit cloud microphysical studies and numerical models of storm evolution. Although extensive research has been ongoing to determine the benefit of ingesting copolar data (i.e., Z_h, Z_v, ρ_{hv} and the H and V propagation phase difference Φ_{DP}) into storm models (Jung et al., 2008a,b, 2010a,b; Zhang et al., 2006), there needs to be similar research to show the benefit of cross-polar data (Matrasov et al. 2001) . However, because cross-polar backscatter is much weaker (i.e., 20 to 30 dB weaker) than the copolar echoes, these data are limited to regions of high reflectivity where cross-polar signal-to-noise ratio is sufficient for accurate measurement.

As mentioned earlier, if there is cross-polar radiation lobe coaxial with the copolar beam, the Z_{DR} bias is much less for the AHV mode. Thus the AHV mode is relatively immune to antenna design and/or manufacturing errors that could cause cross-polar lobes coaxial with the copolar lobe. If phased array antennas cannot produce a deep cross-polar null (i.e., deeper than 45 dB below the copolar peak) along the beam axis of every beam at reasonable cost, the use of the AHV mode would be mandatory. Calibration of differential powers (i.e., to estimate Z_{DR}) is a challenging problem, even for the single beam of a mechanically steered antenna as illustrated by several papers on this topic (e.g., Hubbert et al., 2003; Zrnić et al., 2006), especially if the mechanically steered beam cannot be pointed vertically as with the WSR-88D. Insuring differential reflectivity accuracies to a tenth of a dB for the thousands of beams of a PPAR is likely an even more challenging problem. On the other hand, because differential power needs to be calibrated to within a tenth of a dB, whereas absolute power calibration accuracy is relaxed by an order of magnitude (i.e., 1 dB), there might be alternatives to calibrate the PAR.

Because of gravity most hydrometeors have their axis of symmetry vertical, and because center-fed parabolic reflectors have negligible on-axis cross-polar radiation, the SHV mode performs well for quantitative precipitation measurements. If the axis of symmetry is, on average, vertical there is little conversion of H to V and vice versa as the wave propagates to and from the scattering volume V_6. That is, H and V waves propagate independently and the copolar properties (i.e., Z_h, Z_v, and ρ_{hv}) of the scatterers in V_6, and the H and V propagation phase difference Φ_{DP} can be unambiguously and accurately measured. Although propagating H and V waves are not depolarized, they do experience differential phase shift and attenuation.

On the other hand, circularly polarized waves are depolarized when propagating through rain; that is, right-handed circularly polarized waves can be converted, if the propagation path is sufficiently long, to left-handed circularly polarized waves and vice versa. In this case copolar echoes from storms can be strongly attenuated and even

disappear (Zrnić, internal memo to the NSSL Director). Circularly polarized radiation was installed on the first 10 WSR-88D radars, but after it became clear that severe attenuation of circularly polarized waves would be encountered, linear polarization was installed on all WSR-88Ds.

The minimal depolarization of H, V polarized waves propagating under normal precipitation conditions is the principal reason why the linear polarization basis is favored over circular polarization for rain rate measurements made with the WSR-88D (Doviak et al., 1998, 2000). However in regions of strong vertical shear of horizontal wind, or in regions of strong storm related electric fields, hydrometeors might no longer have a vertical axis of symmetry. In this case H waves will be converted to V waves and vice versa, and "depolarization regions" can be seen in the data. In these "depolarizing regions" of a storm, the polarimetric parameters of scatterers in the resolution volume have significant bias (e.g., Fig.2.2). However, because depolarization rarely occurs at the lowest altitudes of the atmosphere, measurements of precipitation accumulations should not be affected.
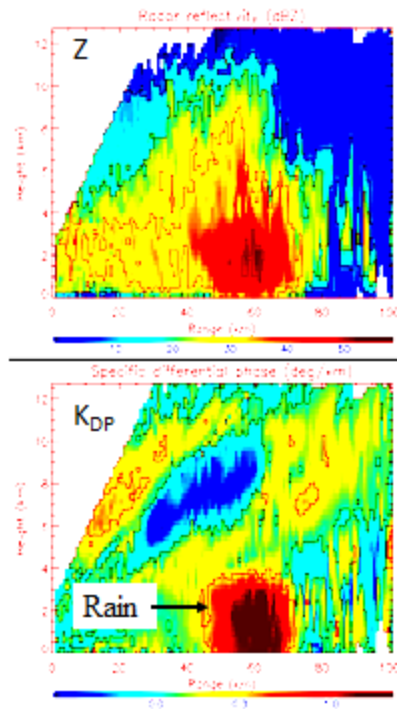

Fig.2.2 Upper panel: the vertical cross section of reflectivity factor Z_H (dBZ) in a storm. Lower panel: radially extended regions of lower specific differential phase K_{DP} (deg km^{-1}) caused by depolarization effects (i.e., strong storm induced electric fields causing ice crystals not to have their axis of symmetry horizontal or vertical).

In principle, if there is no depolarization along the propagation path, and if the amplitudes and phases of the transmitted copolar and cross-polar radiation are measured with sufficient accuracy, and the amplitudes and phases of the copolar and cross-polar echoes are simultaneously measured with equally sufficient accuracy, one should be able to estimate without bias, irrespective whether the SHV or AHV mode is used, all the copolar properties (i.e., Z_h, Z_v, and ρ_{hv}) of the scatterers in V_6. However, it might turn out that the required upper bounds of the cross-polar field intensity for the AHV mode is

significantly relaxed compared to the SHV. But how accurate these measurements need to be made to satisfy the accuracy specifications placed on the copolar properties of scatterers in V_6 requires a thorough investigation and testing on prototype weather PPAR.

2.3. Measured cross-polar radiation from some phased array antennas

If the SHV mode of polarimetric data collection is to be used, negligible levels of cross-polar radiation along the beam axis need to be maintained (i.e., more than 40 dB below the copolar peak); otherwise precise knowledge of the amplitude and phase of the copolar and cross-polar radiation along each of the PAR beams is required. In this section we show two different phased array antennas that have measured deep nulls of cross-polar radiation along beams in the principal planes of radiation. One electronically steers the beam in two dimensions (i.e., 2D phase-phase scanning); the others uses a combination of electronic scanning in one direction (1D electronic scanning), but mechanically steers the beam in the orthogonal direction. The hybrid mechanical and electronic scanning directs the beam to always be in the principal planes and thus should produce the lowest cross-polar radiation field. The 2D phase-phase scanning is implemented on NSSL's NWRT, which only transmits V copolar waves.

A dual polarimetric phased array antenna having 1D scanning in elevation is comprised of an array slotted waveguides that is mechanically steered in azimuth; this has been developed by ITT Gillfillan (Wolfson and Cho 1980). Another 1D scanning radar has been developed by the Center for Collaborative Adaptive Sensing of the Atmosphere (CASA), an engineering research center sponsored by the National Science Foundation. CASA is advancing technology to enable future deployment of a dense network of low-power short-range radars for the observation of weather in regions where present radar networks, such as the WSR-88Ds, have poor surveillance coverage (Salazar et al., 2010). This 1D antenna also has dual polarization capability.

2.3.1 A weather PAR having 2D electronically scanned beams

The elements of the NWRT phased array are rectangular horns (i.e., aperture antennas) excited with a TE_{10} mode in which the electric field, in the plane of the horn's aperture, lies in a vertical plane. Horns are often the aperture of choice because they support operation over a wider range of frequencies than slotted waveguides, or open ended cavity resonators (i.e., patch array elements). But the electric vector in the horn's aperture is not vertical because the face of the NWRT aperture is tilted by 10° relative to the vertical. Thus although the intended copolar polarization is vertical, unintended horizontal cross-polar components are generated. Tilting of the face of a planar array, to achieve observations at higher elevation angles with less loss of gain, is detrimental to weather observations at low elevation angles where polarimetric observations are most critical. This is because, as will be shown, cross-polar radiation is significant when the beam is directed away from the principal planes.

Although a non-tilted vertically polarized aperture generates only vertically polarized electric fields (i.e., only an E_θ = V field) in the vertical and horizontal principal planes, a vertically polarized tilted aperture has horizontally polarized electric fields (i.e., E_φ = H polarized field) as well as a vertically polarized component. In general beams directed outside the principal planes have a vector field oblique to the orthogonal unit vectors $\vec{a}_\theta, \vec{a}_\phi$ of a spherical coordinate system having the polar axis vertical as assumed for polarimetric radars observing weather. Although the NWRT does not have dual polarization capability, the boresight cross-polar radiation (i.e., the horizontally polarized field) has been measured by NSSL researchers (Curtis and Meier, 2009) and has been used to assess the level of cross-polar radiation associated with an array of aperture elements to verify the calculations of Zhang et al., (2009) to correct bias due to cross-polar radiation.

The cross-polar radiation experiments made with the NWRT (Doviak et al., 2011) show (Fig 2.3 left panel) the cross-polar field along the boresight for a beam 8° below the broadside direction (i.e., the direction perpendicular to the face of the array which, for the NWRT, is tilted 10° relative to the vertical). As can be seen, the cross-polar radiation along the beam in the vertical principal plane, is more than 45 dB below the copolar peak. Such low cross-polar radiation along the beam is required for quantitative polarimetric weather measurements using the SHV mode of polarimetric data acquisition being implemented on the national network of weather radars that presently use center-fed parabolic reflectors.

But this observed exceptionally low cross-polar radiation along the beam axis needs to be maintained when the beam is pointed outside the principal planes. If cross-polar radiation along the boresight (i.e., along the beam axis) of these beams can be kept to levels 45 dB below the peak of the copolar beam, the cross-polar radiation along the beam will not significantly bias polarimetric measurements.

But, Fig.2.3 (right panel) shows the peak of cross-polar radiation along the boresight is significantly higher (i.e., about 15 dB higher than that cross-polar peak seen in Fig.2.3 left panel) when the beam is electronically steered at a 45° azimuth and -8° elevation away from the array's broadside direction (i.e., the beam does not lie in a principal plane). Such high levels of cross-polar radiation are unacceptable using the SHV mode for polarimetric measurements of weather. But, because the array face is tilted 10° from the vertical, the high level of cross-polar radiation seen in the right panel of Fig.2.3 is primarily due to the horizontal component of the electric field in the aperture (Doviak et al., 2011). That is, even though only the copolar V port (in the NWRT the only port is the V port) is energized there will be cross-polar H fields when the beam is directed away from the principal planes simply because of the array tilt.

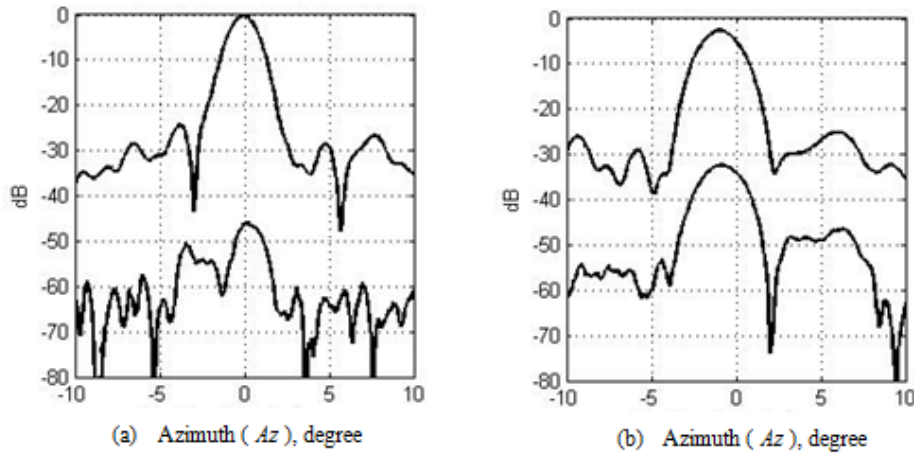(a)   Azimuth (Az), degree   (b)   Azimuth (Az), degree

Fig.2.3 The copolar (i.e., the V or E_θ field; upper traces) and cross-polar (i.e., the H or E_ϕ field; lower traces) radiation patterns, normalized to the peak copolar radiation for beams electronically steered to: (a) 8° below the broadside direction but in the vertical principal plane, and (b) at 45° from the vertical principal plane, but still at -8°. Azimuths (Az) are relative to the electronically commanded azimuth of the beam.

On the other hand, cross-polar H field is generated by a vertically polarized aperture in an infinite perfectly-conducting vertical plane (Lei et al., 2012). That is, even if the vertically polarized aperture were not tilted, there would still be cross-polar H fields outside the principal planes as seen in Fig.2.7d of this report. In summary, although only the V antenna port of the NWRT is energized, and even though the cross-polar H fields in the principal planes are negligible (ideally they should vanish because of symmetry), horizontally (H) polarized fields will be generated by currents on the conducting surface surrounding the array elements, even if the surface is perfectly conducting and infinite in size.

But if surface currents on the array face and the array face tilt are the only sources of cross-polar radiation, and if this cross-polar field can be accurately calculated or measured, a correction matrix can be applied to the received echoes to remove the bias in polarimetric measurements irrespective whether the SHV or AHV data collection mode is used (Lei et al., 2012). But the correction matrix reported by Lei et al. (2012) ignores the effect other apertures have on the surface currents. It remains to be shown whether this theoretical correction matrix, or one calculated from measurements, is sufficiently accurate to keep Z_{DR} bias less than 0.1 dB.

Fig.2.4 shows the measured cross-polar H radiation as a function of beam direction relative to broadside, and compares this level of cross-polar radiation with that obtained from an array of horizontally and vertically oriented Hertzian dipoles having dipole moments calculated to account for the cross-polar field observed at broadside, and at an angular displacement from the vertical principal plane. The vertical dipole moment is adjusted (theory adj., dashed line in Fig.2.4) for each azimuth beam direction to compensate for the variation of aperture gain when the beam is steered away from the

broadside direction. The data show the cross-polar field is principally due to the tilted array and the cross-polar fields radiated by the aperture distribution.

But there are significant departures (i.e., more than 0.1 dB) from theory suggesting that there might be sources of cross-polar radiation other than that theoretically calculated based on the designed aperture distribution. Cross-polar radiation associated with the designed aperture distribution henceforth is denoted as the **primary** cross-polar radiation to differentiate it from **secondary** cross-polar radiation due to errors in manufacture, assembly, and other spurious effects (e.g., radiation from feed lines, mutual coupling effects, etc.).
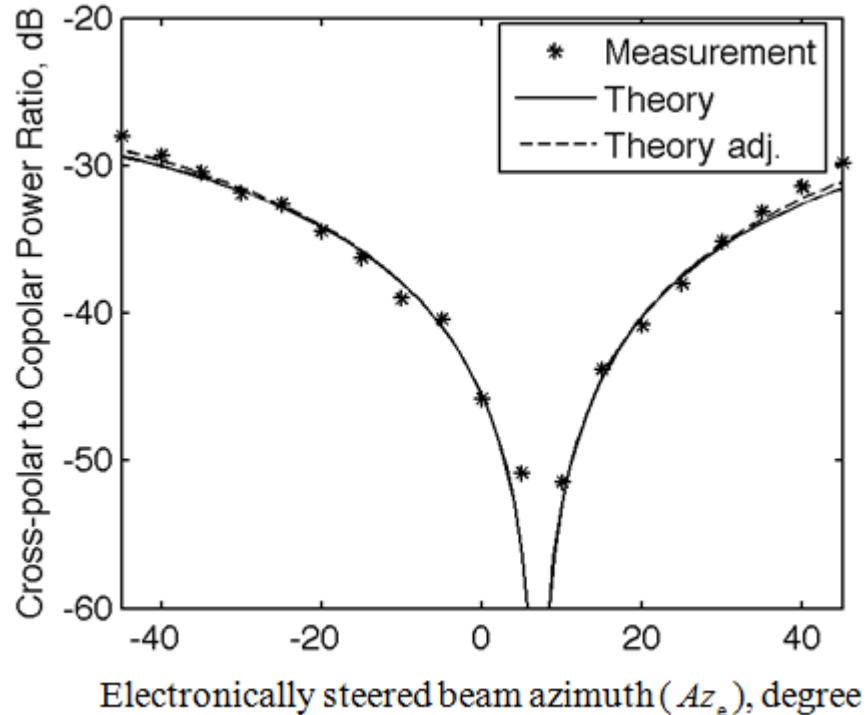

Fig.2.4 Measured (asterisks) cross-polar fields along the axis of the copolar beam as a function of the azimuth of the electronically steered beam direction compared with theory. The polarization of the copolar field is vertical. The solid line is the theoretical dependence if the array elements were ideal dipoles. The dashed line (theory adj.) is obtained when dipole gains are adjusted as a function of beam direction to account for the directive gain of the aperture elements (horns) of NSSL's NWRT.

Secondary cross-polar fields can also be seen in radiation emitted by parabolic reflector antennas if, for example, the feed horn antenna ports are not orthogonal (Zrnić, et al., 2010). If the H **or** V port, of an ideal array element is energized, the primary cross-polar radiation is that due to the projection of the radiated electric field vector (i.e., in general some combination of E_θ, E_ϕ fields) onto the local V or H directions (i.e., $\vec{a}_\theta, \vec{a}_\phi$).

A puzzling feature of the cross-polar field is the unexpected 6° displacement of the cross-polar null from the vertical principal plane (i.e., from $Az_e = 0$). If the polarization within the aperture of each horn was purely vertical as designed, the null of

27

cross-polar radiation should have been along the broadside. This suggests artifacts generate secondary cross-polar radiation in the horn aperture (Doviak et al., 2011). Furthermore, some measured points are more than a few tenths of a dB either side of the theoretical line. It is not certain whether this is due to measurement error, or does the data show that there are other sources of secondary cross-polar radiation. These departures from the theoretical curve emphasize the importance of a precise design and need for calibration of each of the beams.

2.3.2 Polarimetric phased arrays with 1D electronic scanning

Two dimensional scanning with phased array radar is the most expensive option, but offers maximum flexibility to steer the beam. A less costly approach, and one that could offer faster updates than presently obtained with fully mechanically steered beams, are phased array radars in which beam direction in azimuth (or elevation) is mechanically scanned whereas the beam direction in elevation (or azimuth) is electronically controlled. For example, the Rapid-DOW (Doppler on Wheels; Wurman and Randall, 2001) mechanically scans in azimuth, but elevation coverage is obtained by stacking several beams (in elevation) whereby each beam corresponds to radiation at a different frequency. The beams are electronically steered in elevation by sequentially shifting the microwave frequency within a relative long transmitted pulse; this is called frequency-phase steering in elevation. Thus elevation coverage is practically simultaneously obtained whereas coverage in azimuth is obtained by rotating the antenna on a pedestal.. Although the Rapid-DOW decreases, by an order of magnitude, the update time to scan a volume of weather, it is a singly polarized PAR.

2.3.2.1 Beams mechanically scanned in azimuth

An example of a dual polarized PAR having a 1D electronic beam steering in elevation is one that consists of interleaved, orthogonally polarized sub-arrays of dual-slotted square coaxial transmission lines (or "sticks"). The dual slots along each stick form an array element in which slot length determines the taper of the aperture distribution. This pair of slots is analogous to the pair of slots associated with patch antennas (Section 2.4.3.), which seem to play a role in reducing the cross-polar fields at elevation angles near the horizontal principal plane. The periodic spacing between the sticks is about a quarter of a wavelength. Thus the stick array pair is essentially a single dual polarimetric linear array with a common phase center. A demonstrator aperture has been designed, fabricated, and tested by ITT Gilfillan (Fig.2.5a; Wolfson and Cho, 1980). Every other slotted line or stick generates a $\pm 45^{o}$ linearly polarized wave in a vertically broad beam but with an azimuth width of about 2.4^{o} determined by the 3.7 m width.

In this demonstrator aperture, designed to operate in the 10-cm band, there are 8 pairs of slotted lines. By adjusting the relative phase between adjacent lines, any polarization can be transmitted. However to transmit and receive in the H, V basis, the array shown in Fig.2.5a would be rotated by 45° so that one set of alternate lines would generate and receive H polarized waves, whereas the other set would transmit and receive V polarized waves. Electronic steering in a direction orthogonal to the sticks can be accomplished by using a single phase shifter per row as done for the AWACS phased array radar (Brookner, 1988; Section 2.6.2.1).

A Chebyshev aperture distribution provides ultra-low sidelobes. But ultra-low sidelobes are only achieved because slots have been accurately cut by using numerically controlled machining, and because there is theory to accurately calculate the effects of mutual coupling between the radiating elements (Brookner, 1988). This theory and the use of accurate machining could account for the very low cross-polar in broadside radiation. Figs.2.5b and c show the copolar and cross-polar radiation patterns in the horizontal principal plane. The cross-polar radiation along boresight is well below 40 dB suggesting that slots could be used as radiating elements to achieve very low cross-polar radiation, at least in the principal planes. Having such low cross-polar fields suggests that the SHV data collection mode can be used to calculate Z_{DR} and ρ_{hv} without incurring significant bias

Although this 1D (i.e., electronic scanning only in a direction perpendicular to the direction of the sticks) phase agile PPAR does not offer all the advantages of a 2D (i.e., phase-phase) agile PPAR being presently considered for MPAR, it has some advantages over the WSR-88D, and costs significantly less than a 2D PPAR. A 1D phase agile PPAR could obtain modest improvements in update rates by using multiple receiving beams at high elevation angles where the full gain of a single beam might not be needed. However, significant analysis is required to ferret out all the pros and cons of this approach and to determine if it can be a cost effective alternative to a fully 2D PPAR.
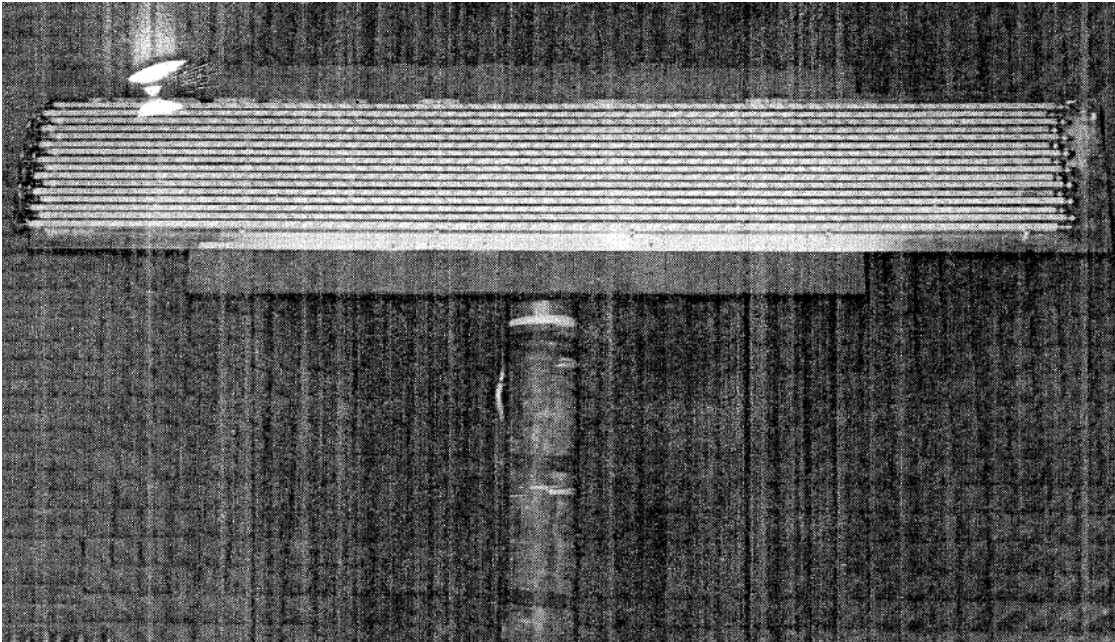

Fig.2.5a Demonstrator dual polarimetric slotted array antenna consisting of 16 interleaved dual polarized array sticks (Wolfson and Cho, 1980)
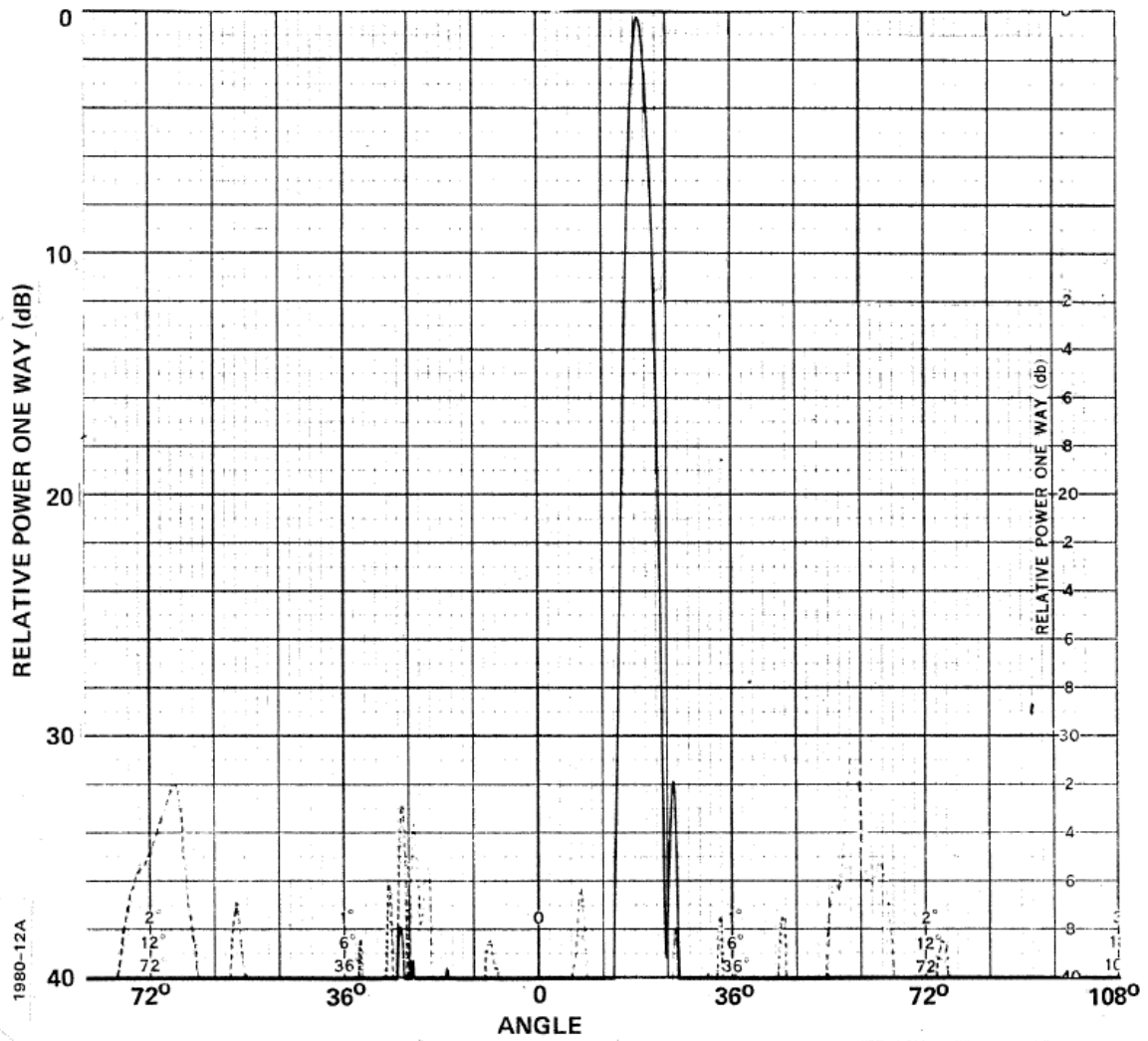
Fig. 2.5b Copolar H (solid line) and cross-polar V (dashed line) antenna patterns of the dual polarimetric slotted array operating at 3.1 GHz and measured in an anechoic chamber.
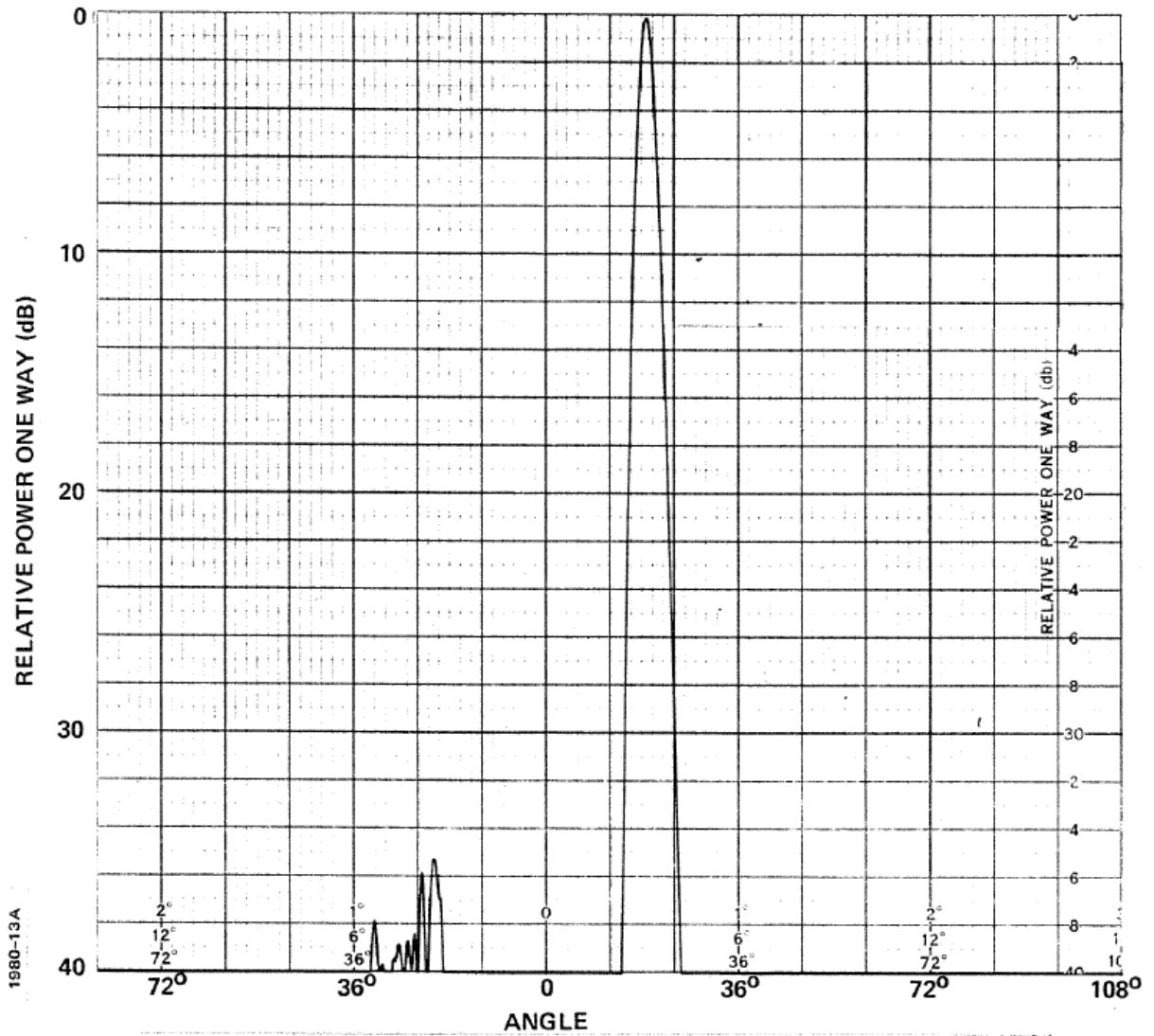
Fig. 2.5c As in Fig. 2.5b, but the copolar V channel is energized. The maximum cross-polar H field is below -42 dB (i.e., below the displayed span).

2.3.2.2 Beams mechanically scanned in elevation

An example of a dual polarized PAR having a 1D electronic beam steering in azimuth is one developed by the Engineering Research Center for CASA. The Center is researching an alternative approach to surveillance of weather, one with a low-cost and providing coverage where present network radars have data voids. This approach calls for a dense network of short wavelength dual H, V polarimetric radars that observe storms at short range, communicate with one another and adjust sensing strategies in direct response to the evolving weather and changing end-user needs (McLaughlin, et al., 2009).

The Center has developed a dual (H, V) polarized 3-cm planar phased array solid state radar that performs electronic steering in the azimuth direction (i.e., $\pm 45^{\circ}$) while mechanically steering in elevation (i.e., a so-called phase-tilt array antenna (Salazar, et al., 2010). Four such planar antenna arrays can provide volume coverage within the troposphere. This rectangular array (1 m in the horizontal and 0.5 m in the vertical direction) has four sub arrays (Fig. 2.5d) and has a total of 64x32 patch elements.

Although the H and V copolar and cross-polar far field patterns of this array were not shown by Salazar et al., (2010), the patterns of a single 32 element column embedded in one sub-panel was measured and presented. That is, only one column of patches was excited and the patterns for one column in one sub-panel were measured along one of the principal planes; these patterns are reproduced in Figs. 2.5e and f. The patterns show deep nulls of cross-polar radiation along the broadside beam axis, similar to that measured for parabolic reflector antennas along a plane 45° from the principal planes (Zrnić et al., 2010). However, the cross-polar peaks for the column array are about 18 dB below the copolar peak, whereas the cross-peaks for the parabolic reflector are about 36 dB below the copolar peak. Furthermore, theory for the cross-polar radiation from a patch element (Section 2.4.3 of this report) suggests a null along the entire principal plane whereas Fig. 2.5f shows a peak of cross-polar radiation along the principal plane. Finally, theoretical patterns of an ideal patch suggest no cross-polar radiation associated with the copolar H field (Fig. 2.8b of this report). It remains to be seen whether these deep nulls will be present for the entire array and whether the cross-polar peaks are sufficiently low to permit operation in the SHV mode. Nevertheless, the preliminary measurements show promise for the use of low cost ID electronic scanning arrays in which the beam remains in a principal plane, whereby the principal plane changes direction by mechanically rotating in azimuth, or by or tilting in elevation. Keeping the beam in a principal plane, where typically the cross-polar radiation is minimal, is also the property of a Cylindrical Polarimetric Phased Array Radar (CPPAR) being developed by the Atmospheric Radar Research Center of the University of Oklahoma (Zhang et al., 2011). However the principal plane of the CPPAR changes direction by azimuthally commutating the excitation of vertical columns around the circumference of the cylinder; thus the CPPAR has no moving parts, unlike that of the ID Planar PPARs.
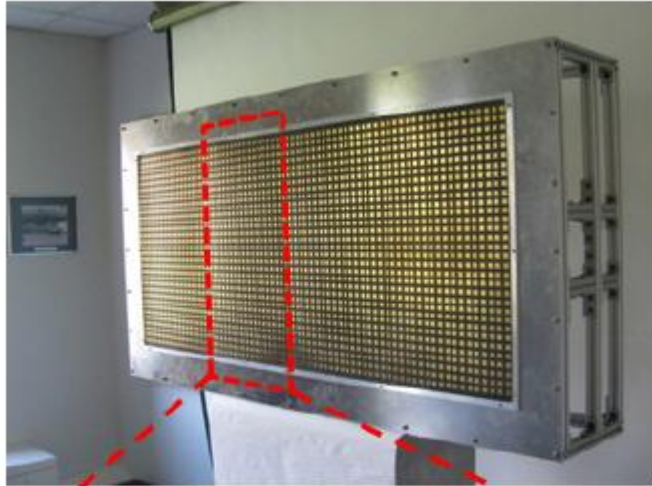
Fig. 2.5d Phase tilt phased array antenna. The dotted area is one sub-panel of the four sub-panel array shown here.
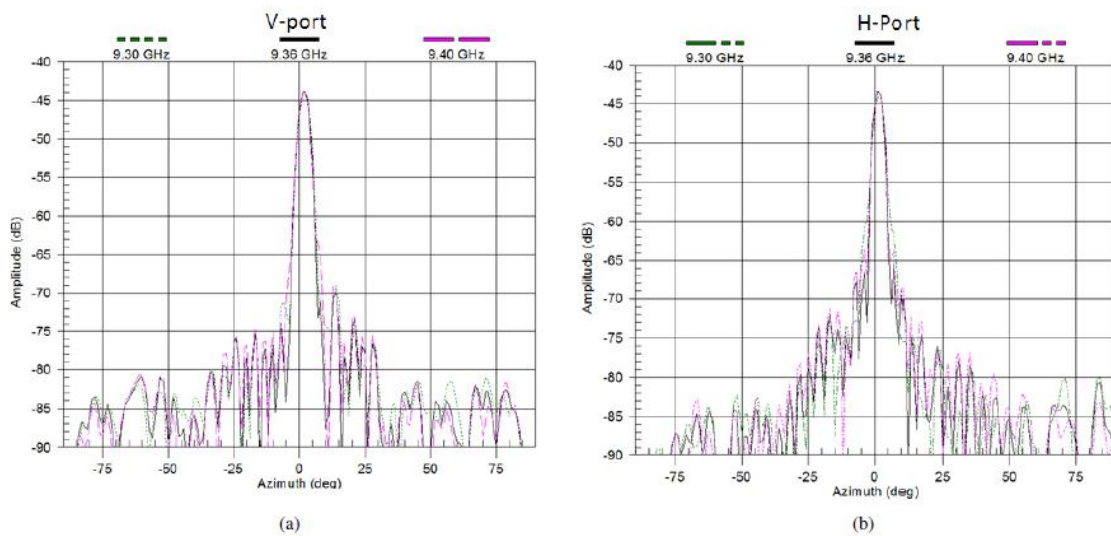

Fig. 2.5e The copolar V (left panel) and copolar H (right panel) patterns of a 1x32 element column of patch elements embedded in a sub-panel of 16x32 elements.
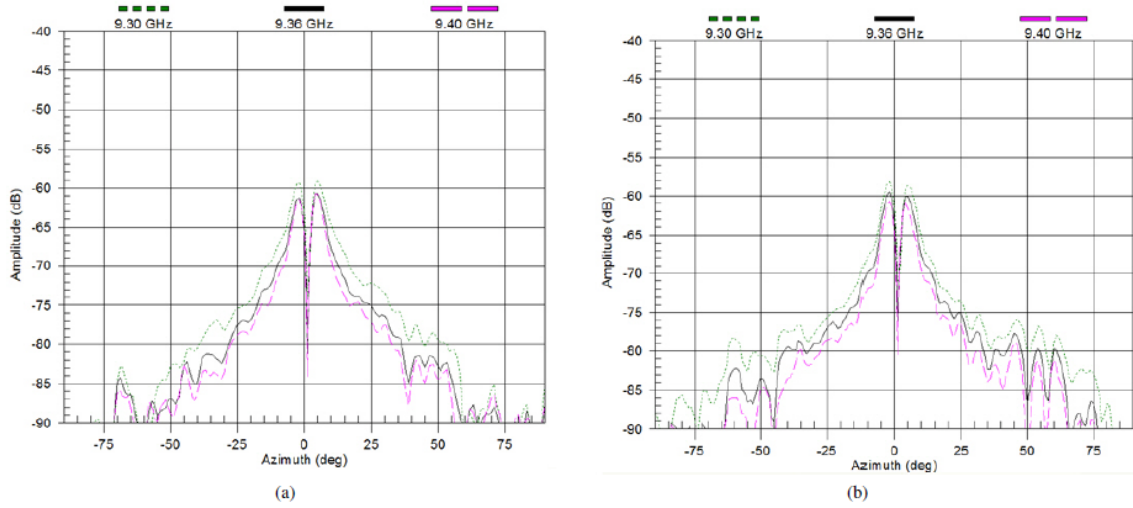
Fig. 2.5f The corresponding cross-polar H (left panel) and cross-polar V (right panel) patterns for a single 32 element column of patch elements.

2.4 Phased array antenna elements

Because the array element is the key to having a PPAR that meets the stringent requirements of low cross-polar radiation along the beam for beams electronically steered in any direction, this section compares some candidate elements and presents, where possible, their actual or theoretically calculated performance.

2.4.1 Dipoles

Because peak transmitted power is distributed over the array, the amount of power being radiated by each element is relatively small. Thus electric dipoles can be used with less concern of electrical breakdown. Crossed electric dipoles accurately placed in an array have been used in many large diameter PARs (Brookner, 1988, Section 2.2.6.1) to produce circularly polarized waves with radiation patterns having extremely low side-lobes. Thus it seems likely that the exacting manufacturing tolerances required to produce antennas with ultra-low sidelobe levels could also provide antennas with very low secondary cross-polar radiation.

An ideal dual polarimetric radiating element for a PPAR is a pair of parallel electric and magnetic dipoles. Whereas the electric dipole can be approximated by a center-fed conducting wire, the magnetic dipole is approximated by a narrow slot in a conducting plane (Jordan and Balmain, 1968, Chapter 13). The fields generated by a magnetic dipole only differ from those generated by an electric dipole in that the electric and magnetic fields (in a spherical coordinate system with the polar axis along the z coordinate of the dipole axes) are interchanged (i.e., $H_\phi^{(e)} \to E_\phi^{(m)}; E_\theta^{(e)} \to H_\theta^{(m)}$; superscripts 'e' and 'm' define respectively the fields of the electric and magnetic

dipoles). Thus an electric dipole having a z directed axis generates only vertically polarized waves (i.e., E_θ) whereas the z directed magnetic dipole generates only horizontally polarized waves (i.e., E_ϕ). The use of electric and magnetic dipoles aligned in the vertical originated from Dr. D. Staiman of BCI/Lockheed Martin. With such an arrangement, copolar H or V fields can be theoretically generated to be completely free of cross-polar radiation in any direction. On reception H and V backscatter can be received independently as with polarimetric radar using a parabolic reflector antenna. Rather than having a pair of crossed electric dipoles as is common (e.g., Brookner, 1988), an array element having vertically aligned electric and magnetic dipoles as illustrated in Fig.2.6a[1] has been proposed.

The theoretical absence of primary cross-polar radiation anywhere makes a PPAR having an array of magnetic and electric dipoles theoretically superior to the parabolic reflector illuminated with a feed horn (i.e., a design used for the WSR-88D). The parabolic reflector antenna has a feed and associated supports that block the beam and generate additional secondary cross-polar fields, but a PPAR does not have feed supports. However, parabolic reflector antennas have been designed and built for weather radar using an offset feed that eliminates blockage (Bringi et al., 2011).

Although the emphasis of the LMCO design is on the colocation (i.e., in the y, z plane) of slots and dipoles, it is likely that an arrangement of interlaced slots and dipoles would also keep levels of cross-polar radiation well below the desired 45 dB with respect to the copolar field. Moreover, such an alternative might lessen the disturbance of the aperture fields that transmission lines feeding the two dipoles cause; and also might reduce secondary cross-polar radiation due to such artifacts and as well the mutual coupling between H and V elements (i.e., between the slots and electric dipoles). To have a common phase center of the array, there must be one more row and column for either the slot or dipole arrays. Thus the slot or dipole will have a slightly larger beamwidth (i.e., less than $0.01°$). We need to check whether this small difference in beamwidth and gain (i.e., < 0.1 dB) causes significant bias in weather measurements.

---

[1] The figures shown in this section were adapted from a power point presentation given by Y. Al-Rashid of LMCO, on November 9, 2010 in response to the NSSL sponsored BCI/LMCO NOAA PAR Task Order 5: "Radiating Element Final Review". These figures are not approved for public release, nor are secondary distributions authorized without prior written approval of the NSSL program manager.
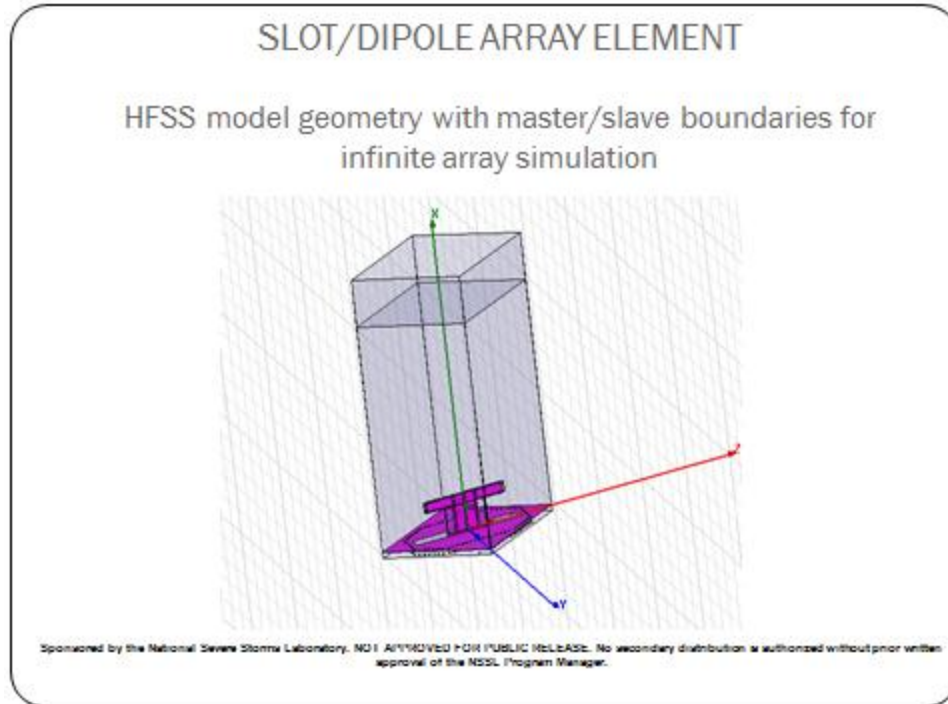
Fig.2.6a The z-directed and aligned pair of conducting strips that approximates the center-fed electric dipole located above a z-directed slot in a y, z conducting surface. The slot approximates the magnetic dipole. The feed line for the electric dipole is the pair of closely spaced conducting strips oriented in the x direction and passing through the slot. The slot is illuminated with a y directed electric field to approximate the vertically oriented magnetic dipole.

Although the ideal vertical slot (i.e., vertical magnetic dipole) and electric dipole should generate copolar fields everywhere free of primary cross-polar fields, radiation from the transmission lines feeding the dipole and slot, errors in manufacturing and assembly, etc. will cause secondary cross-polar V fields (i.e., E_θ) to be generated by the vertical slot and its associated connections, and will also cause secondary cross-polar H fields (i.e., E_φ) to be generated by the dipole and its associated connections. It remains to be seen whether such a configuration of slots and dipoles can be manufactured and assembled at sufficiently low cost so sufficiently low (i.e., less than -45 dB below the copolar peak) secondary cross-polar radiation can be obtained, at least in the lowest several degrees of elevation angle where quantitative estimates of precipitation rates are most important.

Figs.2.6b and c show, as a function of zenith and azimuth angles, the numerically calculated secondary cross-polar levels radiated from the combined slot and electric dipole model configuration shown in Fig.2.6a. The calculation is based on the High Frequency Structure Simulator (HFSS) software to numerically determine the electromagnetic field around structures having specified voltage and/or current sources

36

feeding the structure (in this case the antenna and its associated feed lines, the ground plane, etc.). It is obvious there are secondary cross-polar fields even for this idealized model that should have no primary cross-polar radiation. Because of the symmetrical configuration, the secondary cross-polar field should be symmetrical about the principal planes (i.e., about the horizontal plane at 90° zenith and the vertical plane 0° azimuth).

In the lowest regions of the atmosphere where zenith angles lie between 80° and 100° (i.e., at elevation angles below 20° for an array tilted 10° to the vertical) the secondary cross-polar fields generated by the slot are more than 40 dB below the copolar peak for all azimuths between $\pm45^o$ (this is the required azimuth coverage for each face of a four-faced planar phased array radar). Cross-polar fields are the lowest (i.e., 60 to 70 dB below the copolar peak) along the broadside direction. Likewise the secondary cross-polar fields of the vertical electric dipole are more than 40 dB below the copolar peak everywhere for elevation angles below 20° and azimuths between $\pm45^o$.

If such a low secondary cross-polar field can be sustained in manufacture and assembly, Z_{DR} might be estimated without significant bias. But even if such low cross-polar fields are only sustained over the azimuths and elevations angles where quantitative precipitation measurements are need, the correction procedures suggested by Zhang et al., (2009) and Zrnic et al., (2011) to provide quantitative precipitation estimates can be greatly simplified. That is, a PPAR composed of electric dipoles and slots has the potential to perform polarimetric measurements that might match those obtained with the mechanically steered center-fed parabolic reflector antenna presently used by the NWS.
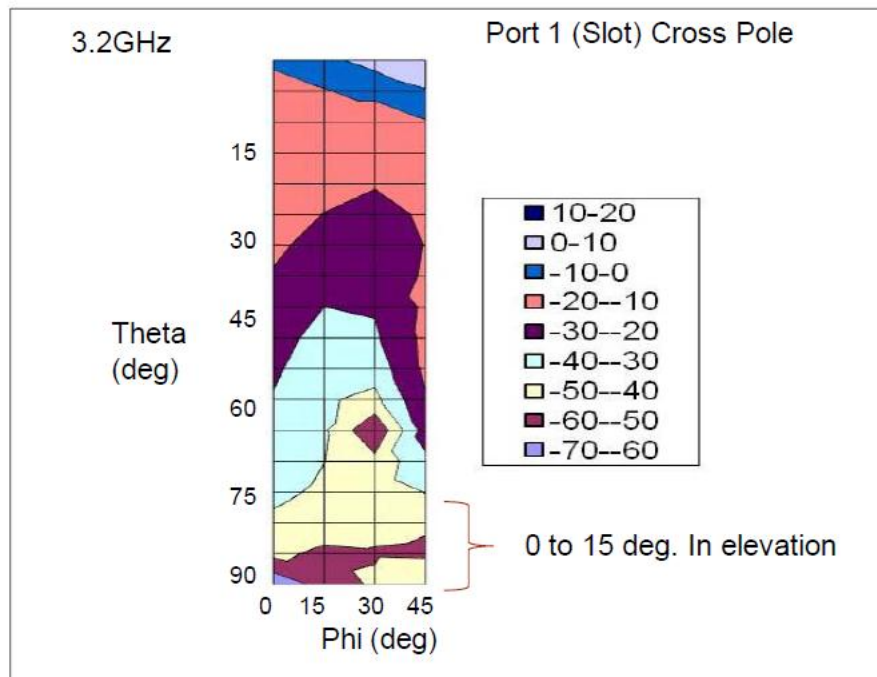
Fig.2.6b The HFSS numerically calculated secondary cross-polar V field of the slot shown Fig.2.6a. The slot is energized to transmit copolar H field.
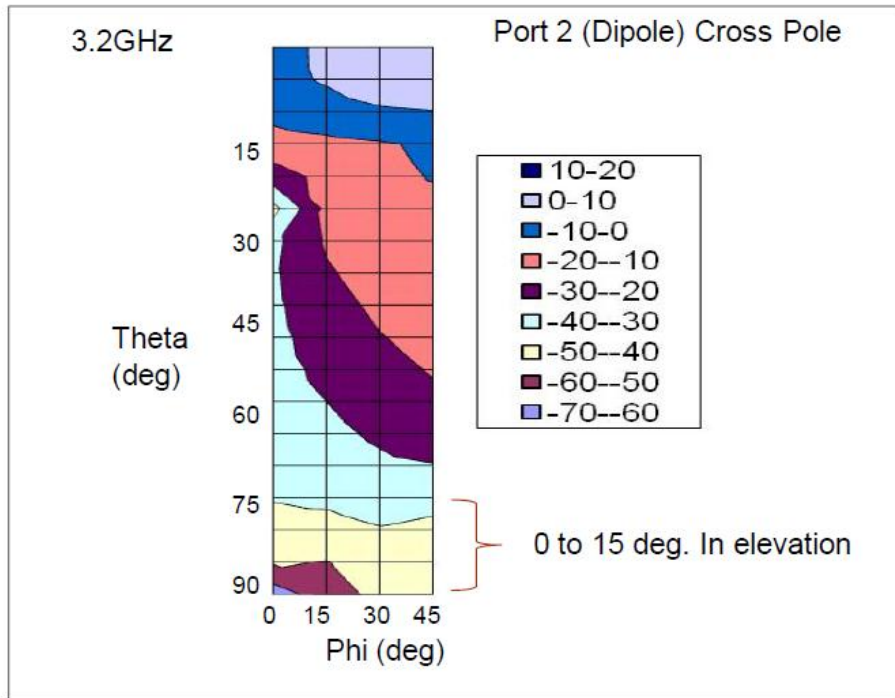

Fig.2.6c The HFSS numerically calculated secondary cross-polar H field of the electric dipole configuration shown Fig.2.6a. The dipole is energized to transmit copolar V field.

Although the performance of the vertically oriented slot and electric dipole show significant promise at the design frequency of 3.2 GHz, antenna efficiency decreases and cross-polar radiation increases at the extremes of the 200 MHz band (i.e., at 3.1 and 3.3 GHz). Fig.2.6d shows the return loss (a measure of antenna efficiency). The return loss at the dipole and slot antenna ports is likely more than that measured for the WSR-88D, but a -10 dB return loss should still be acceptable because efficiency at this design stage is not the most significant antenna parameter to be addressed. Another parameter of importance for the design of a PPAR is the isolation between the H and V channels of the array. As seen from Fig.2.6d, the isolation at the H and V antenna ports, computed using HFSS software, predicts 60 dB of isolation. This should be adequate for weather signal processing and is within the bounds specified for the WSR-88D.
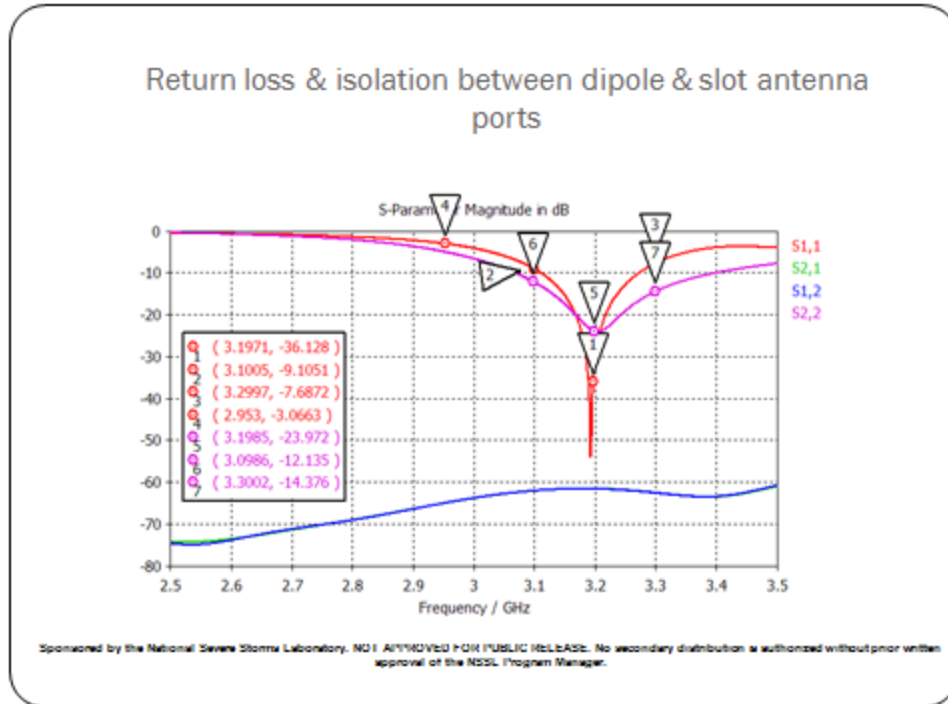
Fig.2.6d. Return loss (purple and red curves), and isolation (blue and green curves) between the dipole and slot antenna ports calculated using HFSS software.

On the other hand the cross-polar fields increase as the operating frequency departs from the designed frequency of 3.2 GHz. Figs.2.6e and f show the cross-polar fields of the electric dipole and slot energized at the lower end of 200 MHz wide band, a band of width matching one presently assigned to weather radars (i.e., 2.7 to 2.9 GHz). The cross-polar fields of the dipole and slot elements, although increased, are 40 or more dB below the copolar field for elevation angles below 10° (i.e., assuming an array tilted by 10°) for azimuths between $\pm 45^{o}$. Such low cross-polar fields could still allow quantitative precipitation fall rates without the need for bias correction, and might also allow data collection in the SHV mode. Furthermore, there might be other antenna designs that could reduce the cross-polar field at the extremes of the band.

Moreover, because the phase between the copolar and cross-polar fields exerts significant control on the level of cross-polar radiation that can be tolerated without significant Z_{DR} bias, it would be of great interest to have these intensity plots accompanied by cross-polar phase plots. For example, if the relative phase between
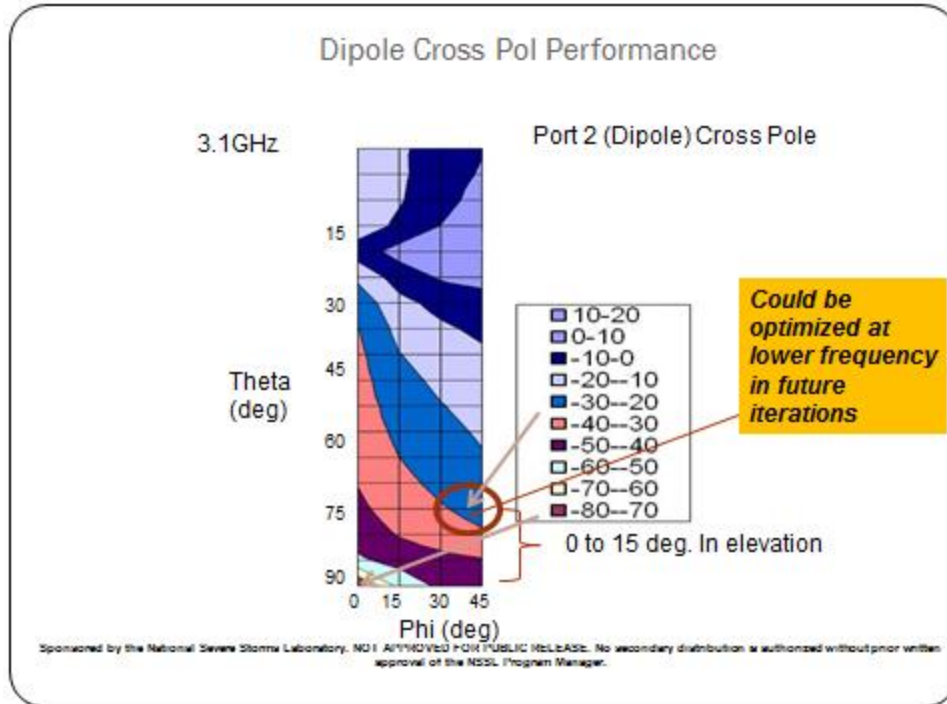
Fig.2.6e. The secondary cross-polar field if the dipole element is energized at 3.1 GHz (i.e., the lower end of the 200 MHz operating band of the PPAR).

copolar and cross-polar fields is about 0° or 180°, the peak level of coaxial cross-polar radiation that can be tolerated without causing significant Z_{DR} bias, can be increased by about 20 dB as discussed in section 2.2.2. If indeed the phase difference between the copolar and cross-polar patterns can be designed to be nearly in- or out of phase, then the level of cross-polar radiation can be as much as 25 dB below the copolar peak, without causing significant bias in Z_{DR}. But as stated earlier (i.e., section 2.2.2) the cross-polar phase might be caused by errors in manufacturing and assembly rather than by design. In this case these cross-polar fields are defined as being secondary. Nevertheless, this is an issue that deserves more study.

      On the other hand at the upper part of the 200 MHz band, the dipole and slot elements have secondary cross-polar fields noticeably worse than those in the lower half of the band. These cross-polar fields for the dipole and slot are shown in Figs.2.6g and h. The secondary cross-polar field associated with the slot (i.e., cross-polar V field given the copolar H field) is worse than that obtained with the dipole.
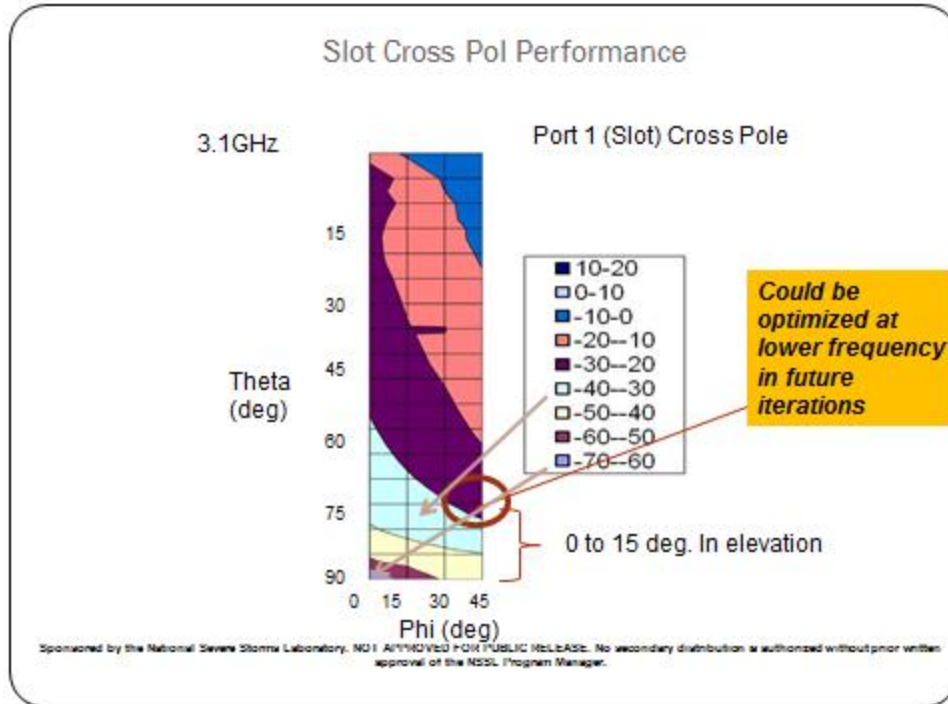
Fig.2.6f. The secondary cross-polar field if the slot element is energized at 3.1 GHz (i.e., the lower end of the 200 MHz operating band of the PPAR).
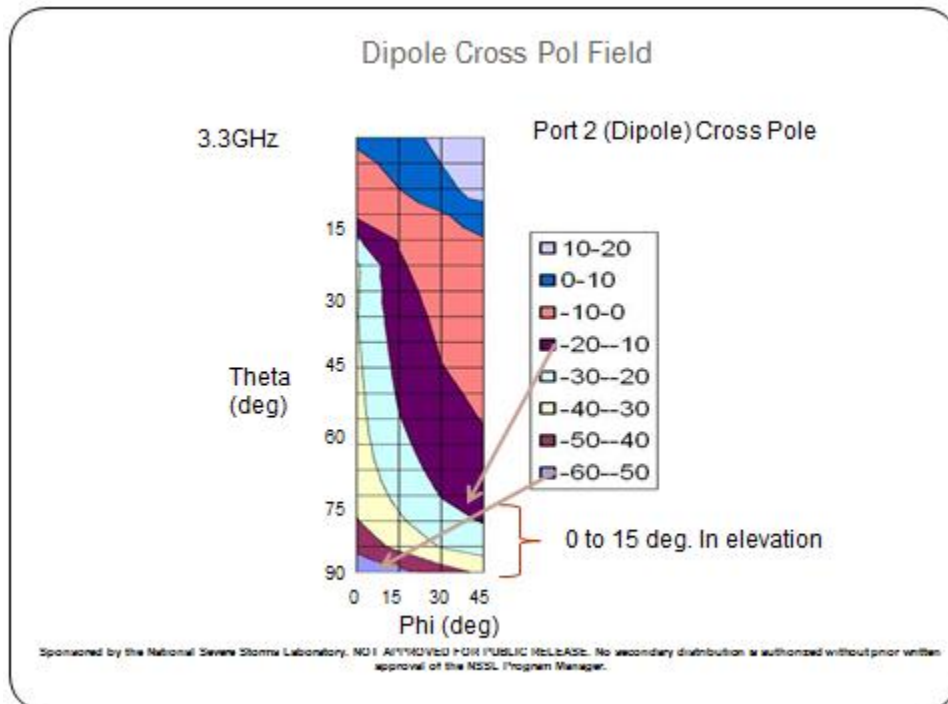

Fig.2.6g. The secondary cross-polar field if the dipole element is energized at 3.3 GHz (i.e., the upper end of the 200 MHz operating band of the PPAR).
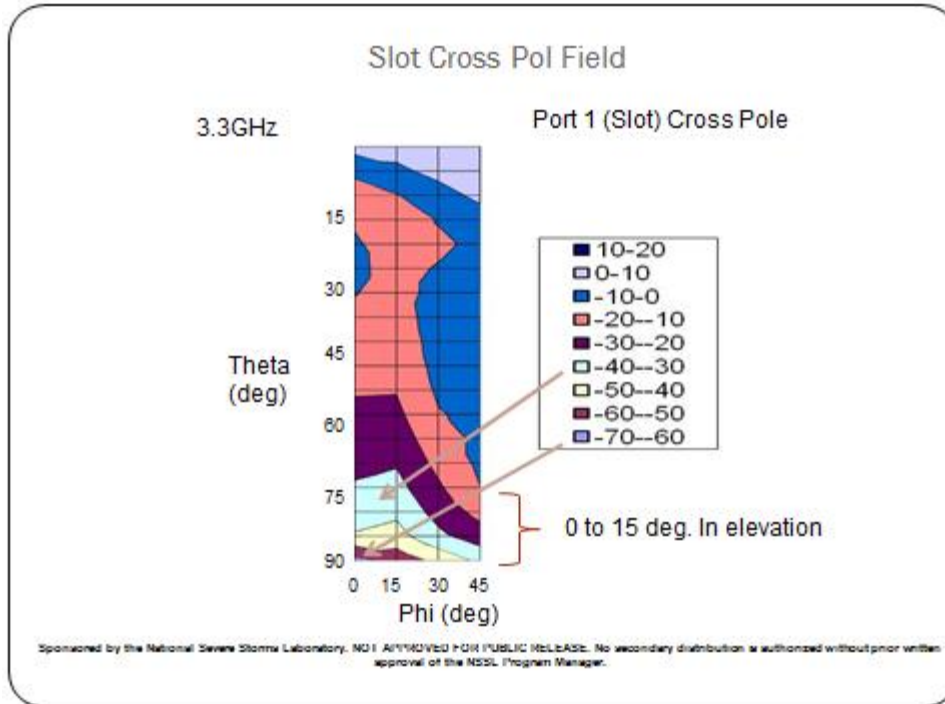
Fig.2.6h. The secondary cross-polar field if the slot element is energized at 3.3 GHz (i.e., the upper end of the 200 MHz operating band of the PPAR).

　　Although computer simulated secondary cross-polar field radiated from a dipole/slot configuration exceeds that 45 dB specified upper limit on the coaxial cross-polar lobe for many beam positions, the cross-polar radiation near the horizontal principal plane is below 45 dB for much of the operating band. Having such low cross-polar fields for beams near the ground is most critical because that is where quantitative precipitation measurements are made. Because the relative phase of the copolar and cross-polar fields is crucial to determining the level of cross-polar radiation that can be tolerated, it is most important to have measurements of this relative phase.

　　Although the vertically oriented ideal electric and magnetic dipoles produce no primary cross-polar radiation anywhere, an array of these dipoles likely has primary cross-polar radiation in directions away from the principal planes. For example, cross-polar H is expected because the electric dipole's $E_\theta^{(d)}$ (referenced to the spherical coordinate system of the dipole) does not necessarily lie in the vertical plane containing the array center and the point of observation. That is $E_\theta^{(d)}$, from any dipole not lying in the vertical principal plane, is not tangent, except along the horizontal principal plane, to the meridian of the spherical coordinate system centered on the array (i.e., our reference coordinate system). Thus each of these $E_\theta^{(d)}$ components has an $E_\phi^{(d)}$ component that is not necessarily canceled by $E_\phi^{(d)}$ components from other electric dipoles. Each of these $E_\phi^{(d)}$ components sums to the E_ϕ referenced to the spherical frame centered on the array.

Consequently primary cross-polar E_ϕ (i.e., H) polarized waves will likely be generated if the array of electric dipoles is energized.

But only primary cross-polar H is expected, because the $E_\phi^{(d)}$ radiated by each magnetic dipole always lies in horizontal planes in the reference spherical coordinate system. Thus no $E_\theta^{(d)}$ is generated if the magnetic dipoles are energized, and thus there should be no primary cross-polar V associated with the array of magnetic dipoles.

In summary, an array of vertically-oriented electric and magnetic dipoles is the only array that ideally can generate electronically steered copolar beams without primary cross-polar radiation along the copolar beam axis for any beam direction. Nevertheless, there will be secondary cross-polar fields due to practical considerations in the design of the dipoles and their respective feed lines, as well as errors in manufacturing and assembly. Extensive testing of various designs is needed to keep these secondary cross-polar fields as low as possible. Nevertheless, it should be possible to design the elements so secondary cross-polar fields are negligible. If this goal can be achieved, then the correction techniques of Zhang et al., (2009) and Zrnic et al. (2011), can be greatly simplified (i.e., corrections will only be needed to compensate for changes in gain and beamwidth).

Manufacturing slots and electric dipoles for testing at 3.2 GHz allows for a dual polarimetric demonstrator antenna to be adapted to single polarimetric PARs (e.g., the EQ-36) already extensively tested and deployed for military purposes. That is, there would be no need to build all the electronic hardware to field test a demonstrator PPAR. Adapting the slot/dipole array to an existing PAR would allow sooner testing of the PPAR for weather radar purposes.

Fig.2.6i shows a proposed 12x12 array of slot and dipoles that could be manufactured for use as a demonstrator PPAR. The elements are laid out in a staggered configuration in which alternate elements in a column (i.e., z direction) are shifted in the y direction by 0.317λ and the spacing of the elements along a column is 0.5λ; such small spacing eliminates grating sidelobes.
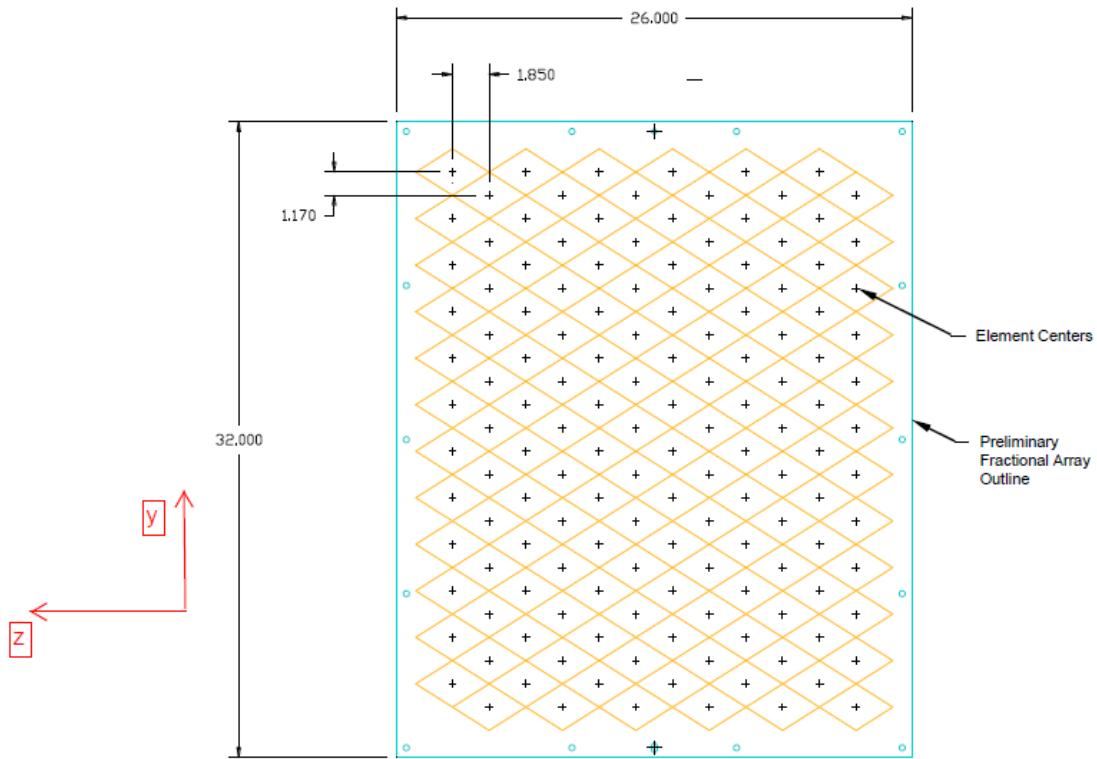
12 elements wide x 12 elements tall = 144 elements

Fig.2.6.i. A layout of a proposed demonstrator array of staggered collinear slot and dipole elements in a 12x12 array The long side of the above array is the top side and dimensions are in inches.

When a PPAR beam is steered azimuthally away from the vertical broadside plane the azimuth beamwidth will increase; at $\pm 45^{o}$ the azimuth beamwidth is 1.4 times broader than the broadside beamwidth. Thus corrections for gain will be necessary for a PPAR to make quantitative measurements of reflectivity factors, Z, no matter the ratio of the broadside beamwidths. But for the full scale PPAR, not for the demonstrator panel, the beamwidth should be no worse in elevation and azimuth, than that 1° presently available with the WSR-88D. This means that at the extreme azimuths of $\pm 45^{o}$ the azimuth beamwidth of the final full sized array needs to be 1°.

But the beamwidth could be allowed to increase as elevation increases because, even with the WSR-88D having a fixed 1° beamwidth, the elevation angular spacing of beams is larger than a beamwidth thus generating gaps in coverage. The larger spacing in elevation is a compromise to have reasonable elevation coverage without compromising the need to complete a volume coverage in less than 5-7 minutes. In short, the increase in beamwidth of a PPAR, and the flexibility to increase the beamwidth by adjusting the aperture distribution as a function of beam elevation angle, would close the coverage gaps in elevation, and is considered to be an advantage as noted in Table 2.1.

2.4.2 Aperture elements

44

The University of Oklahoma under support of NSSL, has theoretically investigated the copolar and cross-polar fields of various elements that can be used to form the array of elements of a PPAR. The elemental aperture could be an open ended waveguide like that used on NSSL's NWRT, or a conducting patch on a dielectric substrate (Section 2.4.3). Some of the results of that investigation are reported here where an aperture element is first discussed.

Some insight into the copolar and the primary cross-polar fields can be gained by considering an aperture in a perfectly conducting plane of infinite extent. Even this problem is difficult to solve because the actual field distribution in the aperture is not precisely known, nor is the distribution of currents on the conducting plane. But by using the field equivalence principle, the actual sources of radiation (e.g., the aperture field and currents on the conducting plane) can be approximated by equivalent electric and magnetic current sources; this often makes the computation of radiation field easier. For example, given an aperture in a perfect electrically conducting plane of infinite extent, it can be shown the only equivalent source is a magnetic current density $M_s = -2\hat{n} \times E_a$ across the aperture. That is, the entire conducting plane surface and its associated surface currents can be removed; here E_a is the electric field in the aperture (not exactly known) and $\hat{n}$ is a unit vector perpendicular to the aperture (Balanis, 2005, Fig.12.5).

For a horizontally polarized rectangular aperture, the longer side lies along the z axis (Fig.2.7a) and for a vertically polarized aperture (Fig.2.7b), the long side is in the y direction. A TE$_{10}$ mode is assumed to propagate inside both waveguides feeding the aperture so a co-sinusoidal distribution exists across the aperture satisfying boundary conditions and approximating the actual aperture field E_a.

The apertures can be arranged in a brick pattern, like that used in NSSL's single polarimetric (i.e., vertical polarization) PAR (i.e., the NWRT). But for a dual polarimetric PAR, the H- and V-polarized apertures would be interlaced to minimize cross-polar coupling. The copolar radiation patterns measured by NSSL (Curtis and Meier, 2009) compare very well with the theoretical patterns that ignored mutual coupling (Zhang and Doviak, 2008). This agreement between theory and measurements suggests that interlaced brick pattern of apertures might have minimal effect due to mutual coupling so that cross-polar fields in the principal planes might be kept well below the -45 dB level as they are for the NWRT.
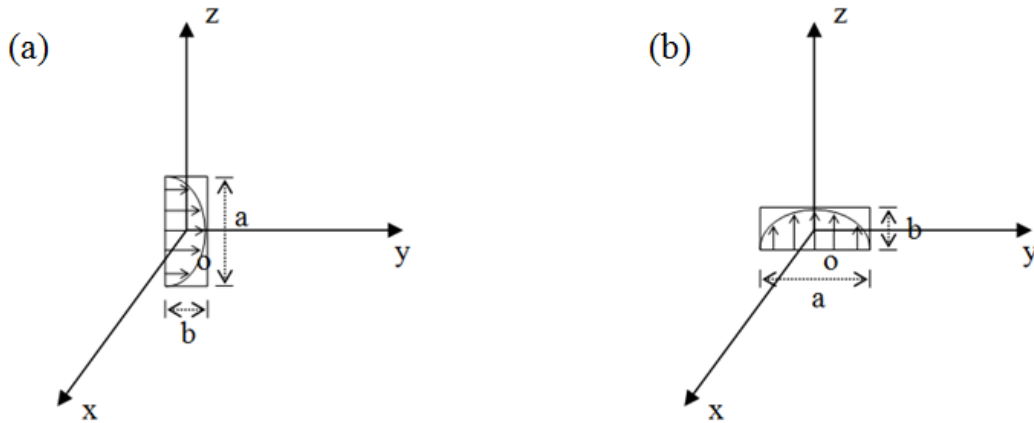
Fig.2.7a Horizontally (a) and vertically (b) polarized rectangular apertures that generate the H and V copolar and cross-polar fields shown in Fig.2.7b.

The approximate copolar and primary cross-polar far fields, caused by a sinusoidal field distribution across a rectangular aperture in an conducting plane of infinite extent, are given by Lei et al. (2012). Although the conducting surface of a MPAR face is of finite size, the array diameter is sufficiently large that the theoretical copolar and cross-polar fields should well represent the stronger component fields expected from measurements. On the other hand, as stated in section 2.2.2, cross-polar fields as weak as 40 to 50 dB below the copolar peak can have significant impact on the accuracy of meteorological measurements if the cross-polar field lies along the beam axis. Thus it is imperative that the amplitude and phase of cross-polar fields be calculated accurately to the levels of 40 to 50 dB below the copolar peak. The results presented here need to be supported by more precise calculations and measurements to insure that levels of cross-polar radiation are within acceptable limits.

The copolar and cross-polar fields of the horizontally and vertically polarized apertures are presented in Fig. 2.7b. For the H-polarized aperture, energized from an H antenna port, it is seen (Fig.2.7b panel c) there is no cross-polar field in any direction. But this result is only a first order approximation because the aperture field is not known exactly. In this case the radiation field everywhere is nearly purely horizontal. However, if a conducting plane of finite size is considered, numerical solutions to the radiation problem show a quad of cross-polar fields with a null of cross-polar radiation along the broadside direction[2].

On the other hand, the vertically polarized aperture has zero cross-polar radiation only along the principal planes (Fig.2.7b, panel d). The primary cross polar field of the vertically polarized aperture is consistent with that measured on NSSL's NWRT (Doviak et al., 2011). Note that although the vertically polarized aperture is simply the horizontally polarized aperture rotated by 90°, the patterns shown in Fig.2.7b are not rotated versions of one another.

---

[2] Private communication from Djordje Mirkovic, CIMMS, University of Oklahoma.

This is because the polarization definition commonly used by radar meteorologists is tied to the spherical coordinate system having it polar axis fixed to the vertical. That is the spherical coordinate unit vector $\vec{a}_\theta$ always lies in a vertical plane whereas the unit vector $\vec{a}_\phi$ always lies in a horizontal plane irrespective of the orientation of the aperture. Thus, electric fields having the $-\vec{a}_\theta$ direction are defined as the vertically V polarized component because these fields lie totally in the vertical plane. Likewise the electric fields having the $\vec{a}_\phi$ direction are defined as horizontally H polarized fields because this direction always lies totally in the horizontal plane. In the context of weather observations with a PPAR, H (i.e., E_ϕ) or V (i.e., E_θ) are the copolar fields only if the H or V antenna port is energized.
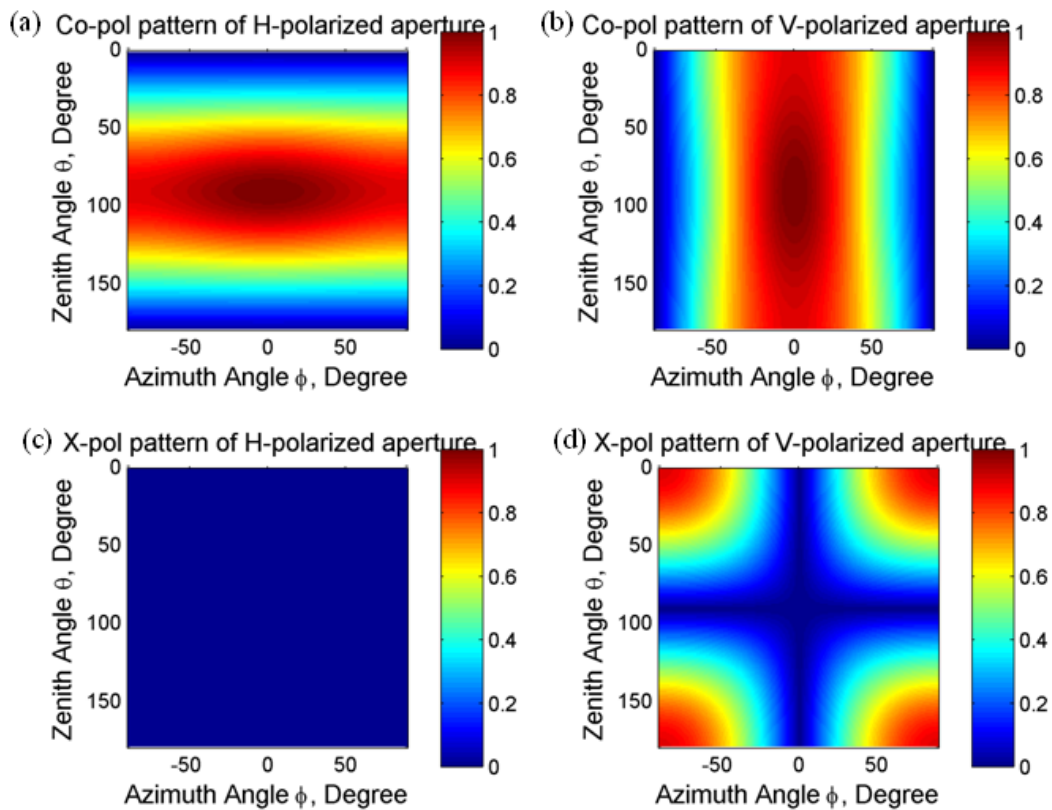

Fig.2.7b The copolar (Co-pol) H and primary cross-polar (X-Pol) V fields (panels a and c) if the H-port of the array element (left panel of Fig.2.6a) is energized, and those respective fields (panels b and d) when the V-port (right panel of Fig.2.6a) is energized. Zenith angle θ is related to the elevation angle $\theta_e = 90 - \theta$.

Primary cross-polar H radiation is generated by the vertically polarized aperture, and thus for an interlaced array of vertically and horizontally polarized apertures the field within a beam directed away from the principal planes will also have primary cross-polar H fields within it. Thus there will be biases in the estimates of polarimetric parameters when aperture antennas are used as elements in a PPAR. Biases in Z_{DR}, the magnitude

47

ρ_{hv} of the copolar correlation coefficient, and the linear depolarization ratio L_{DR} have been calculated by Lei et al., (2012).

Because the WSR-88D cannot provide estimates of L_{DR}, attention here is focused on biases in the estimates of Z_{DR} and ρ_{hv}. The biases depend on the mode of data collection and typically they differ if the SHV or AHV mode is used (L_{DR} is only measured using the AHV mode). Fig. 2.7c shows the Z_{DR} bias if the idealized aperture elements shown in Fig.2.7a are used in a PPAR, and either the AHV (left panel) and SHV (right panel) data collection mode is used. For beam directions near the principal planes there is practically no difference in bias for the two modes of operation. But in either case biases are much more than the intrinsic differential reflectivity. But these horizontal cross-polar components are a result of our definition of cross-polar fields, and not an artifact of the design or manufacturing errors. Because the cross-polar field of the idealized apertures is not an artifact of improper design or orientation of the slots, Z_{DR} bias generated by the cross-polar fields can be corrected (Zhang, et al., 2009; Zrnić, et al., 2011).
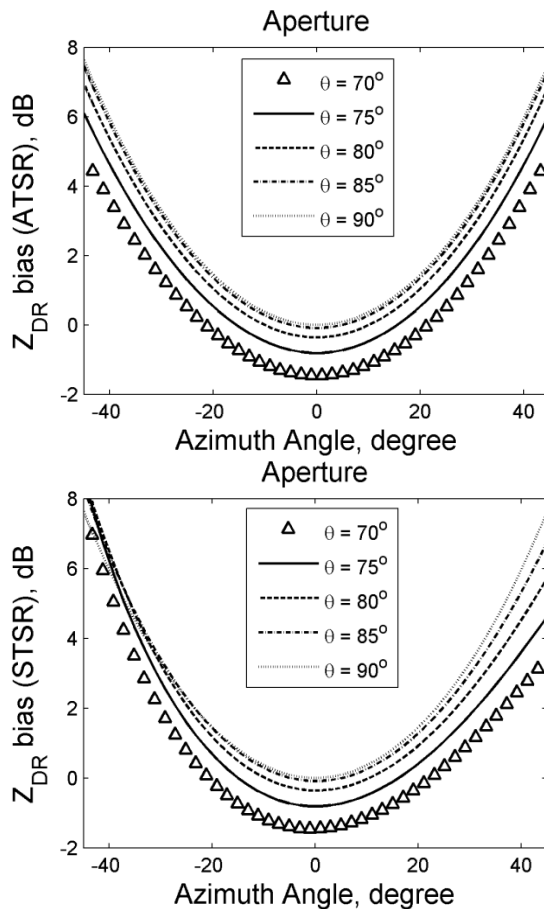

Fig. 2.7c. The dependence of Z_{DR} bias (dB) for the dual polarimetric aperture array element (Fig.2.7a) vs azimuth and zenith angle θ for two data collection modes: AHV (left panel) and SHV (right panel). Transmit H, V amplitude ratio $\gamma = 0$ dB and phase difference $\beta = 0°$, intrinsic $Z_{DR} = 1.0$ dB, and $\rho_{hv} = 0.98$ in all cases.

It is of some interest to compare the cross-polar fields produce by the rectangular aperture with that produced by center-fed parabolic reflector. If the parabolic reflector is illuminated with a *conical* feed horn (i.e., a design used for the WSR-88D), cross-polar radiation in the far field would be present as shown by Zrnic, et al., (2010), even if the conical feed horn and reflector were precisely manufactured and assembled. However, if the reflector is illuminated with crossed magnetic and electric dipoles (i.e., a Huygens source) at the reflector's focal point, it is shown there is no cross-polar field in the antenna's aperture (Jones, 1954). That is, if the electric dipole is horizontal (vertical) and the magnetic dipole is vertical (horizontal) the field in the aperture is purely horizontal (vertical). That is there is no cross-polar field in the aperture.
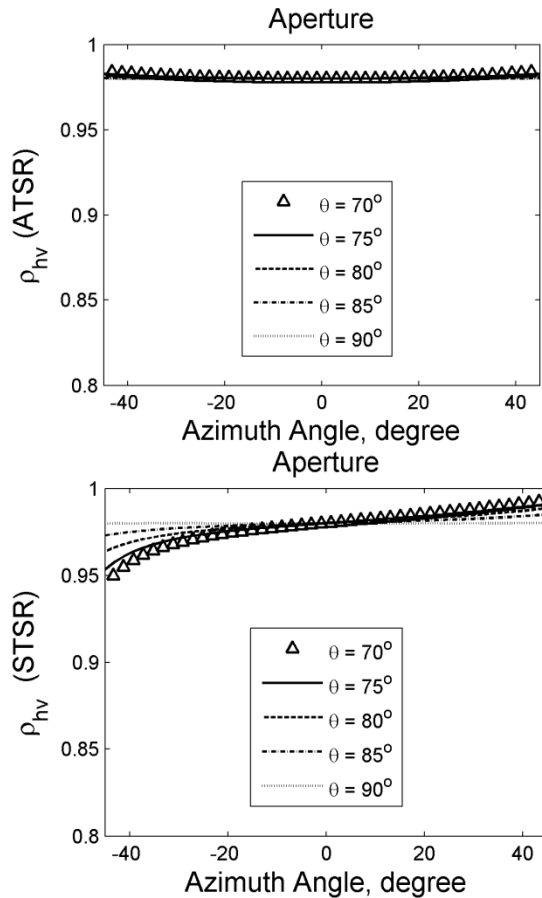

Fig. 2.7d. The dependence of the copolar correlation coefficient ρ_{hv} for a dual polarimetric array element (Fig.2.7a) vs azimuth and zenith angle θ for two data collection modes. All parameters are the same as in Fig.2.7c.

Furthermore, the horizontally polarized aperture has no cross-polar radiation anywhere, consistent with the fact that there is no cross-polar (i.e., no $\vec{a}_\theta$ or V polarized component) radiation from a horizontally polarized rectangular aperture antenna (i.e., Fig. 2.7c). This is also consistent with the fact that the vertically oriented slot produces no

primary cross-polar radiation. But if the reflector and feed are rotated 90° so that the aperture has purely vertically polarized fields, there will be cross-polar radiation (i.e., H fields) outside the principal planes. This is consistent with Fig.2.7b (panel d).

The reason primary cross-polar fields are present in the latter case and not in the former is related to the fact that our definition of cross-polar fields is based on fields generated by energizing the H and V ports of an antenna and defining local H and V polarized fields as those along the unit vectors $\vec{a}_\phi$ and $\vec{a}_\theta$ of a reference spherical coordinate system centered on the array center and with the polar axis z vertical. This definition is consistent with definition 2 of Ludwig (1973), but it is not the one (i.e., definition 3) most commonly used by antenna engineers. With definition 3, a vertical dipole generates cross-polar radiation, whereas using the definition presented herein, there is no cross-polar radiation emitted by a vertical dipole.

To illustrate consider a vertical dipole on an elevation-over-azimuth pedestal and a vertical (horizontal) dipole to receive and measure the copolar (cross-polar) field. At broadside the vertical dipole receives the maximum copolar radiation whereas the horizontal dipole will receive no cross-polar radiation. But as the elevation angle of the vertical dipole under test is increased, the copolar radiation will decrease but cross-polar radiation remains zero. However, if the azimuth angle is changed by 90° from broadside while the elevation angle remains non-zero, the cross-polar field will increase to a maximum because the dipole under test presents a maximum horizontal aspect viewed from the horizontally oriented receiving dipole.

It is stressed that Ludwig's definition 2 is to be used, because it is rooted in the observation of precipitation particles that typically have an axis of symmetry that is vertical, which also form the polar axis of definition 2 used to define the cross-polar field.

2.4.3 Patch elements

Although an array of horn apertures or slots in waveguides appear to provide acceptably low secondary cross-polar coupling, and electric and magnetic dipoles ideally have no primary cross-polar field anywhere and appear to have low secondary cross-polar radiation at the lowest elevation angles where quantitative measurements are most crucial, the cost of construction these array elements is higher than, for example, the manufacturing of surface-mounted elements such as patch type antennas. On the other hand, patch elements have less bandwidth, are more susceptible to variations in gain and phase changes with temperature variations, and as a consequence might have higher secondary cross-polar fields.

The ideal patch antenna considered by Lei et al., (2012) as an element in a PPAR consists of an electrically conducting ground plane, a substrate of high dielectric permittivity, and an electrically conducting square patch on top forming an open-ended cavity (Fig.2.8a). Because the patch's substrate thickness is much thinner than the free

space wavelength, and because the patch and ground plane are nearly perfect conducting surfaces, the four sides of this open-ended cavity can be modeled as nearly perfect magnetic walls at which the magnetic field vanishes.
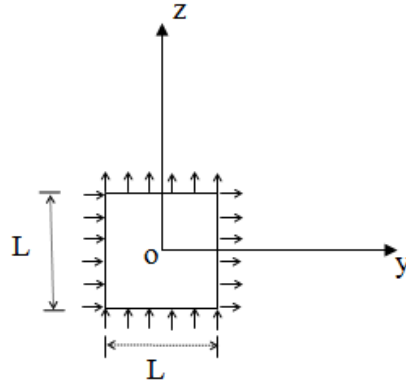

Fig. 2.8a.Top view of a dual-polarized square patch showing the fringe fields of the open-ended cavity if both H and V ports (not shown) are energized.

The field distribution within this rectangular cavity is described as Transverse Magnetic TM_{mnp} in which m, n, and p designate the number of half cycles of electric field change in the x, y, and z directions (m = 0 for the patch in Fig.2.8a). TM_{001} has one half cycle of field change in the z direction (p =1) whereas the TM_{010} mode has one half cycle of field change in the y direction. Radiation from this cavity is due to fringe fields at the open ends. Properly placed feed lines excite either the TM_{001} or TM_{010} modes, but Fig.2.8a shows the fringe fields that contribute to both H and V copolar field when both modes are energized. But either mode can be separately excited (e.g., if the AHV mode is used).

In case only the TM_{010} mode is energized, the fringe fields along the left and right sides would remain as shown, but the fringe fields shown along the upper and lower sides would vanish. The remaining y-directed fringe fields contribute to the copolar H field. Although the fringe fields associated with the TM_{001} mode vanish at the upper and lower edges, there would remain a pair of fringe fields (not shown) along the upper and lower edges of the patch associated with the TM_{010} mode. But these fringe fields have a half wavelength sinusoidal distribution along each edge. Thus they do not contribute to copolar radiation along the boresight, but contribute to the primary cross-polar and copolar radiation; these fringe fields are ignored in Lei et al., (2012).

Thus the radiation field of a patch element is calculated by assuming uniform fringe fields along each pair of opposing edges where the fringe fields can be replaced with magnetic currents. Thus a pair of z directed magnetic currents on the left and right edges or slots of the cavity, energized in the TM_{010}, are spaced L_e apart (L_e is an effective length slightly larger than L the physical patch dimensions; $L = 0.95 \, L_e$ is assumed). Both

magnetic currents radiate principally horizontally polarized copolar fields (Fig.2.8a). To a first order approximation, the pair of slots acts like a pair of horizontally narrow apertures, or as a pair of magnetic dipoles, in a two-element array. The calculation of the far field for this model shows no cross-polar radiation anywhere (Fig.2.8c). But the absence of cross-polar radiation from the pair of vertically directed magnetic currents is consistent with the absence of cross-polar radiation from a vertical magnetic dipole (Section 2.3.1), as well as with the absence of cross-polar fields radiated by a horizontally polarized aperture (i.e., a vertical directed magnetic current sheet) as shown Section 2.4.2 (Fig.2.7b panel c). But if the TM_{010} cross-polar fringe fields along the upper and lower slots are considered, it is hypothesized there would be a quad of cross-polar fields of opposite polarity symmetrically distributed about the copolar beam.

If the TM_{001} mode is energized, V copolar radiation is generated (Fig.2.8b panel b) by the pair of magnetic currents associated with fringe fields at the upper and lower patch edges. But, as with aperture antennas, the co- and cross-polarization patterns are
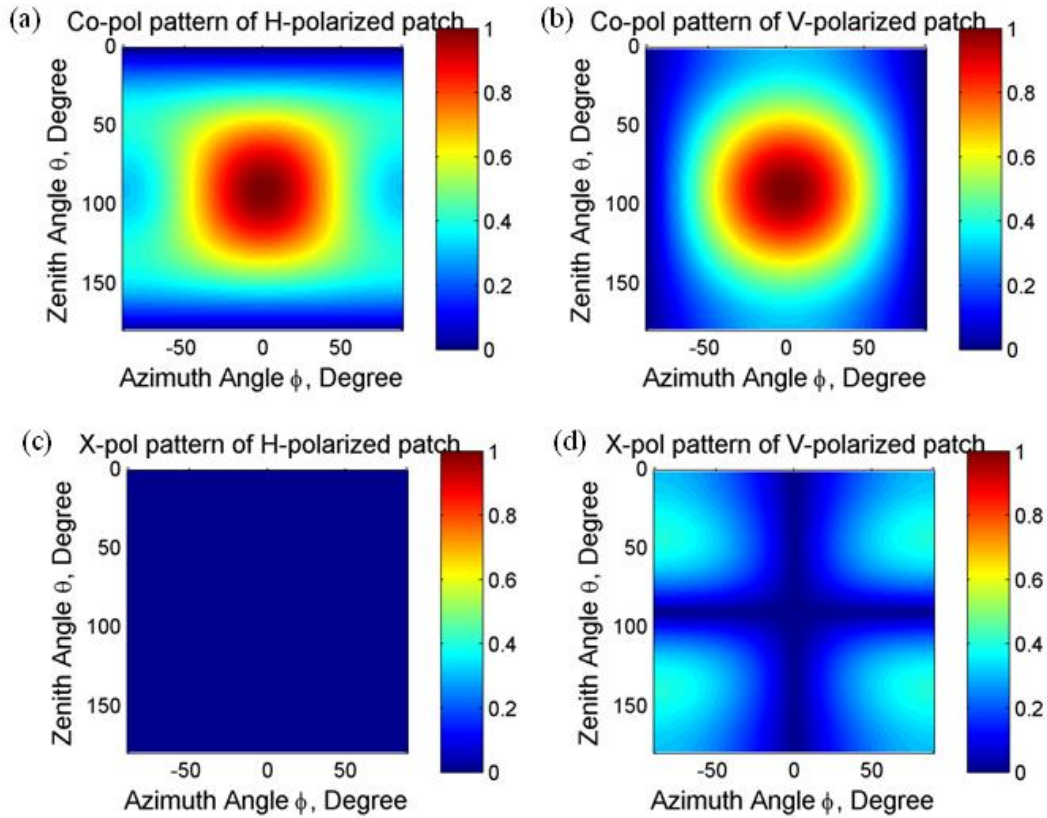

Fig.2.8b The copolar (Co-pol) and cross-polar (X-Pol) fields when the H-port (TM_{010} mode) of the square patch array element is energized (panels a and c), and that when the V-port (TM_{001} mode) is energized (panels b and c). (physical length: $L = 0.38\lambda_o$, effective length: $L_e = 0.40\lambda_o$).

not 90$^{\text{o}}$ rotated versions of one another. This is so because the coordinate system that defines the co-polar and cross-polar fields does not rotate; this definition of copolar and cross-polar fields is consistent with Definition 2 in Ludwig (1973). That is, we define horizontally polarized fields (i.e., E_{ϕ}) as cross-polar radiation if the V antenna port is only energized, and vertically polarized fields (i.e., E_{θ}) as cross-polar radiation if only the H antenna port is energized. Thus cross-polar field (Fig.2.8b panel d) along boresight for beams electronically steered from the principal planes is considered, as stated earlier, primary cross-polar fields.

Although the cavity model approximates the actual fields of the patch, it has been shown input admittance, resonant frequencies, and the copolar radiation patterns of the model cavity compare well with measurements (Balanis, Section 14.2.2, 2005). Such good agreement, however, is unlikely to be seen when comparing measured and theoretical cross-polar patterns.

The primary cross-polar fields generated when the V port of the patch is energized creates biases in Z_{DR} and ρ_{hv} if a PAR uses the patch as elements. Secondary cross-polar fields can be generated if there are manufacturing and assembly defects. The biases in Z_{DR} and ρ_{hv} are functions of the element's radiation pattern, beam direction, the copolar correlation coefficient, and the array factor for the two pairs of radiating elements of the patch. Fig.2.8c (top panels) show the Z_{DR} bias for an array of patch elements operated in the AHV and SHV modes of data collection. For these figures the patch size was selected to be $L = 0.38\lambda_{\text{o}}$ because it produced the smallest span of biases both in Z_{DR} and ρ_{hv} for zenith angles near 90$^{\text{o}}$. Thus the minimal bias corrections, if any, might be needed.
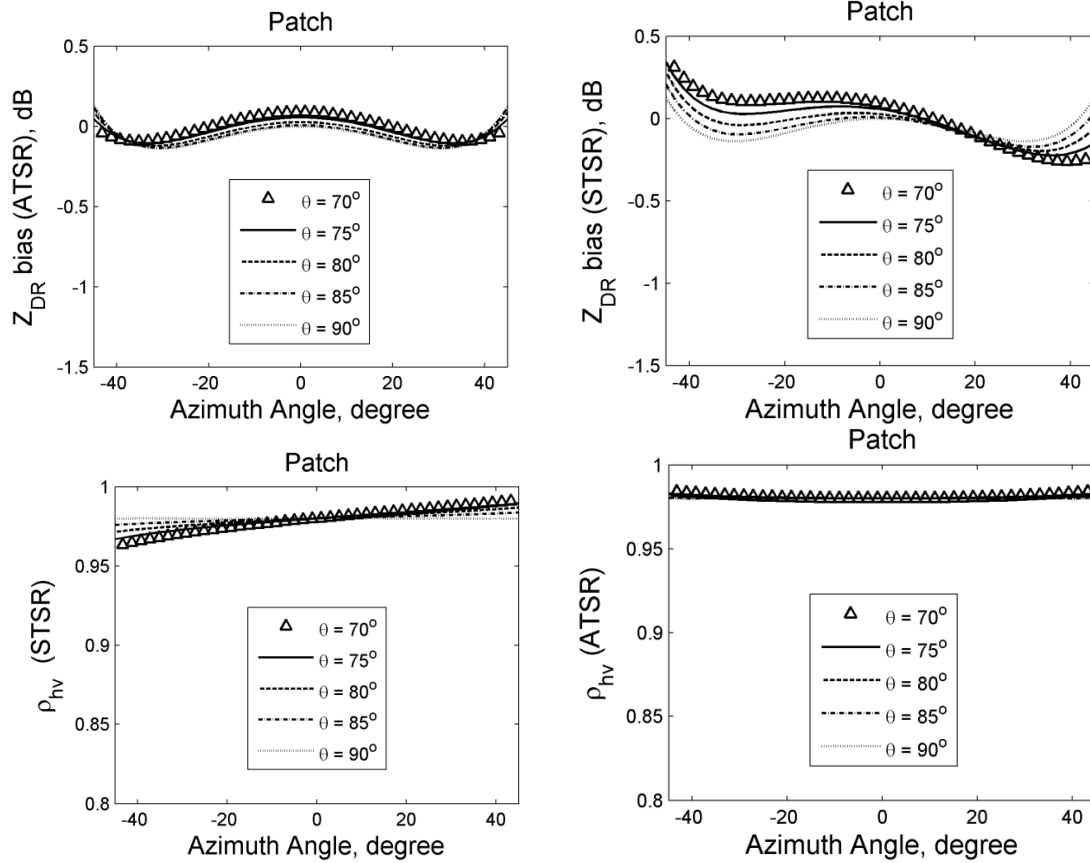
Fig. 2.8c The dependence of Z_{DR} bias (dB; top two panels) and the copolar correlation coefficient ρ_{hv} (bottom two panels) for a dual polarimetric square patch array element ($L = 0.38\lambda_o$) on an infinite ground plane vs azimuth and zenith angle θ for the AHV (left panels) and SHV (right panels) modes of data collection. Transmit H, V amplitude ratio $\gamma = 0$dB and phase difference $\beta = 0^o$, intrinsic $Z_{DR} = 1.0$ dB, and $\rho_{hv} = 0.98$ in all cases.

2.5 Summary

The array element is a fundamental building block of any phased array antenna. Of the various polarimetric array elements examined herein, the only element that appears to offer the potential of having primary cross-polar fields at least as low as, or even lower than, that of the center-fed parabolic reflector antenna (used for the WSR-88D polarimetric radar) for any beam direction is the slot (magnetic dipole) and electric dipole having parallel axes. It is the only ideal element when used with a planar array that can transmit copolar H (V) and receive copolar H (V) on one port while receiving cross-polar V (H) radiation on the orthogonal V (H) port. If the slot/dipole is practically achievable, bias corrections as suggested by Zhang et al. (2009) and Zrnic, et al., (2011) can be simplified

Cylindrical and planar phased arrays are two candidate antennas to which the chosen element can be applied to form either a Cylindrical Polarimetric Phased Array Radar (CPPAR), or a Planar Polarimetric Phased Array Radar (PPPAR). A comparison of the tradeoffs of these two approaches has been published by Zhang et al. (2011). In

summary, the CPPAR allows simultaneous multi-beams to optimally utilize the antenna resources for fast data update while maintaining high quality polarimetric data. This is so, because the beam characteristics are the same at all azimuth angles for each elevation, allowing for simplified calibration.

Furthermore, CPPAR maintains the same polarization characteristics with axial symmetry (i.e., the beam shape and widths do not change with azimuth). Because the beam of the CPPAR remains in the principal planes, theoretically no cross-polar radiation exists along any boresight no matter which array element (i.e., patch, aperture, etc.) is chosen for the antenna, and no matter the direction of the beam. Thus one port of the CPPAR can be used to transmit and receive copolar radiation whereas the other port receives cross-polar radiation for any beam direction. The CPPAR might allow all beams to have the same frequency and thus provide a more efficient use of spectral space because all the beams (e.g., four) are always 90° apart.

For a PPPAR that takes advantage of its beam agility to have independent scanning for beams from each face, the side-by-side beams are likely to interfere when pointed far from broadside and nearly in the same direction; thus at least two separate frequencies will likely be required. The most significant problem with PPPAR is the need to develop methods to remove measurement bias due to many changes in beam characteristics as a function of pointing direction. It is crucial for Z_{DR} signatures to be solely those due to the hydrometeors. Other advantages and disadvantages of the CPPAR and PPPAR are presented in Zhang et al. (2011).

Future work should employ a full wave solution to obtain a more accurate representation of the cross-polar patterns for dipoles, apertures, and patches. It is crucial that measurements of copolar and cross-polar fields accurate at least 40 dB below the copolar peak be made. Measurements of both cross-polar amplitude and phase are extremely important. For example, the relative phase between the copolar and cross-polar fields can affect, by more than an order of magnitude, the upper limit of allowable cross-polar radiation that eliminates significant bias in polarimetric parameter estimates due to cross-polar radiation. In addition, because it is difficult to isolate the H and V channels of a PPAR, the layout and of H and V polarized apertures in an array and their respected feed lines needs to be carefully evaluated to minimize coupling.

3. Polarimetric issues on agile beam PAR

A summary of pertinent issues concerning polarimetric PARs is presented herein. This section supplements the material presented in Section 2 which focuses on broader issues of observing weather with polarimetric radar and examines alternative approaches for array elements. In this section, a theory is presented so that the various tradeoffs of different implementations of polarimetric measurements can be compared.

First a quick review and comparison with polarization geometry on standard parabolic reflector antennas is given (section 3.1). Then in section 3.1.1 requirements for cross polar isolation for a parabolic reflector antenna are explained. That section is pertinent because it applies to any antenna (including the phased array), thus implications for the PAR are discussed. The polarization basis on the WSR-88D radar is linear "horizontal" (H) and "vertical" (V) and the mode of operation is "simultaneous transmission and reception of H and V waves (SHV). The cross-polar requirements placed on antenna performance are much more stringent in this mode than in the mode whereby the H and V polarizations are transmitted sequentially but echoes are received simultaneously (i.e., the AHV mode).

A newly designed PAR can have flexibility to produce more complex polarization modes. Principal criteria determining the mode will be rooted in tradeoffs between requirements, practicalities, and cost. As discussed in the introduction three PAR antennas are candidates for weather observations. For two of these (PAR_{EM} and PAR_{CYL}) the polarization of electric fields is equivalent to the one a mechanically steered antenna would produce. But the PAR_{EE} requires accounting for the inherent non-orthogonally of the electric fields in directions out of the principal planes. Thus the key issues in polarimetric performance of the PAR_{EE} boil down to three factors: 1) the change of polarization of the intended transmitted Horizontal (i.e., E_φ) or Vertical (i.e., E_θ) electric field which depends on the pointing direction (more discussion on this coupling mechanism is given in the next section), 2) coupling of polarizations within the radar, and 3) the anisotropy of the propagation medium. The second and third issues are common to the three PARs and radars with parabolic dish antennas (the coupling within the radar might be stronger for a solid state PAR with printed circuits). The effects of polarization change due to beam steering are documented in (Zhang et al, 2009, Zrnic et al. 2011, Galletti and Zrnic 2011, and Lei, et al., 2012).

3.1 Parabolic dish vs phased array antenna

Assume that the plane of the phased array is vertical. Then, for both the parabolic dish and phased array (PAR_{EE}) antenna the "vertical" component of the transmitted electric field (at a location far from the antenna) is always tangent to the meridian (great circle) connecting the range location to the pole over the radar. That is, a transmitted wave, vertically polarized along the array's broadside direction, remains in the vertical plane as the beam is electronically steered. This is true for any pointing direction of the two antennas (parabolic dish and PA). Hence if "vertically" (henceforth vertically polarized waves will mean the wave's electric field lies in a vertical plane) polarized fields are transmitted, the polarization of echoes would on the average be vertical because hydrometeors have zero mean canting angle (Doviak, et al., 1998).

56

The "horizontal" direction in case of a parabolic dish mounted on an elevation over azimuth pedestal does not have such simple correspondence to the intended "horizontal" component emitted by the horizontally polarized elements of the PAR$_{EE}$; this is explained next. For the mechanically steered beam define a local coordinate system at the range r such that the z axis is in the direction of the beam's axis and the x axis is horizontal and thus always perpendicular to the beam direction; that is, as the beam direction changes so does this coordinate system. In this case, if the aperture of the parabolic dish is horizontally polarized, the polarization of the field along the beam axis is always parallel to the horizontal plane at the radar, independent of the beam direction.

Contrast this to a planar phase array antenna for which the plane of the array is vertically oriented (i.e., perpendicular to the earth's surface). For such phased array antenna the electric field radiated along the beam by horizontally polarized array elements is parallel to the earth surface only if the beam is either in the vertical plane perpendicular to the antenna aperture (i.e., the plane of the array), or in the horizontal plane; these are the so-called principal planes. Generally, for beams pointed in any other direction, the electric field generated by the horizontally polarized elements, is tangent to the great circle connecting the range location to the poles (these are defined to be on the line parallel to the horizontal plane at the radar and in the plane of the array aperture). As the beam is pointed electronically away from the principal planes, the electric field along the beam will not be along the intended horizontal direction. **Hence the wave transmitted by horizontally polarized array elements can contain both a horizontal and a vertical component**. *That is, the transmitted wave's polarization is a function of the electronically steered direction; this is not the case for a mechanical steered beam. To maintain the state of polarization independent of beam direction requires, in general, adjustment of the excitation level of the transmitting elements for each beam direction.*

Of critical importance to the favorable utility of a polarimetric weather radar is the selection of polarization basis and its practical implementation. As mentioned in the previous paragraph, the wave's polarization changes in the defined V, H coordinate system (i.e., E_θ, E_ϕ; a spherical coordinate system with a vertical polar axis at the radar) for a phased array antenna as the beam direction changes. Considerations for the choice of polarimetric basis and a few system design options are described in the NSSL report (Doviak and Zrnic 1998) and in the paper by Doviak et al. (2000). In that report the circular and linear polarimetric bases are compared. It is demonstrated that any apparent advantage of the circular polarization basis vanishes in the presence of significant precipitation along the propagation path. Furthermore, the linear polarization basis is best suited for quantitative measurement of rainfall and classification of hydrometeor types because it is least affected by propagation effects. Therefore, the choice of the transmitted wave polarization rests with the linear H, V basis.

Quantification of polarization change and a description of how to correct its effects are describe in the paper by Zhang et al. (2009). Therein it is assumed that the radiating elements are dipoles, there is no mutual coupling between the dipoles, and the effects of Doppler shift in the AHV mode are ignored. The results given by Zhang et al., (2009) are supplemented by Zrnić, et al., (2011) to account for the effects of Doppler shift, and by Lei et al., (2012) where idealized patch and aperture phased array elements are considered.

57

Subject Study

PAR$_{EE}$: Further quantitative evaluation of the suggested correction needs to be made for practical radiating elements wherein: 1) the copolar and cross-polar patterns differ from those of ideal dipoles, and 2) there is mutual coupling between the elements. This theoretical evaluation should also consider the array factor for a candidate antenna. Complicating further the matter are designs which use overlapping sub arrays to form the antenna. Furthermore, tests and measurements should be made on prototype arrays of small size to evaluate principle design objectives.

PAR$_{EM}$: This configuration is being developed by BCI and Lockheed Martin Co. Measurements on single radiating elements and on panels need to be made and evaluated. Alternate realizations of the Electric-Magnetic dipole (or equivalent) should be explored.

3.1.1 Polarization coupling in case of a parabolic dish

In Zrnić et al. (2010) requirements for the cross-polar performance of antennas are discussed. *The essence of this paper and pertinence to the PAR follow.*

It is shown that **both the angular distribution** of the cross-polar radiation and **the integral power** under the cross-polar pattern affect the bias in the polarimetric variables. That is, the cross-polar isolation or depolarization ratio (ratio of power within the cross-polar pattern to the power within the copolar pattern) is only one measure of the performance, and by itself it is not complete. It could even be misleading.

The following two types of cross-polar pattern found on some antennas are: Type 1 wherein the main lobe of cross-polar radiation coaxial with the main lobe of copolar radiation, and Type 2 wherein the cross-polar pattern has four principle lobes symmetrically located with respect to the axis of the main lobe of the copolar pattern. For the same depolarization ratio the type 1 pattern produces much larger bias in the polarimetric variables. In practice there appears to be antennas for which the cross-polar pattern is a superposition of the two types (that is there is a cross-polar pattern peak centered on the copolar peak plus an even number of lobes axially symmetric with respect to the main lobe peak). The coaxial cross-polar lobe can be caused by a tilt in the feed horn. If this is the only lobe of cross-polar radiation, the cross-polar peak must be more than 43 dB below the copolar peak to satisfy bias requirements for differential reflectivity (Section 2.2.2) .

3.1.2 Implications for the PAR

Now assume that the phased array antenna has type 1) pattern and both H and V polarization are simultaneously transmitted. Then a better (i.e., smaller biases of polarimetric variables such as Z_{DR}) polarimetric performance will be achieved if the phase of the cross-polar lobe equals or is opposite to the phase of the copolar lobe. *If these conditions are achievable in practice – 30 dB of isolation (depolarization) would meet performance requirements (this assumes the cross-polar lobe has the same width as the copolar lobe, and contribution from sidelobes is negligible). Polarimetric parameters could be satisfactory even for isolation as low as -25 dB if the copolar H and V are transmitted in a $\pm 45^o$ slant linear mode.*

If the phased array antenna is of type 2) (the pattern has an even number of cross-polar lobes of equal magnitude but alternating phases, and cross polar lobes axially symmetric with respect to the main lobe of width about equal to cross-polar lobe width)

then *the cross-polar to copolar peak power ratio due to this pattern could be as high as -20 dB and the performance could still be acceptable*.

In practice we expect that the cross-polar pattern will be a superposition of the type 1 and type 2. But at arbitrary pointing directions the cross-polar lobes of type 2 pattern will not have the same magnitudes and will not be exactly symmetric about the axis of the copolar main lobe. This and the presence of a peak on axis of the copolar pattern will degrade the performance such that a smaller cross-polar to copolar power ratio would be required. That is, a better polarization performance of the antenna might be needed.

3.1.3 Definitions pertinent to PAR

Two modes of polarimetric measurements in the linear polarization basis produce useful information about precipitation at volume update rates compatible with rates used by the WSR-88D. These modes are 1) Simultaneous transmission and reception of Horizontally and Vertically polarized fields (SHV mode) and 2) Alternate transmission but simultaneous reception of the H and V polarized waves (AHV). The SHV mode is not fully polarimetric as it does not measure cross-polar components unless some more sophisticated (and untested) transmitted pulse modulation and/or sequence is utilized (Bharadwaj and Chandrasekar 2007). The preferred mode of operation is the SHV mainly because it is completely compatible with the existing signal processing and meteorological algorithms on the network. It is also easy to implement on conventional radars.

Because the polarization (in the H, V basis) of the fields generated by the phased array antenna depends on the beam direction if the H port is only energized, and to avoid confusion in nomenclature, we define two modes of operation specific to the PAR. One is the Alternating mode (ALT) in which the H and V *ports* of the array elements are alternately energized from transmitted pulse to transmitted pulse. The other is the mode (SIM) in which both H and V *ports* are simultaneously energized. The SIM and ALT modes have obvious analogy with the SHV and AHV polarization modes used on the WSR-88D. The reasons for using different nomenclatures for modes of polarimetric data collection with PAR and WSR-88D is as follows.

The AHV mode for the center fed parabolic reflector antenna means we alternately transmit but simultaneously receive H and V polarized fields when we excite and receive on the H and V ports of the antenna. If we only excite the H port, only the H field will be transmitted along the beam axis for every direction the beam. Furthermore the principal backscatter field is the copolar H field with minimal reception V fields due to small fluctuations of hydrometeor's canting angle. Small cross-polar fields typically can be ignored (Zrnic, et al., 2010).

However for a PAR, the idea of H and V ports lose its meaning because if the "H" port is excited, H polarized waves will only be transmitted along the beam axis for the broadside direction. If the beam is steered away from broadside, both H and V waves are transmitted. Thus we use the term ALT simply to indicate that although the so-called "H" port of the antenna is only energized both polarizations are transmitted; H and V are not alternately transmitted.

Defining H and V ports of a PAR only has meaning for one beam direction; broadside. Thus for the PAR we use the term ALT in place of AHV. Similar arguments led us to replace SHV with SIM when we energize both "H" and "V" ports of a PAR. In the sequel we use SIM and/or SHV interchangeably but try to stay with SHV and AHV when referring to the WSR-88D.

In using either the ALT or SIM mode, the excitation of each port could be fixed, or adjusted, unlike that for the SHV mode of the WSR-88D that transmits simultaneously H and V polarized waves of equal intensity. For the simpler fixed mode of excitation, the polarization of the wave will be function of the electronically steered beam direction. In the adjusted SIM mode, the relative excitation of the ports can be altered so that the polarization of the transmitted wave along any boresight will be fixed (e.g., H and V of equal magnitude). Maintaining equal H and V polarization along the boresight and operation in the SIM mode requires less computation to retrieve the polarimetric parameters (e.g., Z_{DR}), but at the considerable complication and expense of having to control the level of transmitted power and receiver gain of the H and V ports for each array element (Zrnić et al. 2011).

Because a V component of radiation is transmitted from the 'H' radiator if the beam is electronically steered from the principal planes, the so called 'H' and 'V' channels of a PAR are pseudo H and V channels. That is, these port designations bear no relation to the polarization along the electronically steered beam as it does for the mechanically steered beam of the WSR-88D. Furthermore, on reception, both 'H' and 'V' channels of a PAR received V polarized echoes, although only the 'H' channel receives H polarized echoes. Only the PAR_{EM} array has the property that H and V channels are uncoupled both in transmission and reception.

The ALT mode on the PAR (either without or with adjustments of the H and V port excitations to achieve equal H and V transmitted fields) can be configured to receive both the copolar and cross-polar components and thus the PAR can be fully polarimetric. Nonetheless, because the cross-polar returns have typically 30 dB lower power than the copolar returns, the range coverage where these would be useful is reduced. It is therefore doubtful that cross polar variables would be recommended for initial inclusion to the weather PAR. Thus the principal output from this mode would likely be the H and V copolar power components $P_h \propto \left\langle \left| s_{hh} \right|^2 \right\rangle$ and $P_v \propto \left\langle \left| s_{vv} \right|^2 \right\rangle$, and the copolar correlation coefficient $\rho_{hv}(0) = \left\langle s_{vv} s_{hh}^* \right\rangle \big/ \sqrt{P_h P_v}$, variables presently available on the WSR-88D.

3.2 Compensating for the change in polarization caused by planar PAR

Fig. 3.1 depicts two orthogonal electric dipoles and the field generated in an arbitrary direction with obvious implication for the $PAR_{EE.}$ The y and z coordinates at the array element correspond to H and V directions of the dipole elements. The configuration in Fig. 3.1 is applicable to patch and slot elements (Sections 2.4.2; 2.4.3). Nonetheless there are configurations wherein a magnetic dipole is parallel with an electric dipole (under development at Lockheed Martin and BCI) referred to as PAR_{EM}.

In that case the electric fields far from the antenna are orthogonal and no "zero order" correction (described herein) is needed.
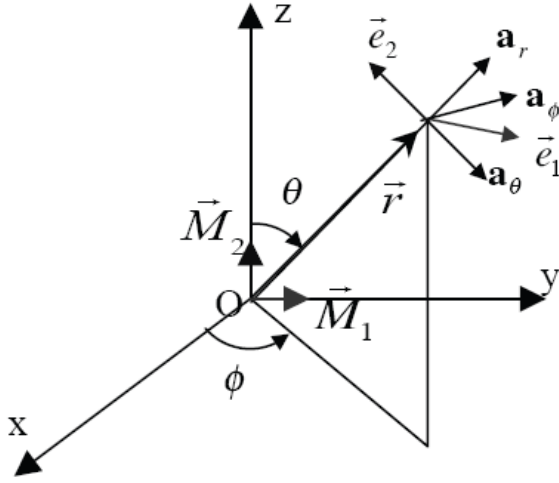

Fig. 3.1 Geometry: Phased array antenna is at the origin and the plane of the array is in the z,y plane. The pointing direction is $\vec{r}$, the electric dipole moments and angles are indicated.

Details of the correction procedures are in the papers by Zhang et al. (2009) and Zrnic et al. (2011). A compact summary follows.

3.2.1 ALT mode

   To compensate the inherent change in polarization as a function of beam direction, adjustments of excitation to both the H and V ports have been proposed (Zrnic, et al., 2011). In that case the horizontally and vertically polarized fields at scatterers' location can be made equal and independent of the beam direction, just the same as it would be for a mechanically steered beam. Nevertheless, additional corrections need to be made in the receiver to obtain the polarimetric variables as discussed in section 3.2.1a. But, from a practical point of view, it is much simpler to fix the excitations of the H and V ports and to make all the necessary corrections to the received signals as shown in section 3.2.1b.

3.2.1.1 Adjustment on transmission and reception

   We list equations (8b and 8c) from Zrnic et al. (2011) which quantify the adjustments (amplitude and phase of voltages) on the horizontally and vertically oriented electric dipoles which were considered as array radiating elements. In general the adjusted electric dipole moments M_H^a and M_V^a are

$$M_H^a = M_1 / \cos\varphi \tag{3.1a}$$

$$M_V^a = M_1(\cos\theta\sin\varphi)/(\sin\theta\cos\varphi) + M_2/\sin\theta \tag{3.1b}$$

61

where M_1 and M_2 are independent sources respectively for the pseudo H and V ports of the PPAR. Typically $M_1 = M_2$, but we distinguish these in (3) to make clear how source weighting is distributed between the dipoles so that the H and V fields are of equal intensity independent of beam direction.

In the ALT mode the dipole moments (say at time i and $i+1$) are

$$\text{Time } i: \quad M_H^a(i) = M_1/\cos\varphi \text{ and } M_V^a(i) = M_1(\cos\theta\sin\varphi)/(\sin\theta\cos\varphi) \quad (3.2a)$$

$$\text{Time } i+1: \quad M_H^a(i+1) = 0 \text{ and } M_V^a(i+1) = M_2/\sin\theta. \quad (3.2b)$$

In the sequel we drop the subscripts "1" and "2", and equate $M_1 = M_2 = M$. The adjustment (3.2) is made on each transmitted pulse so that the H and V fields incident on a resolution volume at $\vec{r}$ (in the direction ϕ, θ) would be exactly the same as fields produced along the broadside direction by the two dipoles having moments M. This is equivalent to fields from a mechanically steered beam because the electric fields as function of direction are given by the matrix product

$$\mathbf{P}\begin{bmatrix} M_H^a \\ M_V^a \end{bmatrix} = \begin{bmatrix} \cos\phi & 0 \\ -\cos\theta\sin\phi & \sin\theta \end{bmatrix}\begin{bmatrix} M_H^a \\ M_V^a \end{bmatrix}. \quad (3.3)$$

One can quickly see that introduction of (3.2a) into (3.3) produces horizontally polarized fields and introduction of 3.2b produces vertically polarized fields of magnitude equal to that of the H field.

Because beam forming is a linear operation, adjustments (3.2) can be made on individual array elements, on signals feeding a sub-array, or on the pair of composite signals feeding the H and V ports of the entire array. Obviously the latter is the simplest if a corporate network (i.e., the network that divides and distributes the signals to each power amplifiers at each array element) is in place. On the other hand, if the PAR antenna is calibrated using the mutual coupling technique (Aumann et al., 1989), adjustments need to be made on individual array elements.

Fields of both polarizations (H and V) must be measured on reception and correction can be done from *pulse to pulse* before computing the polarimetric variables (see Zrnic et al. 2011, Sec III A.1). Computationally less demanding is a procedure whereby *estimates of powers and covariances* are first made and from these the polarimetric variables are computed (Zrnic et al. 2011 Sec III A.2). Again both can be done on signals from each of the array element, signals from sub-arrays, or on signals from the full array. The system is fully polarimetric and the obtained polarimetric variables have no bias due to inherent polarization change.

The differential phase and Doppler shift are coupled and can be resolved using techniques similar to the ones implemented in 1991 on the NSSL Cimarron dual polarization radar (Zahrai and Zrnic 1993).

Adjustment on transmission other than the one presented here are possible and worthy further scrutiny. For example adjustment of the level of excitation to one of the dipoles or compensation of gains without compensation of polarization could be made.

Subject study

PAR$_{EE}$: The above described procedure has never been implemented on PAR radar. Compensation on transmission as function of direction might have practical (economic) consequences. However it is worth further study because it is conceptually simplest and can provide a benchmark for comparisons. Its use of energy is not most efficient. Control of amplitudes and phases on each element to achieve the desired balance might be problematic. Thus much experimental work needs to be done. Inclusion into the PAR system design might pose additional challenges. The correction equations are valid for Hertzian dipoles. Currently there is no consensus on which type of radiators is most suitable. Patch antennas, Hertzian dipoles in a slot aperture, and other types of elements are being tested. Measurements of the element pattern and pattern of the full array are needed to determine precisely the correction factors.

Theory suggests that PAR$_{EM}$ does not need orthogonal adjustment. This needs to be tested. Other adjustments might be needed, but as noted earlier, the phase between the copolar and cross-polar fields is critical and needs to be considered in any design and should to be measured along with the power patterns

3.2.1.2 *Adjustment on reception*

Even if the moments of the two dipoles operating in the ALT mode are not adjusted on transmission to obtain alternating H and V polarizations, it is still possible to obtain all the polarimetric variables (Zrnic et al. 2011, III B). Pulse-to-pulse adjustment on reception is not practical because of the unknown Doppler shift and decorrelation between successive returns. Thus to determine the Doppler shift one needs an estimate of the autocorrelation function. Therefore, it has been suggested to compute the polarimetric variables from estimates of powers, correlations, and Doppler shift. The ensuing set of equations, for a non-diagonal scattering matrix, is lengthy, but can be solved. It requires knowledge of the amplitudes of the dipole moments and the differential phase on transmission as well as on reception. Moreover the effects of propagation on the procedure remain to be quantified. This type of adjustment has never been done in practice. Significant simplification of the procedure ensues if the backscattering matrix and the propagation matrix are diagonal. Then even a simple multiplicative correction of the returns enables the radar to obtain polarimetric variables with acceptable bias over a large field of view (Fig. 2 in Zrnić et al. 2011).

Subject study
Experimental test of the procedures starting with the simplest one should be made.

3.2.2. SIM mode

In the SIM mode only reflectivity, differential reflectivity, differential phase and correlation coefficient magnitude can be estimated. This mode is thus effective in probing precipitation that has negligible depolarization along the propagation path, and whereby the backscattering matrix **S** is diagonal. Moreover in this mode the Doppler effects are not coupled to the polarimetric variables, and this is an advantage discussed in section 3.3.

Corrections *on transmission and reception,* or only *on reception,* can be applied. In either case *pulse-to-pulse* adjustment at the receiver or *solutions from estimates of powers and covariances* are feasible. The later one is preferred because of computing efficiency and proven robustness of results (similar to what is used on the WSR-88D).

The proposed corrections require measurement of differential phases on transmission and on reception as well as calibration of transmitted field amplitudes similar as on radars with parabolic dish antennas.

Subject study

PAR$_{EE}$: The SIM mode can be used without adjustments or corrections in the principal planes where it is essentially the same as SHV mode on the WSR-88D. A study that extends the preliminary work of Zrnić et al. (2011) should be done to establish how far out of these planes can the SIM mode be used before unacceptable bias without correction is incurred, and which variables would be compromised most. The effects of diagonal (coupling) terms in backscattering and propagation as function of pointing direction need to be quantified. Also the following quote from Zrnić et al. (2011) applies: "A comprehensive approach left for future study is optimum solution for the covariance terms and Doppler spectral moments using all available information, i.e., the time series data. The maximum likelihood method is the obvious candidate, but the complexity and computational burden might be more than current technology could support at an affordable price."

PAR$_{EM}$: The SHV mode might be applicable to this design. But this will depend on the intensity of secondary cross-polar fields (Sections 2.3 and 2.4).

3.3 Transmitted sequences – for SIM and ALT modes

Contrasts in processing of the weather signals for SIM and ALT modes to obtain polarimetric variables are highlighted here. Reference to the proven operational SHV on the WSR-88D mode is made repeatedly. In Appendix A1, contrasted are fields of polarimetric variables obtained from the same data in the two modes.

3.3.1 Scans at low elevation angle

Observation at the few lowest elevations is most demanding as the ambiguities in range and ground clutter are the most severe. On the WSR-88D a surveillance scan (with a long PRT) and a Doppler scan (short PRT) are used at the few elevations to deal with range velocity ambiguities. These are discussed next

3.3.1.1 Long PRT

Polarimetric measurements on the WSR-88D at the two lowest elevations are made in the long PRT surveillance scan. That way no range ambiguities are encountered. These measurements in the SHV mode have a definite advantage over the AHV mode. If the H and V polarized fields are spaced by the long PRT = T_l, AHV measurements of Z_{DR}, ρ_{hv} and Φ_{DP} are compromised. That is, the errors in all three estimates would be larger for data collected using the AHV than those data collected using the SHV mode. The errors are also larger than what would be obtained by using short PRTs because the normalized spectrum width,

$$\sigma_{vn} = \sigma_v/2v_a = 2T_l\sigma_v/\lambda \qquad (3.4)$$

is large hence it causes increase in errors (Doviak and Zrnic 2006, section 6.8). The variable which degrades significantly is the ρ_{hv} estimate because it needs the correlation at lag 2 as the following formula spells

$$\left|\hat{\rho}_{hv}\right| = \left|\hat{\rho}_{hv}(T_l)\right| / \left|\hat{\rho}_{hv}(2T_l)\right|^{0.25} . \qquad (3.5)$$

The standard deviations of polarimetric variables are computed in the Appendix A2 and plotted as well. To illustrate, the SD(Z_{DR}) is reproduced in Fig. 3.2. The pulse repetition frequencies are those used on the WSR-88D. The lowest one (320 Hz) is standard for the surveillance scans at 0.5 and 1.5 deg elevations and is the Long PRT. The polarimetric variables are computed only in the surveillance scan hence the corresponding fields are free of range ambiguities (and overlaid echoes).

      The difference in performance of the SHV and AHV modes is striking; at σ_v of about 2 m s^{-1} the estimate in the AHV mode (320 Hz) breaks down. This is not acceptable as median spectrum width in squall line cores is 5.4 m s^{-1}, and the SD(Z_{DR}) should be below 0.4 m/s at spectrum widths of 4 m/s. Clearly a straight forward AHV is out of the question and alternate ways to measure unambiguously the polarimetric variables need to be explored.

Subject study

      Explore quasi orthogonal codes to see if these would provide sufficient isolation so that a SIM mode would not generate excessive biases and variances in the polarimetric variables. The correlation of the pre envelop of the codes should be very small while
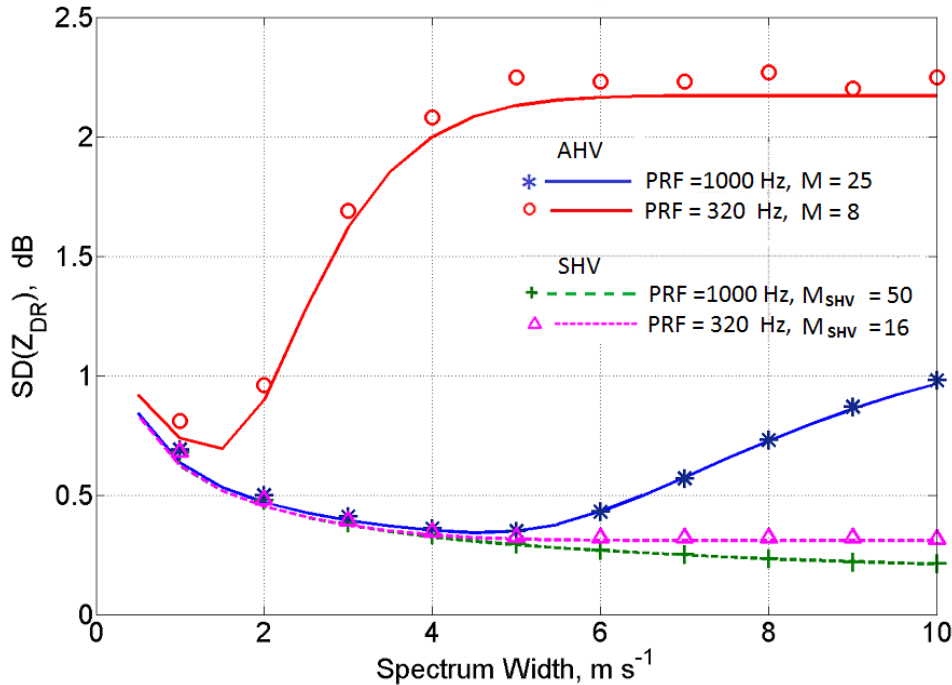

Fig. 3.2 Standard deviation of differential reflectivity as a function of spectrum width for AHV (solid lines) and SHV (dash lines) modes for equal dwell times, SNR > 20 dB and ρ_{hv}=0.98. M_{SHV} is the number of pulses transmitted in the SHV mode, and M is the

number of pulse of like polarization (H of V) it is one halve of the M_{SHV}. The symbols represent simulation results.

the autocorrelation should have a well defined peak. See section 4 for further discussion. There could be combinations of SIM and ALT modes such that the errors of estimates are in check while the resolution of range ambiguities is equivalent to the ones on the WSR-88D.

3.3.1.2 Short PRT – Coupling between Doppler velocity and Φ_{DP}

In the AHV mode operating with uniform PRT, coupling of differential phase shift Φ_{DP} with Doppler phase shift $\omega_d T_s$ needs to be dealt with (Doviak and Zrnic 2006, Section 6.8; or Zahrai and Zrnic 1993). The two phase shifts are in the arguments of the following autocorrelation estimates

$$R_a(T_s) = \frac{1}{M} \sum_{i=1}^{M} H^*(2i)V(2i+1) \tag{3.6a}$$

and

$$R_b(T_s) = \frac{1}{M} \sum_{i=1}^{M} V^*(2i+1)H(2i+2). \tag{3.6b}$$

where M is the number of HV or VH pairs, and the arguments indicate the sample position in time. Thus

$$\arg[R_a(T_s)] = \omega_d T_s + \Phi_{DP}, \tag{3.7a}$$

and

$$\arg[R_b(T_s)] = \omega_d T_s - \Phi_{DP}. \tag{3.7b}$$

Combining these two equation yields

$$\Phi_{DP} = \arg[R_a(T_s)R_b^*(T_s)]/2, \ \ \text{or} \ \ \Phi_{DP} = \arg[R_a(T_s)R_b^*(T_s)]/2 + \pi. \tag{3.8}$$

The ambiguity of π can be resolved with help of continuity in range because the initial phase of the system can be measured and in most precipitation Φ_{DP} increases with range. (An example of the effect on data obtained by the polarimetric WSR-88D is in the Appendix A1). Substitution of the dealiased Φ_{DP} in (3.7a) and (3.7b) and following the rule in Zahrai and Zrnic (1993, Eqs. 14a-h) the Doppler velocity is decoupled from Φ_{DP} and obtained over its unambiguous interval determined by T_s.

The Doppler spectrum width σ_v is estimated from the lag 2 and lag 0 autocorrelations Zahrai and Zrnic (1993)

$$\hat{\sigma}_v = \frac{\lambda[-0.5 \ln \hat{\rho}(2T_s)]^{1/2}}{4\pi T_s} \tag{3.9}$$

where

$$\hat{\rho}(2T_s) = \frac{R_a(T_s) + R_b(T_s)}{(S_h + S_v)}; \quad S_h = \frac{1}{M}\sum_{i=1}^{M}|H(2i)|^2; \quad S_v = \frac{1}{M}\sum_{i=1}^{M}|V(2i+1)|^2.$$

Note that at the same spectrum width the errors of estimator (3.9) are larger than the errors of estimator obtained from $\rho(T_s)$ (see Doviak and Zrnic 2006, Fig. 6.7).

3.3.1.3 Short PRT – error in estimates

Standard deviations of the differential reflectivity estimates obtain using either the SHV and AHV modes of data collection are plotted in Appendix A2. The results are also in Fig. 3.2 where the short PRT corresponds to the PRF of 1000 Hz which is very often used in the Doppler scan.

SD(Z_{DR}) for AHV mode is marginally larger at low spectrum width because of the high correlations although the number of samples is one-half of that used in SHV mode. Larger separation of samples in the AHV mode compared to the separation in the SHV mode comes to play at big spectrum widths. Then the AHV samples are less correlated which noticeably increases the errors (in the AHV mode). The main difference between SD(Z_{DR}) in SHV and AHV modes is that SD decreases monotonically with spectrum width for SHV mode. Currently the polarimetric variables are not computed in the Doppler scan of the WSR-88D but that will change.

3.3.2 Phase coding

In the AHV mode special phase coding (Zrnić 2007) similar to SZ-2, Torres et al. 2007 that is operational on the WSR-88D could be applied separately to each channel. As an example for discussion consider the first four trips in the SHV mode (PRT=T_s); these first four trips are resolve with the SZ-2 code. Then in the AHV mode separation of overlaid echoes of the same polarization would only be needed for the third and first trip (i.e., H overlaid to H). The unambiguous (Nyquist) velocity interval within which the spectra of the H (or V) signals are located is reduced by a factor of two compared to the Nyquist interval in the SHV mode.

To design a phase code (for say H channel) one needs to specify the number of trips L over which the protection (recovery) of overlaid echoes is needed. The other essential parameters are the code length $M = mL$ and the code periodicity p (defined as length of smallest subsequence in M that repeats). It follows that if L is divisible by 4 the period $p=L/4$ otherwise the period $p=L$. The periodicity indicates how many spectral replicas will be present in the modulation code. There is a compromise in separating the replicas (signals to be reconstructed) from the cohered signal that needs to be filtered. Two replicas are needed for reconstruction, and if there are many replicas (i.e., p is large) most of the undesirable signal will be filtered; but then only signals with very narrow spectrum widths would be faithfully reconstructed.

In its favor the AHV mode has the fact that the second (and other even number) trip echoes are orthogonal to the first trip hence would cause less harm to the desired first trip. In case of phase coding it might be possible to further reduce the overlaid V to H (and H to V) echo by choosing "orthogonal" phase sequences. This requires further investigation.

3.3.3 Staggered PRT

Staggered PRT is challenging for the AHV mode because of coupling between $\omega_d T_s$ and Φ_{DP} and the concomitant ambiguity in Φ_{DP}. This we illustrate by way of example. Let the stagger ratio $T_1/T_2 = 2/3$, $R(T_1)$ and $R(T_2)$ be the autocovariances at the corresponding lags, and $T_1=2T_u$ and $T_1=3T_u$. Then similar to (3.7) we write

$$\arg[R(T_1)] = 2\omega_d T_u + \Phi_{DP}, \qquad (3.10a)$$

and

$$\arg[R(T_2)] = 3\omega_d T_u - \Phi_{DP}. \qquad (3.10b)$$

Implicit in this pair of equations is the assumption that the first echo sample has H polarization. Combining (3.10a) with (3.10b) to eliminate Φ_{DP} defeats the purpose of the staggered technique as it would reduce the unambiguous velocity interval by a factor of 5 compared to what the staggered PRT would yield. Therefore, we need to eliminate $\omega_d T_u$ from this pair of equations. This seemingly trivial chore is fraught with obstacles. Division by 2 and 3 of these equations is needed to eliminate $\omega_d T_u$. This division amounts to taking roots on the unit circles (two in 3.10a and three in 3.10b) resulting in five possible solutions (ambiguities) of Φ_{DP}. These ambiguities are spaced at $2\pi/5$ intervals which might be too small to resolve by applying range continuity.

Relatively simple modification can be made at modest expense of increased dwell time (see Fig. 3.3) to resolve this problem. The velocities would be determined independently from the pair HH (at T_1) spacing and VV (at T_2) spacing; thus the Doppler phase is completely decoupled from the differential phase.
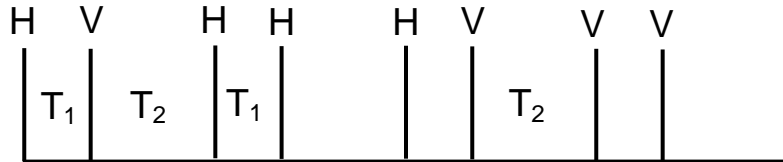

Fig. 3.3 A sequence for decoupling differential phase from Doppler velocity measurement.

Shorter sequences such as in Fig. 3.4 combined with pulse compression could work well. The four pulses represented with full vertical lines form the smallest group per beam position from which the polarimetric variables can be obtained. The Doppler phase estimated from the H pair is not coupled to differential phase and corresponds to T_2. The Doppler phase corresponding to T_1 is eliminated from the correlations of the pair HV and VH yielding unambiguous Φ_{DP} over a 180° interval (3.8). Continuity in range can be applied to unwrap the Φ_{DP} over a 360° as discussed in section 3.3.1b). Because correlations and powers are estimated from very few samples pulse compression would be needed to improve precision.
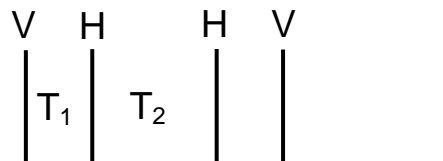
Fig. 3.4 Possible transmitted group for one beam position. The absolute minimum necessity is depicted by full pulses. The dotted pulse provides advantages for measurement of Φ_{DP} and Z_{DR}.

Decision on what kind of time sequence to design depends on the specified accuracy of estimates. Note that time between consecutive groups associated with two beam positions does not have to be sufficiently large to accommodate echoes from beyond $cT_1/2$; beam agility can suppress these returns. That is, the subsequent beam position can be chosen such that a region of very low value in antenna pattern coincides with the beam center at the previous beam position.

3.3.4 Clutter filtering in the context of R/V mitigation

This is relatively a smaller issue compared to the daunting task of clutter filtering of short time series. If the later can be done well on short uniformly spaced pulse trains, then the ALT mode (with same pulse spacing) would take about twice as much time to achieve clutter suppression in both H and V echoes.   Another disadvantage is that the Nyquist interval in the ALT mode is reduced to one half of what it is in the SIM mode. Hence, weather echoes with commonly encountered velocities (twentyish m s^{-1}) which fall in the aliased notch would be filtered. This can be mitigated by sophisticated clutter recognition techniques (CLEAN-AP, CMD, etc.) but not completely eliminated.

4. Design of radar signals and processing

One of the objectives of the MPAR is to decrease the volume surveillance time. One of the approaches to decrease surveillance times is to decrease the time to estimate weather parameters. The purpose of this section is to illustrate the challenges that rapid estimation of spectral moments and polarimetric variables present. This we do by examining the reduction of statistical errors in reflectivity obtained from a one suitably designed transmitted pulse. Uniform trains of pulses are typically transmitted by weather radars because of the need to resolve and edit artifacts such as ground clutter, point target clutter, etc. These artifacts are more easily detected and edited if spectral analysis is performed on a uniform train of echo samples. However, at high elevation angles, and in regions of precipitation, artifacts rarely present a problem, and a suitably designed single transmitted pulse might meet the NEXRAD Technical Requirements of sensitivity, accuracy, and resolution while decreasing the volume scan time.

Thus examined are two techniques that are applied to transmitted pulses and some variants in processing of echo samples to obtain adequate number of independent samples from a single transmitted pulse. The two techniques are pulse compression and multiple frequency transmission. Hard constraints such as power and bandwidth and a softer constraint like pulse duration are brought to the reader's attention. No resolution of these is attempted but tradeoffs and implications are discussed and directions for research to overcome these are presented.

In traditional tracking radars, pulse compression is used to increase SNR from targets and to increase range resolution. For weather radar there is additional motivation for its use; that is to reduce errors in estimates by averaging in range the polarimetric variables obtained from compressed pulses. In any case, requirements of range resolution, accuracy of reflectivity estimates, and sensitivity to detect weak reflectivity, as specified for the WSR-88D in the NTR documents are not to be compromised.

Smith (1986) noted that signal processing of echoes from several pulses is required to extract reflectivity data. Smith's approach to determine weather radar sensitivity is based on probability the echo sample of signal plus noise at the receiver output port exceeds a threshold. This approach is backed by extensive literature (e.g., DiFranco and Rubin 1980) on the detection of point targets such as aircraft, missiles, etc, in which detection probabilities and false alarm rates are the principle measures of radar performance.

To compare the equivalent signal-to-noise ratios that would yield a specified false alarm rate and probability of detection Smith defined a signal processing factor f(SP) and an expression dependent on weather radar parameters. The f(SP) is a factor inserted into the weather radar equation (e.g., Eq. 4.35 in Doviak and Zrnic 1993) for calculating the expected weather signal sample power. The principal advantage of Smith's approach is it permits a more general assessment of radar sensitivity without explicitly including the more complex and diverse methods of processing weather signal samples to estimate Doppler spectral moments (e.g., mean power or reflectivity factor).

On the other hand, of prime interest to radar meteorologists is the accuracy of the estimates of Doppler spectral moments and, more recently, polarimetric variables. Thus we extend the assessment of weather radar detection capability to include accuracy but omit many complexities of signal processing. Toward this goal we consider a common

simple incoherent averaging of power measurements to derive the meteorologically important reflectivity factor Z.

4.1 Power, range resolution, and bandwidth

Transmitted power, bandwidth, and dwell time have fundamental influence on the accuracy of estimates. We anticipate that the total transmit power delivered to the antenna will at least equal or exceed 450 kW, the power delivered to the antenna on the WSR-88D.

Assume for illustration the following flat panel PAR: an elliptical cross section with a height of 8.4 m (same as diameter of antenna on the WSR-88D), a width of 12.1 m (to obtain a 1° resolution at an electronically steered beam 45° from broadside), and element spacing is 0.75 λ. With a PAR antenna vertically tilted by 10°, the beamwidths will be close to 1° in the azimuth domain $\pm45^o$ and $0 \rightarrow 20^o$ in elevation angles. The number of H, V elements per face is 14605 (Zhang et al., 2011) and each should radiate 31 W to match or better the WSR-88D detection sensitivity at all pointing angles; this \power level assumes the aperture is uniformly illuminated. However, in this case the transmit sidelobes of the antenna's radiation pattern will be higher than they are for the WSR-88D. To achieve the same sidelobe performance on transmit, the power radiated across the aperture needs to be tapered. In that case the central elements will need to radiate about 75 watts of peak power, whereas the elements at the edges of the array will radiate significantly less power.

Recently made solid state amplifiers in the 2.7 to 3 GHz frequency range have achieved output power of about 100 W. In Fig. 1 are the characteristic of an amplifier build by Cree Co; similar amplifiers are also available from RFHIC Co. model RRP 29080-10 (80 W, and duty cycle 20 %). With such amplifiers pulse compression for gaining effective peak power and resolution is not required although the full potential of this amplifier without pulse compression would not be achieved (the amplifier has a 20% duty cycle). *But, pulse compression can be used to increase the number of independent samples in range and then average the estimates from these densely spaced resolution volumes to obtain low error of estimates.* Because the technique's potency increases with use of larger bandwidth a brief discourse on the bandwidth follows.

Transmitter bandwidth specs for the WSR-88D are: at -40 dBc (i.e., 40 dB below the carrier level) the maximum bandwidth must be less than 14.5 MHz and at -80 dBc level the maximum bandwidth must be less than 145 MHz without a spectrum filter (ROC, 2006). At locations with multiple radiators transmitting in the 10-cm band, a spectrum filter is required such that the bandwidth at $-$ 80 dBc is less than 46 MHz.

The specified pulse lengths on the WSR-88D are 1.57 μs (referred to as short) and 4.71 μs (long) and these are processed with a matched filter (Table 4.1).

For the more stringent criterion (i.e., 46 MHz at $-$ 80 dBc) the transmitted signal bandwidth (i.e., measured across the -6 dB points) is 600 kHz (the reciprocal of pulse width; Doviak and Zrnic, 2006, section 3.5.3) for short pulse transmissions. This small bandwidth would hamper use of sophisticated pulse coding techniques. The less stringent bandwidth requirement of 72.6 MHz should easily accommodate a three times larger bandwidth (ratio 72.6/22.9). In that case bandwidth 3 to 4 times larger than $1/\tau$ (1.8 to 2.4 MHz) would be sufficient for gain in performance via pulse compression or

71

coding. It can be shown that if the transmitted pulse has Gaussian shape and is as short as 0.3 µs the transmitted bandwidth would be about 2.5 MHz at the -80 dB level and thus within specified bounds of 23 MHz at that level; hence pulse compression technique could be used to obtain about 5.6 independent samples.

Table 4.1 Pulse lengths and matched filter (SIGMET) characteristics.

	Short Pulse	**Long Pulse**
Pulse length, τ	1.57 µs	4.71 µs
FIR Bandwidth, B:	605 kHz	200 kHz
FIR length:	2.15 usec	6.53usec
DC Offset:	0	0
Nominal Filter loss:	0.8dB	0.6 dB
Number of FIR taps:	155	470

Fig. 4.1. Output power, gain, and efficiency of a solid state amplifier versus frequency.

Currently the WSR-88D radars abide by criteria in group D of the RSEC (Appendix B) within the subgroup for non-FM, non-spread spectrum and non-coded pulse radars. Other pertinent group D subgroups are for the FM, FM with frequency hopping, and frequency hopping using non-FM pulses (including spread spectrum coded pulses). These subgroups allow sufficient bandwidth for effective use of respective techniques. It is uncertain if the MPAR would be classified within any of the subgroups

and thus granted the associated bandwidth. Although this is of great concern our approach is to point out the possible technical solutions, indicate the required bandwidth and further research to reduce it.

To determine the shortest dwell examine the variance reduction that can be obtained by processing a return from a single pulse unconstrained by the NTIA regulations presently placed on the WSR-88D. Here the single pulse means a transmitted burst which might contain various modulations, frequencies, or combination of these, etc.

The required accuracy of reflectivity estimates (including only the error due to meteorological signal fluctuations) at SNR $\geq$ 10 dB is 1 dB (NTR, 1991). To achieve it the number of independent samples M_I must satisfy (Doviak and Zrnic 2006; supplement for errata eq. 6.13c).

$$M_I \geq [4.34(1+N/S)]^2 = 22.8, \qquad\qquad (4.1)$$

where N and S are noise and signal powers.

Averaging four samples in range reduces the errors so that the number of independent samples needed is 5.7. Further reduction in error is accomplished by averaging in sample time. Thus to meet the current requirements on a single pulse with averaging in range up to 1 km, 5.7 equivalent independent samples are needed.

Let's examine the current practice on the WSR-88D and future enhancements so that a realistic desirable error in estimates from a single pulse can be determined. On those radars 15 transmitted pulses is the smallest number routinely available in surveillance scans (i.e., using a long PRT). The samples are partially correlated and to quantify the effect of this correlation let the Doppler spectrum have Gaussian shape (Doviak and Zrnic 2006, eq. 6.3) and assume large SNR. The standard error of reflectivity estimate is plotted in Fig. 4.2 (eq. 6.12 from Doviak and Zrnic 2006).
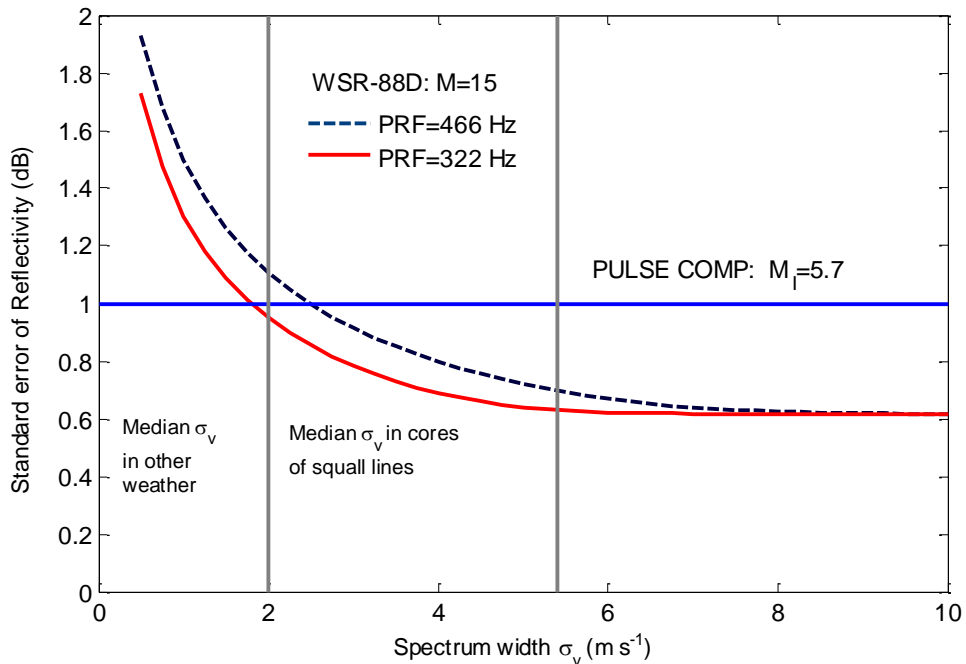
Fig. 4.2. Standard error of reflectivity estimates obtained from M=15 pulses transmitted at the two lowest PRFs (of the WSR-88D) as function of spectrum width. The median spectrum widths for weather returns are indicated. The straight blue line indicating error of 1 dB is obtained using 5.7 independent samples.

The spectrum width observed in isolated severe storms, fair weather without birds, widespread showers, broken squall lines in early stages, and stratiform rain and snow have median values less than 2 m/s (Fig. 4.2); larger σ_v with medians up to 5.4 m/s is found in squall lines embedded within stratiform precipitation (Fig. 4.2); clusters of severe storms and storms along broken squall lines have median widths between these two types of weather events. The statistics of spectrum width is related to storm type in the paper by Fang et al., (2004).

As can be seen from Fig. 4.2 the spectrum width has a strong influence on the errors in reflectivity estimates. For all but one of the storm types analyzed the median spectrum widths were below 4 m/s. Most of the weather types harbor spectrum widths smaller than 2 m/s, but recorded median spectrum widths in squall lines and severe storms were between 2 and 5.4 m/s.

From Fig. 4.2 we conclude that if the single MPAR pulse can yield 5.7 independent samples the errors would be lower than on the WSR-88D if the spectrum width is smaller than about 2 m/s. Otherwise the errors from MPAR would be inferior to the ones on the WSR-88D, but would satisfy specifications. Independence of error on spectrum width is an advantage for numerical models as these require estimate of the errors.

Clearly meeting the written NTR requirements for reflectivity on the MPAR can be done with 5.7 independent samples followed by averaging four samples in range. In the future the NWS will introduce pseudo whitening (Torres et al. 2004) on the WSR-88D thus creating a four fold increase in the number of independent samples. If this happens larger compression ratios would have to be used on the MPAR to match the capability of the future WSR-88D.

Next we plot the standard error in velocity estimates (Fig. 4.3) obtained from M=50 contiguous pulses (i.e., 49 pairs Eq. 6.21 in Doviak and Zrnic 2006) and 25 independent pairs (Eq. 6.22b, Doviak and Zrnic 2006). The parameters listed in the caption are one of the possible Doppler scans. The NEXRAD requirements specify an error less than 1 m s^{-1} at SNR=10 dB and $\sigma_v = 4$ m s^{-1}. It is evident that this particular choice of parameters misses the requirement. This is not unusual as in few modes the requirements are a bit relaxed in order to preserve resolution in azimuth and speed of volume coverage. The point from Fig. 4.3 is that 25 independent samples pairs can do as well or better than 49 contiguous samples.
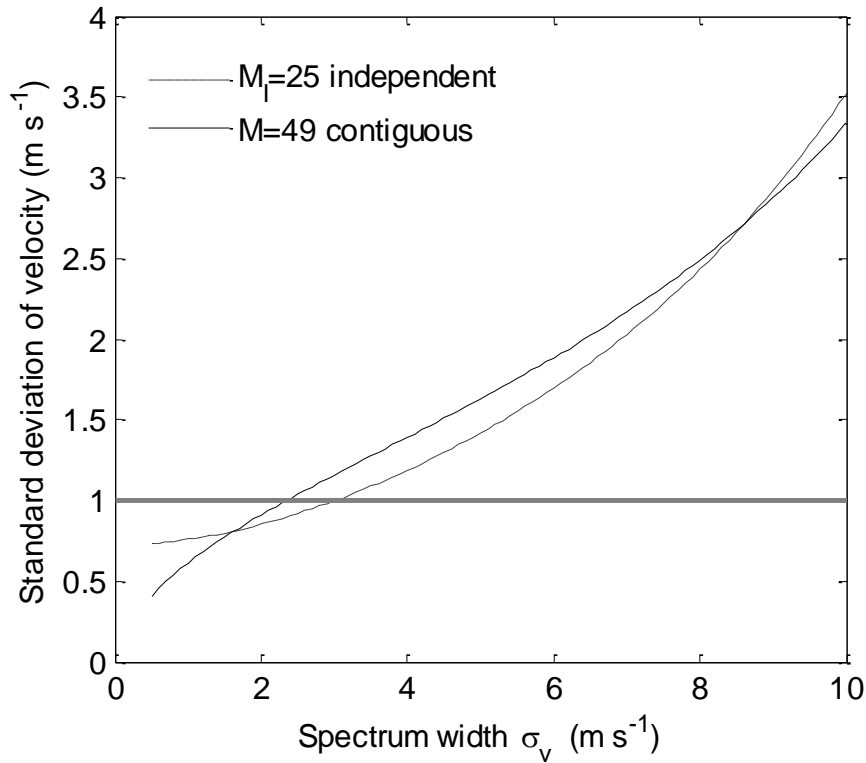
 Fig. 4.3 Standard deviation of Doppler velocity estimates obtained from 25 independent pairs and 49 contiguous pairs. The pulse repetition frequency is 1280 Hz (typical WSR-88D), the wavelength is 11 cm, and SNR=10 dB.

To demonstrate how we can incorporate independent reflectivity and velocity samples into a data collection sequence, we present a signal sequence applicable to polarimetric radar operating in the SIM (i.e., SIMultaneous excitation of the H and V ports of the antenna) mode (Fig. 4.4). In this sequence two pairs for Doppler velocity estimation are spaced far apart and in between a pulse for Z measurement is inserted. Because of such a large temporal separation the two pairs are, for most practical purposes, independent. Then pulse compression by about a factor of 12 would suffice to make for a total of 24 independent pairs. Clearly this sequence with low pulse compression ratio would produce acceptable errors in Z and Doppler estimates.
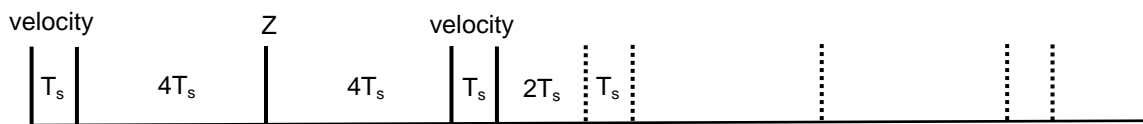
Fig. 4.4 A short sequence for Doppler measurement up to a range of cT_s and surveillance up to $2\,cT_s$.

The pairs for velocity measurement are indicated and so is the pulse for Z measurement.

The minimum dwell time corresponds to the solid pulses (including the clearing at the period of $2T_s$ at the end) in Fig. 4.4 and is $12T_s$. Note that the minimum time after the second pulse for Doppler measurement is $2T_s$ (indicated in the figure) and is required to cover the first and second trip. By beam multiplexing the $12T_s$ dwell time could be reduced to $10T_s$. In this particular example pulse compression of about 12 followed by range averaging would produce satisfactory errors of estimates.

In summary for Z estimates the pulse compression ratio should be about 6 and for velocity estimates about 12. Applying this to the sequence in Fig. 4.4 and averaging in range would produce estimates which satisfy the requirements.

Now we compare to time to cover one surveillance scan and one Doppler scan on the WSR-88D with the time to cover the same using pulse compression and sequence in Fig. 4.4. Assumed is 1° sample spacing in azimuth and the comparison is in Table 4.2. It takes the WSR-88D two scans (one for Z the other for velocity) to accomplish this coverage whereas a phased array radar or rapidly scanning radar with a mechanical dish can accomplish the same at a speed 10 times faster than on the WSD-88D. Although the phased array facilitates such quick scan by not having moving parts, or beam smearing, pulse compression and associated signal sequence are the fundamental reason making it possible. Thus we turn to the topic of pulse compression application.

Table 4.2 Time to obtain Reflectivity and Velocity estimates over one cone or the radar coverage.

Scan	WSR-88D time (s)	Sequence with pulse comp (s)
For Z	16	1.65
For v	14	1.4
Total	30	3.06

4.2 Pulse compression and matched filtering

Long pulses carry more energy than short pulses and thus can improve the signal to noise ratios at the expense of resolution. Pulse compression technique takes a long transmitted pulse and processes the received signal so that the range weighting function is many times shorter than the transmitted pulse. In traditional tracking radars very long pulses have been used for that purpose, and the same was applied to demonstrate measurements of reflectivity with phased array radar (Maese et al. 2001). Compression of 100 times is routine. Such large compression raises two issues which need to be dealt with. One is the extended region of range sidelobes; the other is the blind zone near the radar.

There are some compression schemes producing sidelobe levels of about -80 dB equaling far sidelobe levels on the WSR-88D antenna pattern. Although such schemes appear attractive, the large bandwidth occupied by the transmitted signal might be unacceptable for operational civilian applications. Even moderate pulse lengths (tens of µs) might be objectionable because the blind zone near the receiver would have to be dealt with, likely by transmitting a short low power pulse. This means that two pulses would be needed rather than one for reflectivity measurement and four instead of two for Doppler measurement. Therefore we will consider modest pulse length (<10 µs) such

76

that the blind zone (<3 km) is not an issue. The present resolution of the range weighting function ~ 235 m is a strong constraint which at the end of processing should be preserved.

In Appendix C comparison is made between performance of pulse compression and matched filter on uniformly distributed scatterers. The following expression relating the SNRs associated with the two techniques is derived:

$$\frac{SNR_m}{SNR_c} = \frac{P_m^t}{P_c^t} \frac{\tau_m^2}{\tau_l \tau_u} \ , \tag{4.2}$$

where SNR_m refers to the signal to noise ratio of the matched filter and SNR_c is for pulse compression. τ_m is the pulse length in the matched filter case, τ_l is the length of long coded pulse and τ_u that of its compressed form. If the transmitted powers are equal, but it is desired to keep the same detection capabilities (i.e., the same SNRs) the $\tau_l \tau_u$ must be equal to τ_m^2. So in case of the WSR-88D the τ_l could be about 2 to 4 times τ_m (~3 to 6 μs) and τ_u would than be ~ 0.37 to 0.75 μs. These are realistic possibilities, that is the long pulse is short enough not to present a problem for measurements at close range (dead range less than 1 km) and the compressed pulse is reasonably short so that the required transmission bandwidth is not excessive (less than 10 MHz).

4.3 Techniques for pulse compression

Some candidate techniques are mentioned in this section starting with the pulsed FM. The examples and discussions presented herein are notional, hence some important aspects are not quantified. For example, any of the pulse compression schemes should not be degraded by the Doppler shift (mean and spread) of the weather signal. That is Doppler tolerant schemes are needed so that the observations are the same as that obtained using non compressed pulses.

4.3.1 Pulsed FM
Linear and non linear FM modulations are candidates for pulse compression provided that the bandwidth is allowed. With a 5 MHz bandwidth (frequency excursion) a 5 μs pulse yields the time bandwidth product of 25. Powers from five to ten compressed pulses each about 200 ns wide can be averaged to produce that many independent samples. In principle this is a very attractive option requiring detailed evaluation.

Subject study
Design of the modulation frequency and the receiving filter so that the composite range weighting function at about 200 m from its center has a sharp drop. The desirable value is ~ 40 to 60 dB. From about 300 m and beyond the range sidelobes should be 70 to 80 dB.

4.3.2 Coded pulse techniques
The pulse in Fig. 4.5 helps illustrate some of the techniques. The total pulse length τ is divided in four and a symbol c_i refers to some kind of code within the length τ_u. In practice we are looking for small compression ratios so that the number of sub pulses

would be somewhere between 5 and 20. For the purpose of illustration we will use smaller numbers.
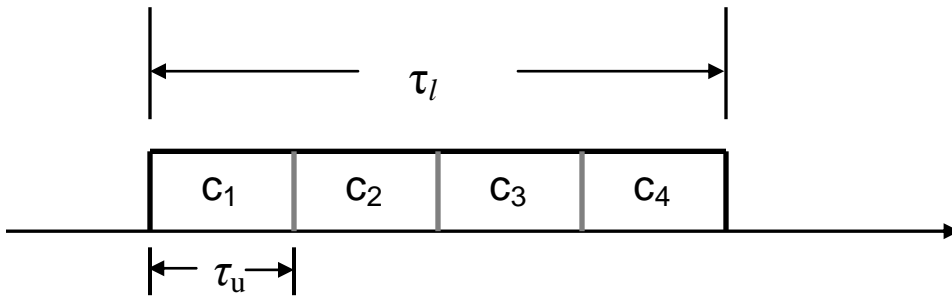

Fig. 4.5. Schematic representation of coded pulse.

Four sub pulses are convenient and easy to draw but real options would require appropriations of bandwidth. The sub pulse lengths can be equal (but need not be equal) to the present pulse length. The sub pulses have either different frequencies, specified phases, or could be sent in different directions to achieve space diversity.

It is important to design pulse compression such that the range sidelobes are well below the peak of the range weighting function. This is a challenge which might be somewhat relaxed if compression ratios are small, way less than 10. This is because the smearing in case of reflectivity gradients would not extent over large range. Nonetheless, Doppler shifts of weather signal can degrade performance of pulse compression, thus candidate schemes must have sufficient tolerance to it.

Simple techniques are examined to bring out the compromises suggesting research which might help resolve the issues. The techniques are transmission of multiple frequencies (MF), phase coding (PC), and space diversity combined with MF or PC.

4.3.3 Multiple frequencies

Four or more frequencies transmitted back to back each in a sub pulse of length equal to the current pulse (i.e., $\tau = 1.57$ μs) could be well suited for the PAR transmitting module. Thus the composite length of about 1 km would be short enough so that there would be no significant dead range after transmission, but yet allow the transmission of four independent pulses (i.e., practically no spectral overlap). Radars transmitting much longer pulses have a blind range which is usually eliminated by transmission of a short pulse. This increases the dwell time and is thus undesirable. Reception and parallel digital filtering can separate these four frequencies into four channels for further processing. Note that the pulse lengths for processing are each the same as on the current WSR-88D hence matched filter would keep the signal to noise ratio the same in each frequency channel. It follows that the scheme can provide four independent samples. This of course is a result of the fact that the average power has increased by a factor of four (another way of looking at it, there are four independent radars sharing a common antenna). For all practical purpose there is no limitation on the duty factor, hence in principle more frequencies could be transmitted. The issue is the increase in bandwidth or smaller separation between the frequencies.

Subject study

With MF the cross talk between the returns at different frequencies (and thus different ranges) needs to be small. A digital filter is needed which would allow closest separation in frequency a rejection of ~ 60 dB of the adjacent channel as shown in Fig. 4.6 Constraints are the maximum sampling rates (currently are ~ 100 MHz) and the effective filter length must match the desired range resolution. The MF scheme inherently is not affected by the Doppler shift of weather signals.
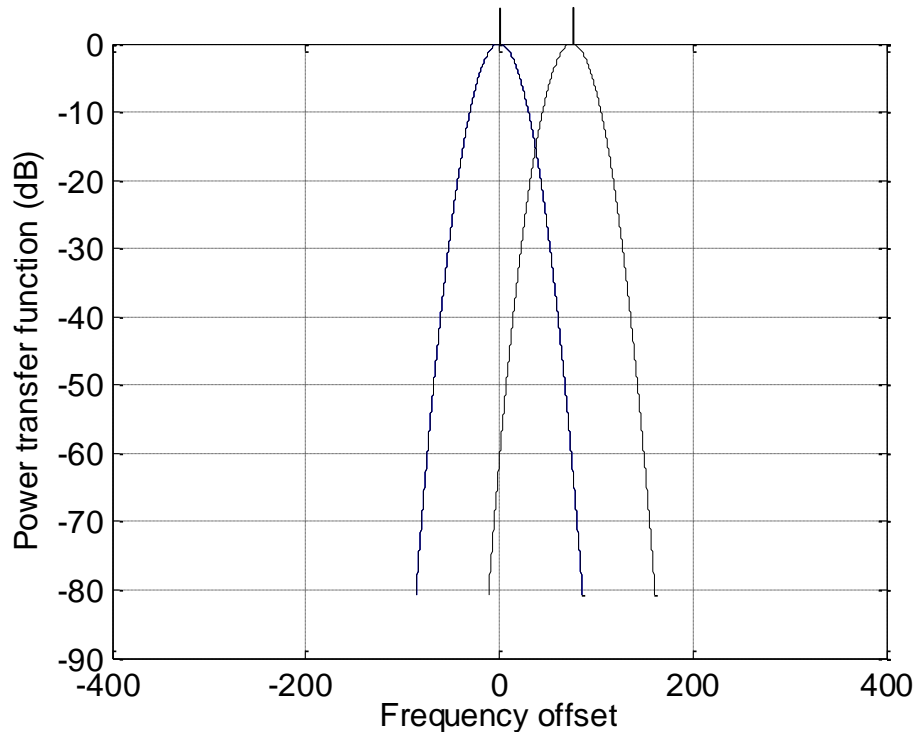

Fig. 4.6 Conceptual depiction of two filter characteristics. The objective is to design the filter with separation of carriers such that the attenuation of one at the center frequency of the other is at least 60 dB (as plotted here).

4.3.4 Phase coding

The simplest phase code is the binary [1, -1], where -1 refers to the phase reversal within the second half of the pulse. This code serves to illustrate the various aspects of range weighting and correlation of samples. Denote the voltage dependence on time of this coded pulse with $p(t)$. We will use this code and a pulse length of 1.6 μs (corresponding to 240 m) rather than 1.57 μs which corresponds to 235. The coded pulse voltage weighting function in range $W_c(r)$ equals to $p(-t)$, with $t = 2r/c$. The negative sign is due to the fact that the pulse rise in time corresponds to the leading edge and is thus furthest in range. This distinction is mute because the waveform will be symmetric, and curves in the plots will be centered on the pulse.

Thus the voltage range weighting function $W_c(r)$, prior to the matched filter is a pulse doublet (positive pulse followed by negative). The matched filter is a correlator hence the voltage weighting function becomes

$$W_{mc}(r) = cor[W_c(r), W_c(r)]. \qquad (4.3)$$

weighting function is the sum of the two
Its magnitude squared is the power range weighting function. If two power samples (magnitude squared) spaced by half the pulse length are averaged the effective range

$$|W(r)|^2 = |W_{mc}(r)|^2 + |W_{mc}(r+\Delta)|^2, \qquad (4.4)$$

where, $\Delta = c\tau/4$ (c=speed of light).

The correlation function of the signal at the output of the matched filter is given by the eq. (4.40) in Doviak and Zrnic (2006) with a slight modification of the term R_{xx}, namely this term equals eq. (4.3). The impulse response function h equals $p(t)$, hence to $W_c(r)$ and therefore the *signal correlation* becomes

$$R_s = cor[W_c(r), W_c(r)]. \qquad (4.5)$$

The *correlation between power samples* is thus the magnitude squared of (4.5) and the corresponding autocorrelation coefficient is denoted with ρ^2.

In Fig. 4.7 are plots of the weighting functions (4.3), (4.4) and the one for a rectangular transmitted pulse of the same length as on the WSR-88D (~ 235 m) after the matched filter.
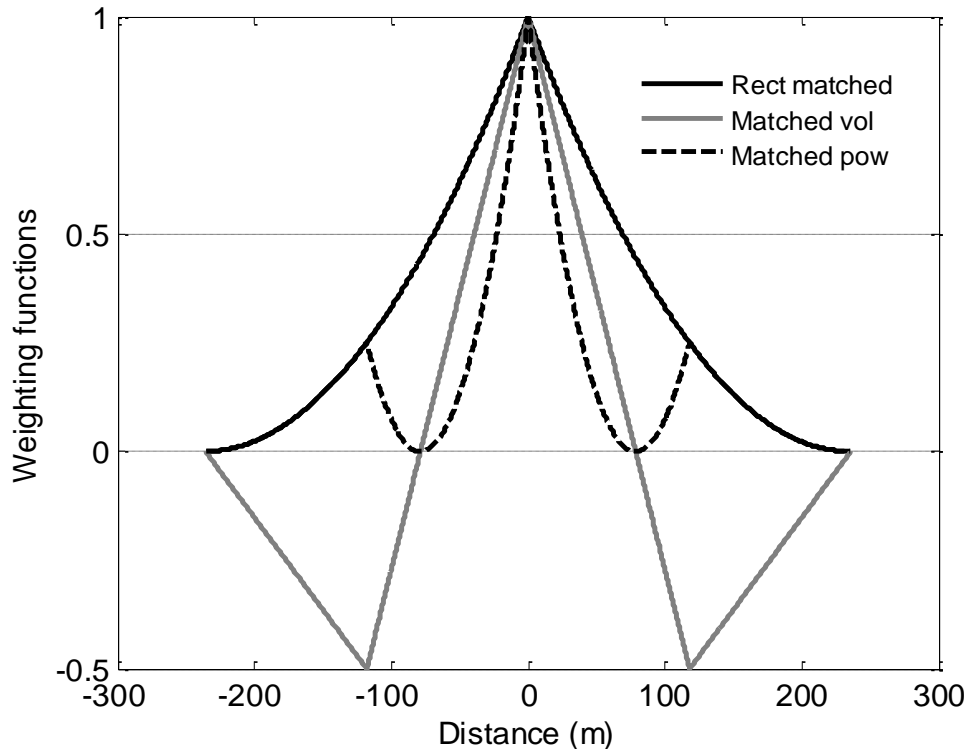
Fig. 4.7. The range weighting functions. Rect matched refers to the power weight at the output of ideal matched filter for the rectangular pulse (would correspond approximately to pulse length ~ 235 m on the WSR-88D). The Matched vol is $W_{mc}(r)$ and refers to the voltage weighting given to scatterers with this two phase pulse at the output of its matched filter. The Matched pow $|W_{mc}(r)|^2$ is the weight given to powers, analogous to the Rect matched.

Assuming that the powers are computed from the average power of two samples the power composite range weighting function (Fig. 4.8) is the sum of individual weighting functions displaced by the sample spacing (120 m) as in (4.4). Correlation coefficient, based on (4.5) is also plotted in Fig. 4.8. It is noteworthy that at the spacing of half the pulse width the correlation is almost zero hence two independent samples can be obtained. Smaller spacing of samples could further increase the number of independent samples. Optimum spacing allowing non uniform spacing might be possible. The composite range weighting function is symmetric with a minimum in the middle about ten times smaller then the maxima on the sides. The sharp peaks of the range weighting function are produced by the abrupt leading and trailing edges of the pulse and the instantaneous phase reversal in the middle of the pulse.
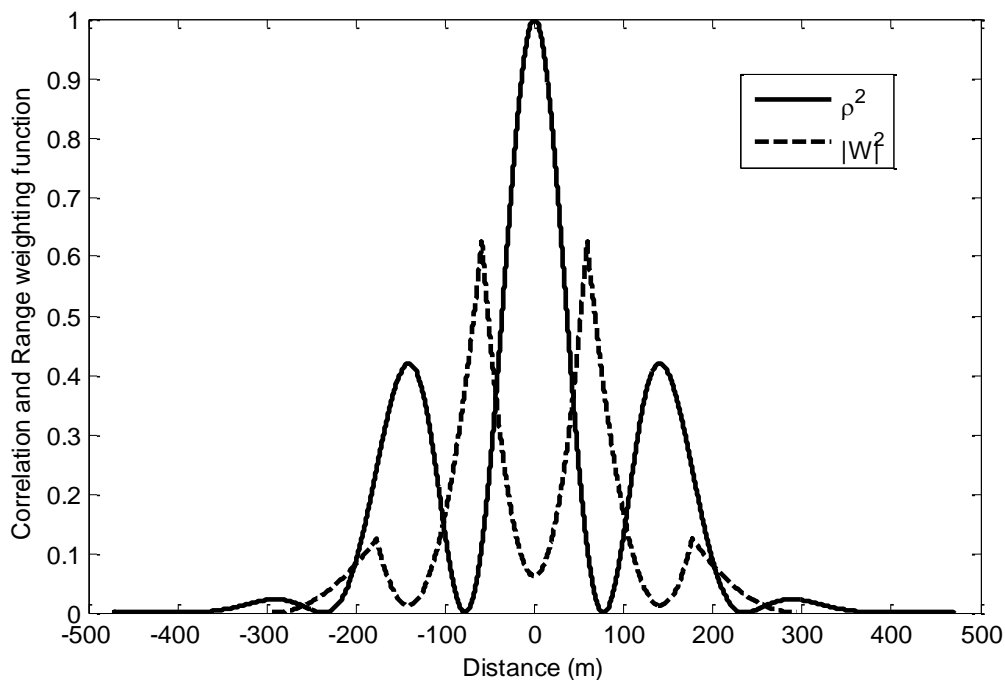

Fig. 4.8. Correlation coefficient ρ^2 of power samples in range time and the range weighting function $|W|^2$ of power estimate obtained by summing two samples spaced by half the pulse length.

4.3.5 Barker code of length 7
Barker codes of length 7, 11, 13 might be candidates for pulse compression if they could be desensitized from the effects of Doppler shifts (see Bucci et al. 1997, and

references therein). Here in we use these to illustrate the point and do not advocate direct application. As example we consider the code of length 7. The range weighting function of this code $|W_{mc}|^2$ after processing through its matched filter is compared to the range weighting function $|W_{mp}|^2$ of a non coded pulse processed by a matched filter, in Fig. 4.9. Clearly the shapes of the weighting functions are similar, the areas are about the same, and the resolution of the Barker code is about seven times finer. From (4.2) it follows that the sensitivity of the matched filter case is seven times higher than the coded case if $\tau_{l=\tau_m}$. To reduce variance of estimates one would choose $\tau_l > \tau_m$ and $\tau_u < \tau_m$, and then average various estimates in range. The various range weighting functions are plotted in Fig. 4.9. The composite range weighting function is a sum of displaced range weighting functions along the range time axis. It is assumed that powers from seven consecutive samples (along the range time axis) are summed to estimate the reflectivity. A smaller number of pulses can be averaged to increase the resolution at the expense of the number of independent samples. This is an added degree of freedom (to the constraint of eq 4.2) in the design of pulse compression schemes for weather radar. An optimum design compromise would have to include this and other factors.
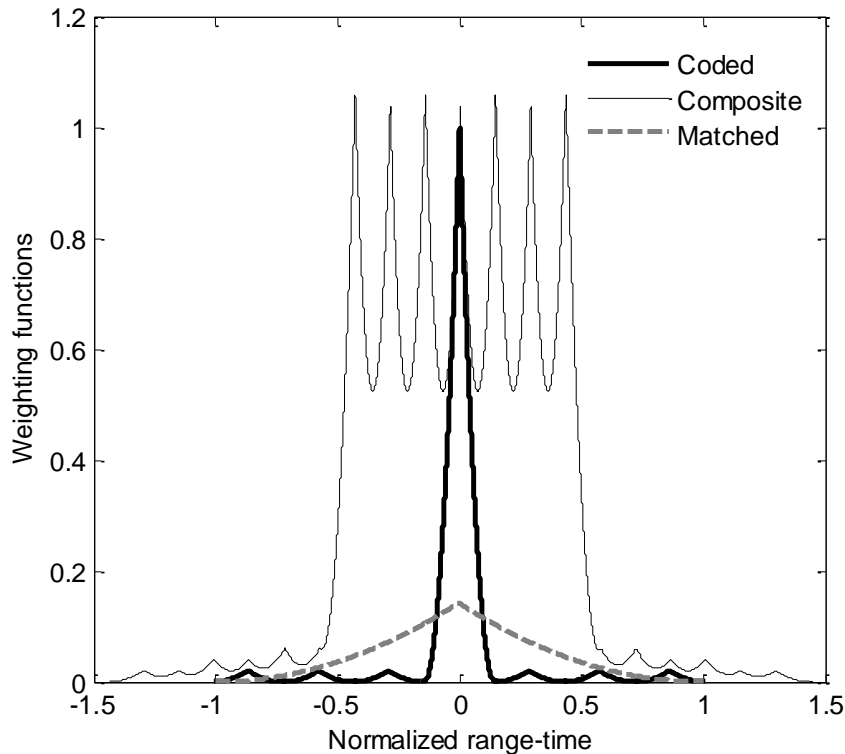

Fig. 4.9. Weighting functions of the matched filter, Barker 7 code and composite after summing 7 consecutive power samples in range spaced by τ_u.

If one starts with the same pulse width and same peak power as on the WSR-88D and compresses the pulse to gain independent samples the sensitivity would be reduced. Averaging of powers in range would not increase sensitivity although it would yield more independent samples and would reduce fluctuations of estimates. Furthermore, if range averaging is done over couple hundred meters the effects of range sidelobes would not be

an issue in rainfall measurements. This is because the accuracy is specified over a 1 km range interval. To avoid loss in sensitivity either the peak power needs a boost or the pulse should be longer than the current 1.57 us one. The second option is very realistic considering that recent transmit modules have sufficient power and large duty cycles.

Subject study

Specify the envelope of the composite range weighting function over the range-time length smaller then the code length. The composite is the sum of compressed pulse envelopes (power) over a range interval sufficient to provide independent samples. Give the main lobe width and the fall off of the range sidelobes. Assume oversampling and determine the coefficients of the compression filter such that the range weighting function is within the specified envelope. Phase codes might not handle well the Doppler shifts of weather signals; range sidelobes might be unacceptable and compression ratios would be reduces. These effects need to be quantified and mitigated.

The correlation coefficient of power samples obtained with this code (Fig. 4.8) indicates that samples spaced by the reciprocal of sub pulse length are essentially independent. For shorter Barked codes the correlation increases. Furthermore note that the correlation has oscillatory variation and for short codes sampling at the minimums would produce least dependent samples.
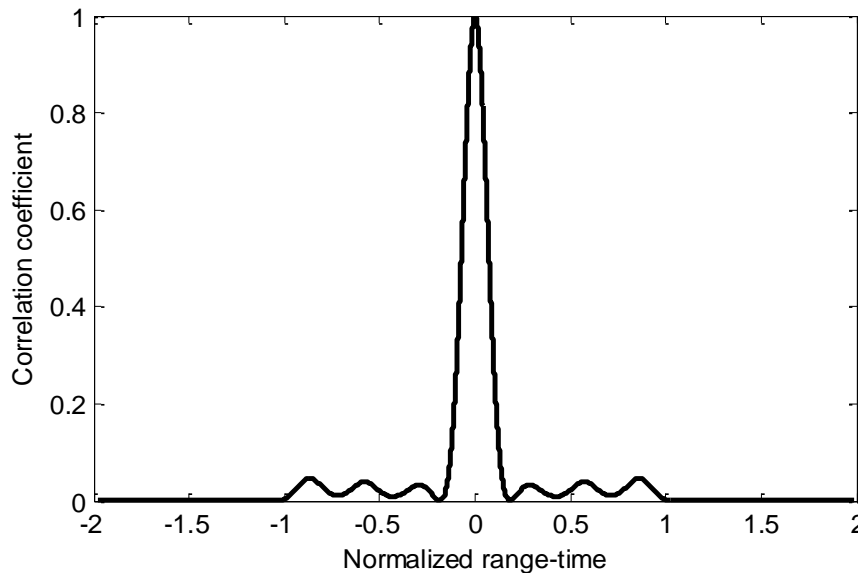

Fig. 4.10. Correlation coefficient of the Barker 7 code.

Subject study

The whole subject of low compression ratios for application to weather radar needs to be studies. This includes the composite range weighting function and the shape of the correlation coefficient. Ideally we want the composite range weighting function to be as compact and samples in range to be as independent as practical. These two requirements are conflicting and some optimum compromise should be found. Furthermore the effect of Doppler shift should be quantified.

Note: For shortest Barker codes the ratio of power in the mainlobe of W to power in sidelobes is smaller than n but for the longest it is closer to n. Other codes might offer possibilities. Of secondary importance is the practical pulse shape and it should be eventually accounted for.

Illustrative example: Let's look at eq. 4.2 having in mind the explanations put forward so far and apply for comparisons with the current WSR-88D (which has a pulse duration τ).

1) Take the peak powers of WSR-88D and PAR to be same. Then according to (4.2) the same sensitivity is achieved if $\tau_u = \tau/\tau_l$. To obtain 4 independent samples within τ the compressed pulse length τ_u must be bout 0.4 μs (1.57/4).

4.3.6 Orthogonal codes

By definition the correlation function of orthogonal signals is zero. In radar applications it is the complex pre-envelope that constitutes the signal and two such signals can be made orthogonal if they occupy separate frequency bands. Otherwise the cross correlation of the two signals will have finite values over the interval equal to twice the long pulse length. Denote the two pre-envelopes p and q then the goal is to have the autocorrelations: $cor(p^*, p) = cor(q^*, q)$ within the compressed pulse while the cross correlation $cor(p^*, q)$ is as small as possible outside of the compressed pulse width.
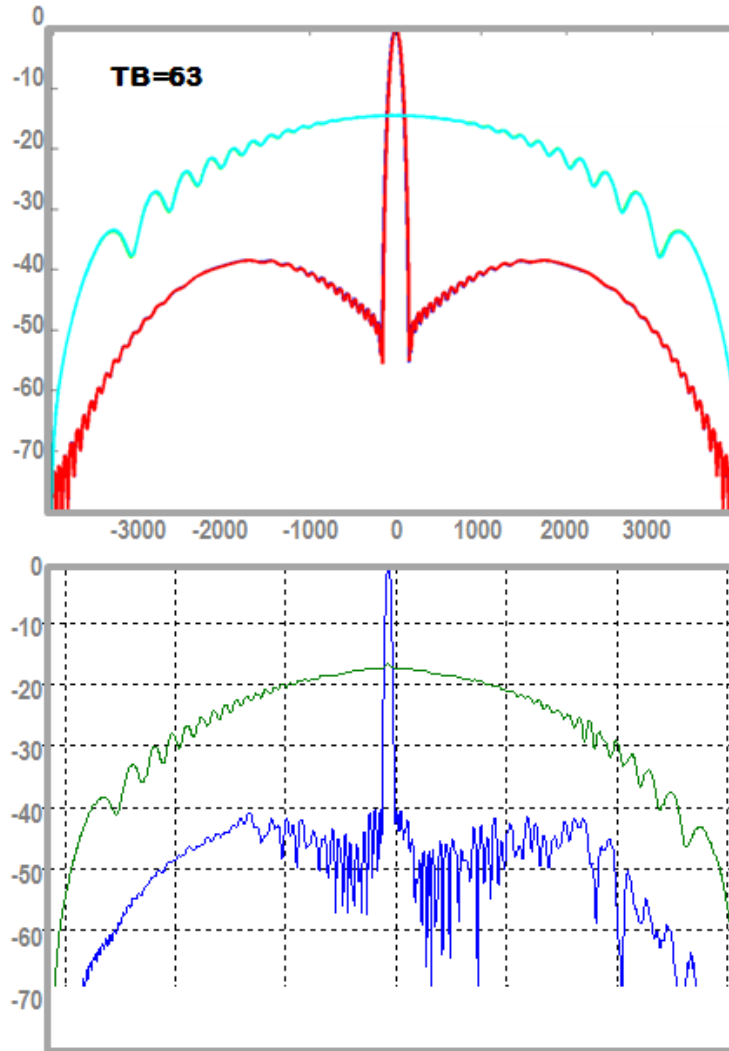
Fig. 4.11 Top: Cross-correlation of an up- and down-chirp linear FM signal (cyan) and autocorrelation of either signal (red). Pulse width is 63 μs, bandwidth is 1 MHz, and the results are from computations. Bottom: Same as on top but the results were obtained from measurements. The ordinate is in dB and abscissa extends to 63 μs either side of zero (figure from Al-Rashid et al. 2012).

Next we illustrate in Fig. 4.11 an example of cross correlations and autocorrelations of linear FM waveforms (Al-Rashid et al. 2012). In the top panel are computed results and the cross correlation is between an up-chirp and down-chirp signal both with the same center frequency and slopes of the FM change have equal magnitudes but opposite sings.

The measurements (bottom panel) agree very well with the theoretical computations (top panel). In this case the pulse length is 63 μs and bandwidth 1 MHz so that the time bandwidth product is 63. Equivalent results can be obtained with a 12.6 μs pulse width and 5 MHz bandwidth because the time bandwidth product is the same. Measured isolation between the up and down chirp signals is ~ -14.5 dB, and integrated sidelobe level of either signal is -21.7 dB. The FM signals are weighted with a 60 dB Taylor tapper which causes a power loss of 1.87 dB.

Appendix A.1
Differential phase and Doppler velocity in the AHV polarimetric transmission mode

An example of aliasing in Doppler velocity due to the reduced unambiguous interval in Φ_{DP} is shown here and a way to overcome this problem is proposed. As stated in the report the unambiguous interval for differential phase in the ALT mode is 180° in contrast to the full 360° interval associated with the SIM transmission mode. To demonstrate the problem we took time series data collected in the SHV mode on the KOUN radar and used alternate H and V samples (Fig. A.1.1); this procedure emulates the AHV mode. This emulation is valid if there is negligible depolarization by the scattering medium, and applies to calculation of the copolar polarimetric variables.

First we examine data obtained in the Doppler mode with the PRT = 781 μs (PRF=1280 Hz) and number of pulses = 51.
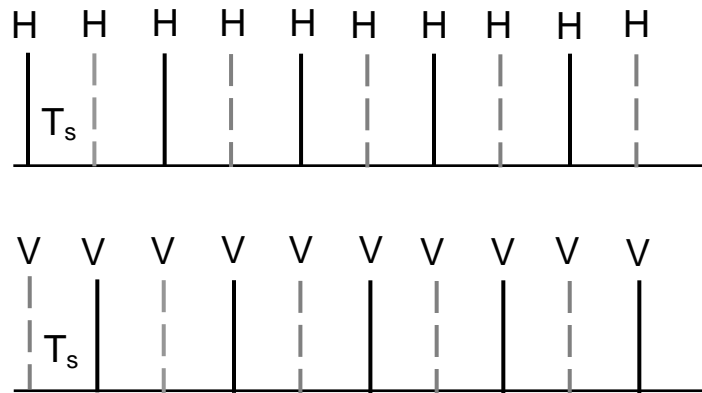
Fig. A.1.1 Simultaneous H (top) and V (bottom) samples spaced at T_s intervals. Dropping every second H (dashed line top sequence) and offset second V sample (also dashed) produces a sequence of alternating copolar H, V samples.

The SHV mode is analogous to the SIM mode on the PAR (see explanation Sec 3.3). The problem is illustrated in Fig. A.1.2 where radial profiles of reflectivity (Z, black curve), the Doppler velocity (v, green curve), and differential phase ($\Phi_{DP,}$ red curve) are depicted. In the left panel are the profiles obtained with SHV mode and the right panel depicts the same profile (same radial) as would be computed with the ALT mode if the straight forward solution of (3.7a) and (3.7b) is applied. The system differential phase is about 25° and the unambiguous interval is set from 0 to 360° in the SHV mode.

Consider the regions in precipitation but where $\Phi_{DP} < 180^o$, at distances between ~30 and 48 km from the weather echo. The Φ_{DP} and v are obtained directly from correlation function R_a and R_b (3.6a, 3.6b measured in ALT mode. At ranges beyond 48 km, the $\Phi_{DP} > 180^o$, and it aliases to positive values near zero. Introduction of these aliased values in (3.7a) or (3.7b) produces erroneous velocities Doppler velocities v (i.e., angular frequency ω_d).
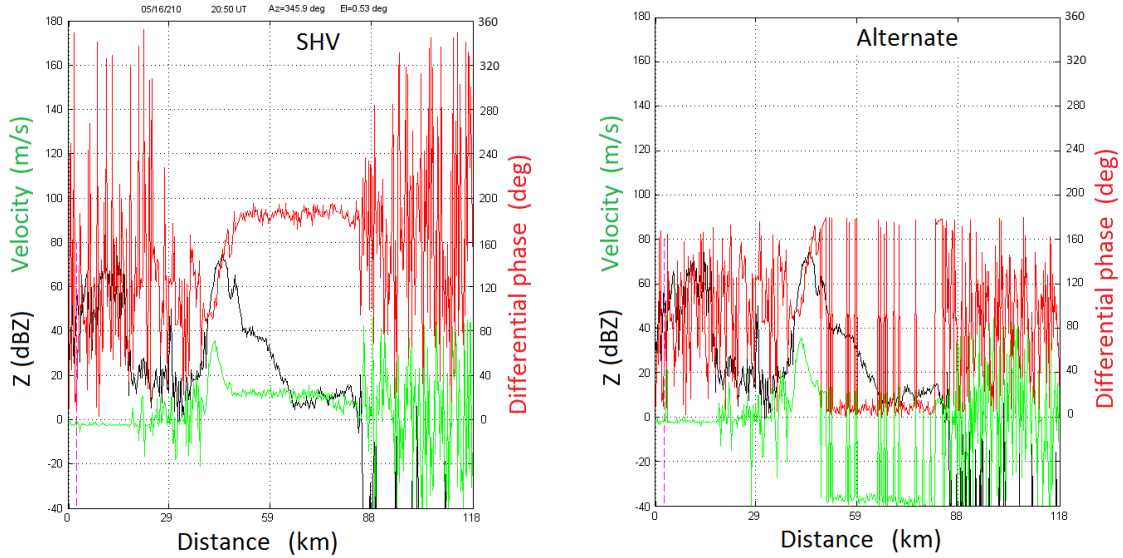
Fig. A.1.2. (left): Profiles of reflectivity (black line), the Doppler velocity (green), and differential phase (red) from data collected on May 16, 2010 at 2050Z with KOUN in SHV mode and processed accordingly. The antenna elevation is 0.5^o. (right) Same data as in the left panel but processed as would be done in the ALT mode with no special provision for extending the inherent Φ_{DP} unambiguous interval from 180° to 360°.

The measured differential phase consists of propagation part Φ_{DPpro} and system part Φ_{DPsys}:

$$\Phi_{DP} = \Phi_{DPsys} + \Phi_{DPpro}.$$

In the SHV mode the Φ_{DPsys} is adjusted to be about 25° and the unwrapping (unambiguous) phase interval is chosen from 0 to 360° (Zrnic et al. 2008). This gives a large margin before aliasing can occur because the phase typically increases through precipitation. Aliased Φ_{DP} is resolved using range continuity of the phase in weather echoes. Such resolution is applied on the dual polarization WSR-88Ds. Similar resolution over the smaller unambiguous interval (180°) is applicable in the ALT mode.

For illustration a similar algorithm is applied and the results are in Fig. A.1.2-right. From observation (continuity) note that beyond 48 km the differential phase aliases, because it exceeds 180°. Therefore one can apply a systematic phase shift (subtraction of a constant number) to the arguments of R_a and R_b, that is multiplication of these autocorrelations with $\exp(j\psi)$, where for example ψ can be -40°. This shift was applied to data shown in the right panel of Fig. A.1.2 and the result is represented in Fig. A.1.3 (left) with the blue graph. The shifted phases do not alias because their values are smaller than 180°. This shifted Φ_{DP} profile (Fig. A.1.3-left) was used to calculate the Doppler velocity. It is seen that the velocity is restored (compare the green graphs in Fig. A.1.3 - left, and Fig. A.1.2 -left). After restoring velocity the differential phase can be unbiased by adding $\psi= 40^o$ to the blue profile beyond 45 km. The result is depicted with the blues graph in Fig. A.1.3-right. Comparing this graph with Φ_{DP} profile obtained using SHV mode processing (Fig. A.1.2-left) we note that these are equal in the region of weather echo.
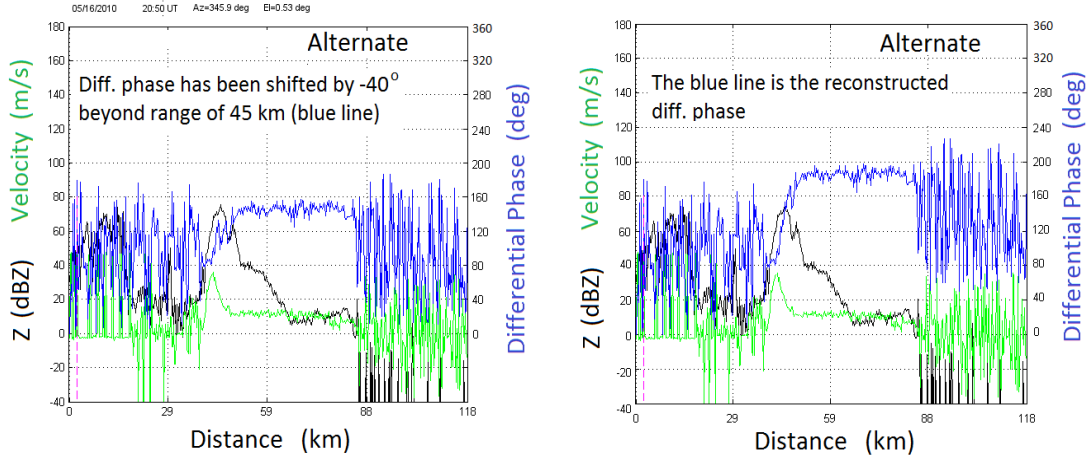
Fig. A.1.3. Illustration of the algorithm for restoration of differential phase Φ_{DP} and velocity.

This dealiasing algorithm of shifting part of Φ_{DP} profile by a fixed amount can be used in processing SHV (SIM in case of PAR) mode data. Details would need to be worked out on how to recognize automatically the beginning location where the algorithm should be applied and the value of the shift.

Obviously, automatic dealiasing is greatly facilitated by continuity in range and the fact that Φ_{DP} increases in most precipitation. In scatterers such as hail, large insects, birds, and ground clutter among other, the Φ_{DP} has no preferential value and thus challenges any automatic dealiasing scheme.

Fields of the radar variables obtained in the two modes (SHV and AHV) are presented next. Spectral moments from the Doppler scan are in Fig. A.1.4 and the corresponding polarimetric variables are in Fig. A.1.5. No continuity of Φ_{DP} is used in the computation of Doppler velocity. Therefore the discontinuity in Φ_{DP} couples into the Doppler velocity as seen in Fig. A.1.4 and A.1.5 (middle right panels). The velocities obtained from emulated AHV mode close to the radar have a significant number of values below -10 m s^{-1} likely because of coupling with Φ_{DP} from ground clutter (backscatter differential phase has a wide distribution over 360° interval). Clutter filter would reduce this kind of contamination but was not applied on this data. Other differences include larger (biased) spectrum widths in the north storms, noisier Z_{DR} and ρ_{hv} in the storms (regions of large ρ_{hv}) and smaller ρ_{hv} (biased) there.

Next we present the fields of polarimetric variables obtained from surveillance scans wherein the PRF=322 Hz and the total number of pulses = 16. Therefore in the "emulated" AHV mode the number of pulses with equal polarizations is 8. Although the dwell times for the SHV and AHV mode are equal the data quality in AHV mode is degraded. This is apparent in Z_{DR}, ρ_{hv}, and Φ_{DP} but not obvious in Z, likely because the quantization interval of Z is quite coarse. Note the speckles (noisy character) of the polarimetric variables and the systematic decrease (bias as predicted in appendix A.2) of ρ_{hv} in regions of weather echo.
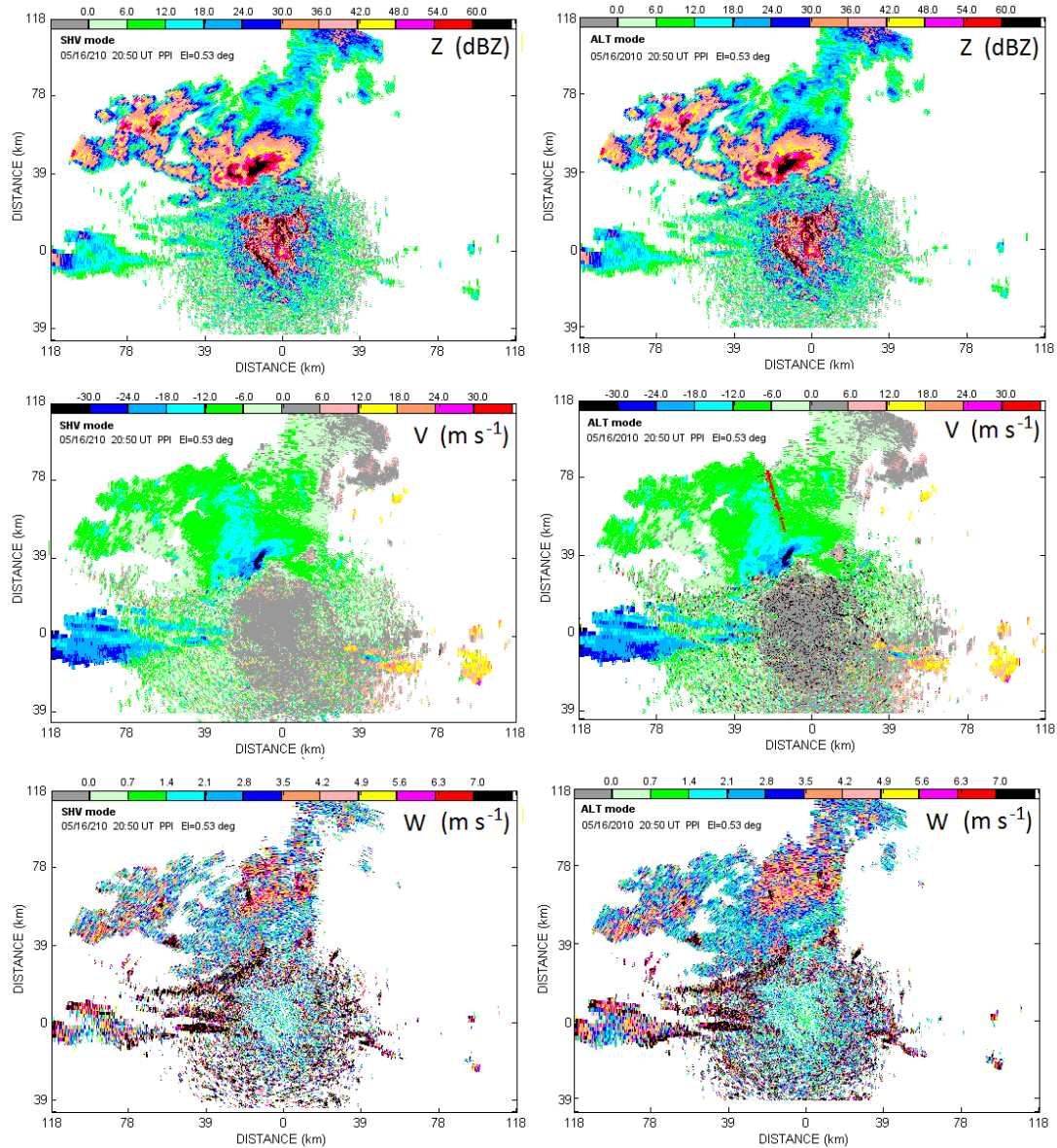
Fig. A.1.4. Spectral moments: Left) in the SHV mode (51 pulses averaged, and PRF=1280 Hz. Right) AHV (emulated) mode using the same data as in a) but alternating between the H and V samples (25 H and 25 V returns). Note the radial discontinuity in velocity (AHV mode) at about -10° from North caused by aliased Φ_{DP} (see Fig. A.1.5).
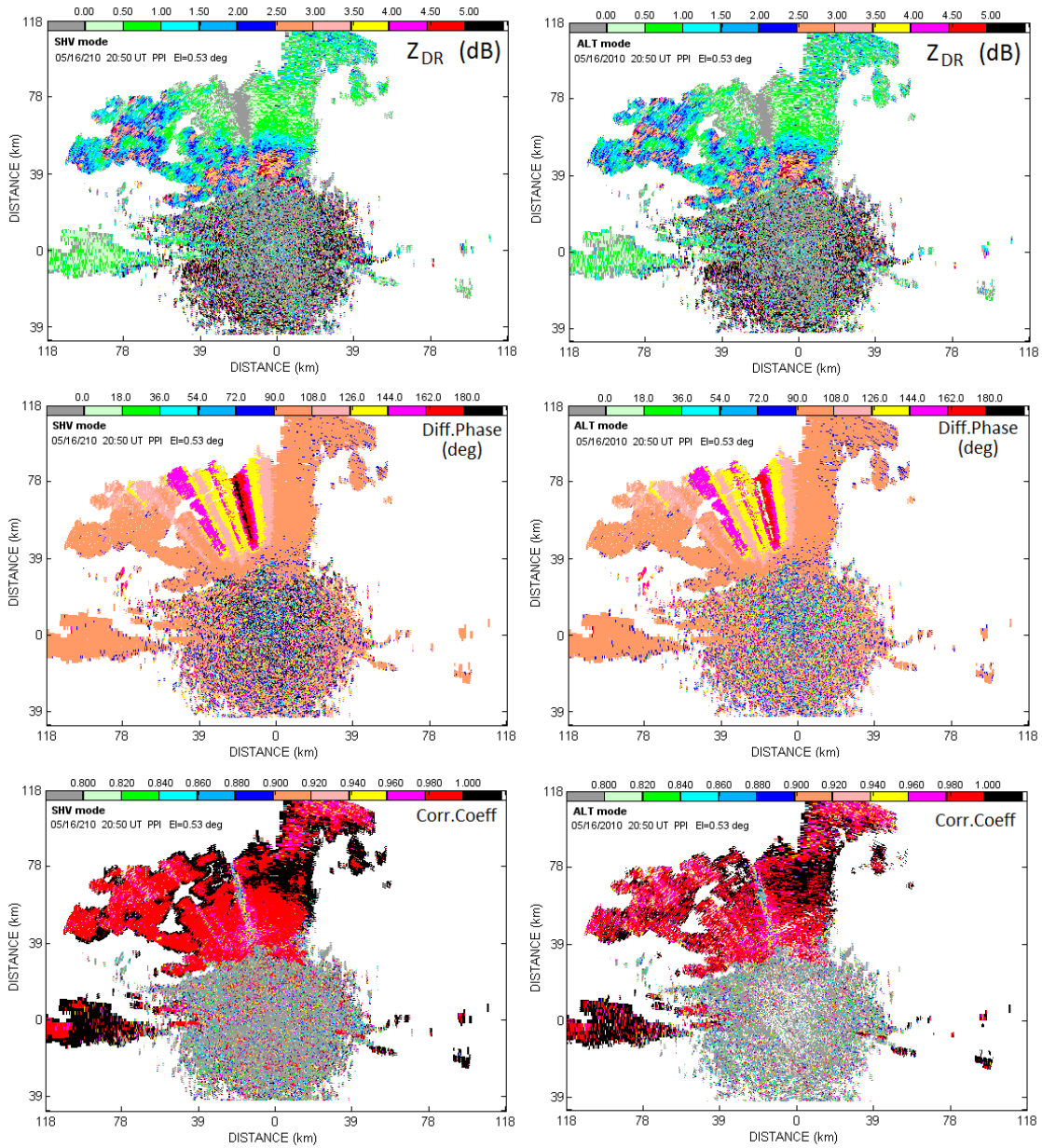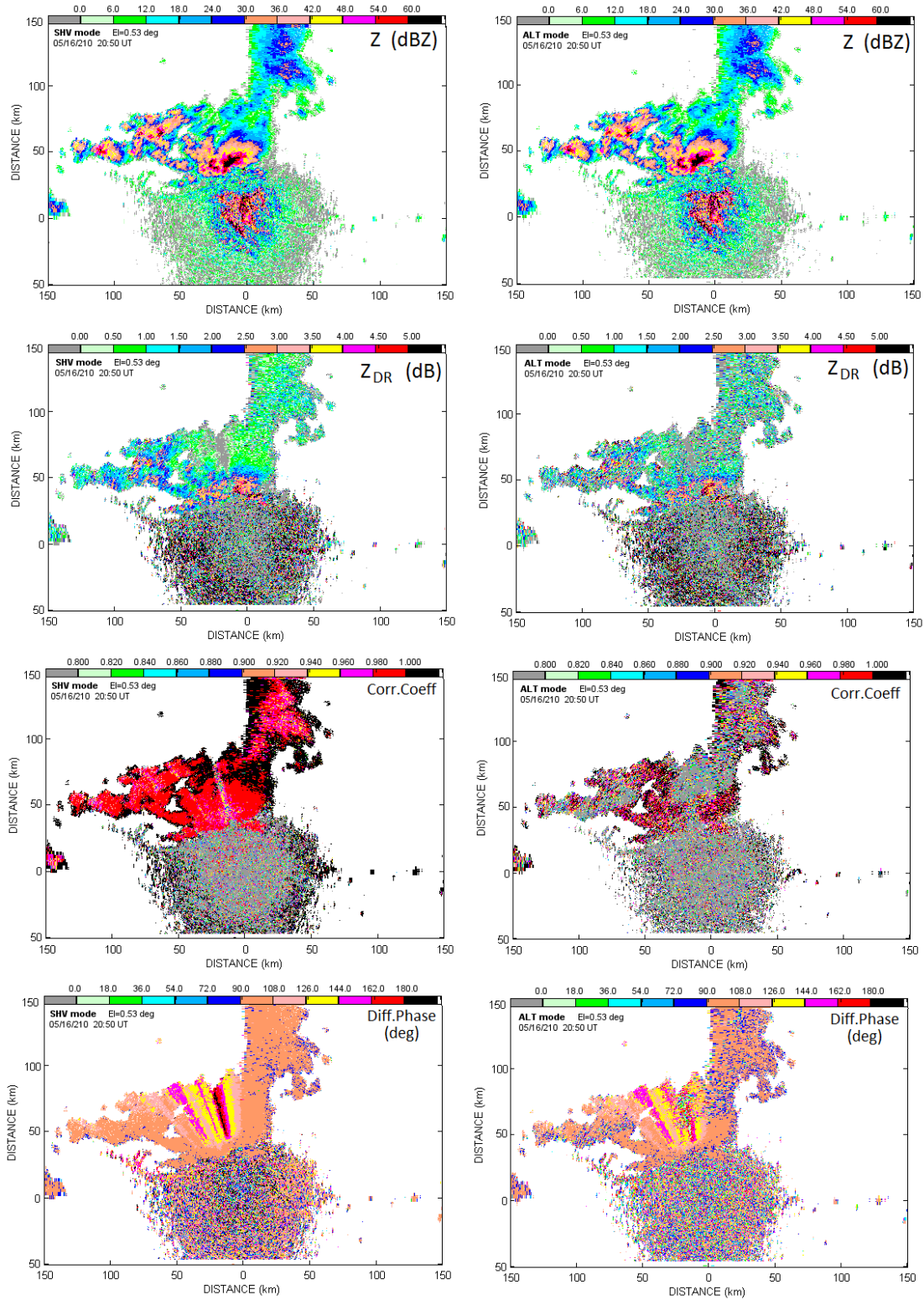
Fig. A.1.5. The polarimetric variables: Left) in the SHV mode (51 pulses averaged, and PRF=1280 Hz. Right) AHV (emulated) mode using the same data as in Left) but alternating between the H and V samples. The radially elongated feature at about -10° from North is aliased because the Φ_{DP} unwrapping interval exceeds 180°.

Fig. A.1.6. The polarimetric variables: Left) in the SHV mode (16 pulses averaged, and PRF=322 Hz. Right) AHV (emulated) mode using the same data as in Left) but alternating between the H and V samples (8 H and 8 V returns).

Appendix A.2

Statistics of the polarimetric variables estimated in the AHV and SHV modes of data collection

A2.1. Simultaneous and alternate transmission modes

Simultaneous transmission and reception of electromagnetic waves with horizontal and vertical polarizations has been chosen as the mode for the WSR-88D weather radar (Doviak et al. 2000). We will refer to this mode as **SHV**, i.e., **S**imultaneous transmission and reception of **H**orizontally and **V**ertically polarized waves. In the mode, six radar moments are estimated from each radar resolution volume: reflectivity, Z, Doppler velocity, v, spectrum width, σ_v , differential reflectivity, Z_{DR}, differential phase, Φ_{DP}, and modulus of copolar correlation coefficient, ρ_{hv}. The first three values are the basic radar products of the WSR-88D, the latter three are basic polarimetric variables. Another polarimetric variable, the specific differential phase, K_{DP}, is calculated from Φ_{DP}. Definitions of the parameters can be found in Doviak and Zrnic (2006). SHV polarimetric mode has been implemented on weather radars in Germany, France, Finland, and many other places.

The alternate transmission of horizontally and vertically polarized waves (**AHV**) was historically the first polarimetric mode (e.g., Seliga and Bringi, 1976). The mode was implemented using a mechanical or ferrite switches. Pulse sequences in the SHV and AHV mode are shown in Fig. A.2.1 with the same interpulse period T.   Pulses in the channel with horizontally polarized waves are designated as H_m and pulses in the channel with vertically polarized waves are designated as V_m, where m = 1, 2, …,M and M is the total number of samples in the dwell time.
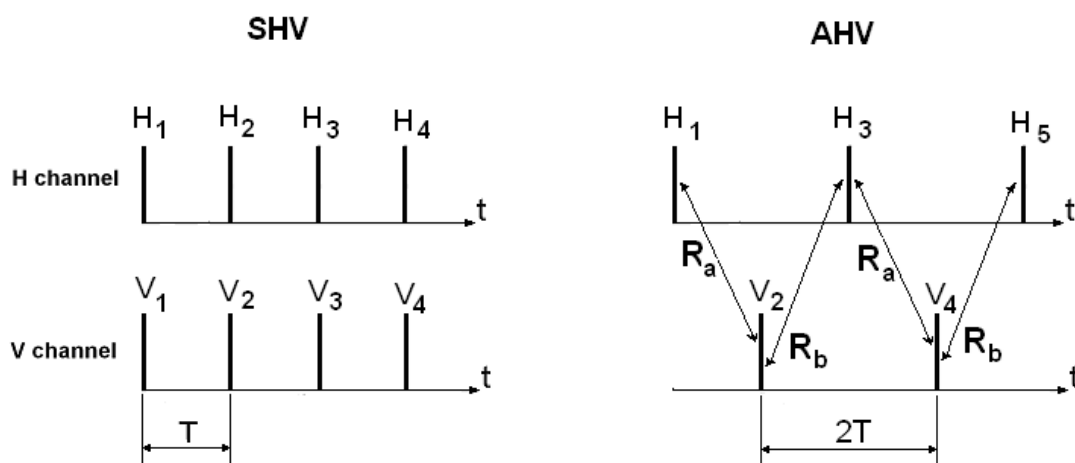

Fig.A.2.1. Schematic representation of pulse sequences in the SHV and AHV modes.

Recent interest in the AHV mode is due to the challenge in polarimetric observations with the phased array radars, PAR. The cost of a PAR antenna with transceivers that transmit and receive H and V waves simultaneously is very high. The cost of PAR antennas with transceivers that use AHV mode is lower. So it is of interest to compare the qualities of polarimetric estimates in the AHV mode with that in the SHV mode. The latter can be considered as a "benchmark" for polarimetric measurements because statistical errors of polarimetric estimates in that mode are lower than those in the AHV modes. Some coupling between H and V scattered waves in the SHV mode (Doviak et al., 2000; Hubbert et al., 2010) can be considered as a side effect of the simultaneous transmission but it is tolerable. So herein we present results of calculations of the statistical properties of Z, Z_{DR}, Φ_{DP}, ρ_{hv} in the AHV mode and compare them with the ones for the SHV mode.

To compare statistical properties of estimates in the AHV and SHV modes, we use the same dwell time, i.e., the same time of measurements. We consider herein the dwell time which is currently used on the dual-polarization WSR-88Ds in the split cuts. The latter consists of two sweeps made at the same antenna elevation. The first is called surveillance cut where estimates use 16 pulses with the pulse repetition frequency, PRF, of 320 Hz . The second sweep is called Doppler cut consisting of 51 pulses at PRF of 1280 Hz (the exact PRF and number of samples can vary a little for a particular radar and even from radial to radial). The surveillance cut is used to obtain reflectivity and polarimetric variables to large ranges and the Doppler cut is used to measure the Doppler velocity and spectrum width. The dwell time parameters in VCP21 of the WSR-88D are shown in table 1.

Table A.2.1. Dwell times in the split cut of VCP 12 of the WSR-88D, SHV mode

Cut	# of samples	PRF, Hz	Dwell time, ms
Surveillance	16	320	50
Doppler	51	1280	40

To calculate the polarimetric variables in the AHV mode, we use herein algorithms proposed by Sachidananda and Zrnic (1985, 1989), Zrnic (1991), Zahrai and Zrnic (1993), Zrnic et al. (1994). Because the AHV mode affects the accuracy of reflectivity measurements, we include this moment in our analysis. Reflectivity, Z, is estimated from measured power in the H-channel (see the right panel in Fig.A.2.1):

$$\hat{P}_h = \frac{1}{M} \sum_{m=1}^{M} H_{2m-1} H_{2m-1}^*, \qquad \hat{Z} = 10 \log_{10}\left(\hat{P}_h - N_h\right), \text{(dBZ)}, \quad \text{(A.2.1)}$$

where the asterisk denotes complex conjugate, the hat designates the estimate, and N_h is the noise power in the H-channel. N_h is measured using a very large number of samples thus it can be considered as true value (that is why it does not have the hat). In formula for Z we have omitted parameters related to radar calibration and the range dependence because they do not affect the estimate's statistical properties.

Differential reflectivity is calculated from power measurements in the horizontal and vertical channels as,

$$\hat{Z}_{dr} = \frac{\hat{P}_h - N_h}{\hat{P}_v - N_v}, \qquad \hat{Z}_{DR} = 10\log\hat{Z}_{dr} \text{ (dB)}, \qquad (A.2.2)$$

The differential phase Φ_{DP} and the modulus of correlation coefficient ρ_{hv} are obtained from calculated correlation function $\hat{R}_a$ and $\hat{R}_b$

$$\hat{R}_a = \frac{1}{M}\sum_{m=1}^{M} H^*_{2m-1}V_{2m}, \qquad \hat{R}_b = \frac{1}{M}\sum_{m=1}^{M} H_{2m+1}V^*_{2m}, \qquad (A.2.3)$$

$$\hat{\Phi}_{DP} = 90\arg(\hat{R}_a\hat{R}^*_b)/\pi \text{ (deg)}, \qquad (A.2.4)$$

$$\hat{\rho}_{hv} = \frac{|\hat{R}_a| + |\hat{R}_b|}{2(\hat{S}_h\hat{S}_v)^{1/2}[\hat{\rho}(2T)]^{1/4}}, \qquad (A.2.5)$$

where $\hat{\rho}(2T)$ is the estimate of the weather signal correlation coefficient, and S_h, S_v are the weather signal powers,

$$\hat{S}_h = \hat{P}_h - N_h, \qquad \hat{S}_v = \hat{P}_v - N_v. \qquad (A.2.6)$$

Pairs of pulses in the calculations of $\hat{R}_a$ and $\hat{R}_b$ are shown in the right panel in Fig. A.2.1.

To calculate the biases and standard deviations of the estimates, the following auto-covariances and cross-covariances are needed

$$<H_nH^*_m> = S_h\rho[(m-n)T]\exp[j\pi v(m-n)] + N_h\delta_{nm}, \qquad (A.2.7)$$

$$<V_nV^*_m> = S_v\rho[(m-n)T]\exp[j\pi v(m-n)] + N_v\delta_{nm}, \qquad (A.2.8)$$

$$<H_nV^*_m> = (S_hS_v)^{1/2}\rho_{hv}\rho[(m-n)T]\exp(j\Phi_{DP}), \qquad (A.2.9)$$

where the brackets denote statistical averaging, ρ_{hv} is the modulus of the intrinsic copolar correlation coefficient, and v_n is the normalized Doppler velocity, and δ_{nm} is the Kroneker symbol.

A2.2 Accuracy of reflectivity estimates

Reflectivity in the AHV mode is calculated according to (A.2.1). The standard deviation of the estimate is calculated herein using the perturbation technique. The perturbation equation for reflectivity follows from (A.2.1):

$$\delta \hat{Z} = \frac{10}{\ln 10} \frac{\delta \hat{P}_h}{S_h},$$

where δ stands for variations and quantities without the hat stand for true means. The standard deviation (SD) follows from the latter as

$$SD(\hat{Z}) = \frac{10}{\ln(10)} \frac{<\delta^2 \hat{P}_h>^{1/2}}{S_h} \text{ (dB)}.$$

The variance of the power can be found in Melnikov and Zrnić (2004); using that result we obtain

$$SD(\hat{Z}) = \frac{10}{\ln 10 M^{1/2}} \left(\frac{2SNR_h + 1}{SNR_h^2} + \frac{1}{m_I} \right)^{1/2} \text{ (dB)}, \qquad \text{(A.2.10)}$$

$$m_I = M_I / M = \left(1 + 2 \frac{S^2}{(S+N)^2} \sum_{m=1}^{M-1} (1 - m/M) \rho^2 (2mT) \right)^{-1}. \quad \text{(A.2.11)}$$

M_I is frequently called the equivalent number of independent samples and it depends on the signal correlation coefficient $\rho(nT)$ (a function of the Doppler spectrum width) as well as SNR; m_I is the relative number of independent samples of the signal plus noise. For the Gaussian Doppler spectra, the weather signal correlation coefficient $\rho(nT)$ is

$$\rho(nT) = \exp \left[-\frac{1}{2} \left(\frac{4\pi \sigma_v nT}{\lambda} \right)^2 \right]. \qquad \text{(A.2.12)}$$

where λ is the radar wavelength. The first term in the parenthesis in (A.2.10) is due to finite signal-to-noise ratio (SNR) in the channel and the second term results from correlation of signal plus noise samples.

In Fig. A.2.2, SD(Z) are shown for the AHV and SHV modes for the same dwell time and SNR > 20 dB. SD(Z)s for the surveillance scan are calculated using (A.2.10) for the AHV mode and corresponding formulas from Melnikov and Zrnić (2004) and Doviak and Zrnić (2006, Errata and Supplements) for the SHV mode; the results are shown with the red and magenta curves. The WSR-88D uses 16 samples to estimate reflectivity in the SHV mode; the dwell time is 50 ms. In the AHV mode during the same dwell time only 8 pulses are available. It is seen from the curves that SD(Z) for the AHV mode is higher than that for the SHV mode but the difference is about 0.5 dB for $\sigma_v > 4$ m s^{-1}, which is acceptable. To verify our theoretical results, we have ran signal simulations,

results some of which are shown in Fig. A.2.2 with the circles and triangles. It is seen that the simulations confirm the theoretical outcome.

For the Doppler cut (the blue and green curves in Fig. A.2.2), 25 samples are available in the AHV mode out of 51 samples in the SHV mode and we see that SD(Z) are practically the same because the dwell times are equal. Simulation results are shown with the stars and pluses and confirm the theoretical calculations.
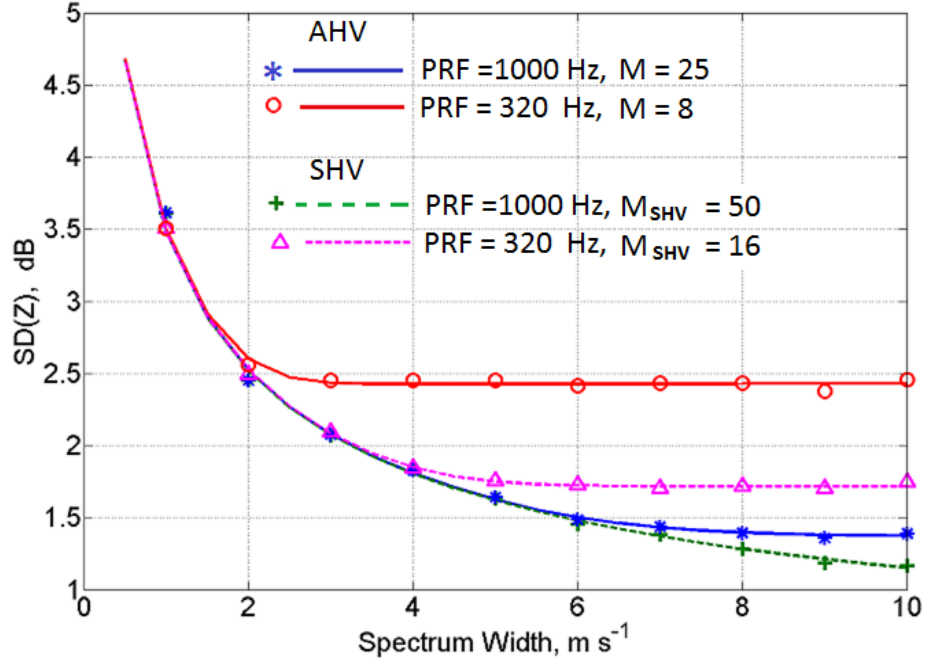

Fig. A.2.2. The theoretical standard deviations of reflectivity as a function of spectrum width for AHV (solid lines) and SHV (dash lines) modes using equal dwell times. The symbols are simulation results. SNR > 20 dB.

A2.3. Statistics of differential reflectivity

Differential reflectivity in the AHV mode is calculated according to (A.2.2) and the perturbation equation for $\hat{Z}_{DR}$ follows:

$$\delta \hat{Z}_{DR} = \frac{10}{\ln 10}\left(\frac{\delta \hat{S}_h}{S_h} - \frac{\delta \hat{S}_v}{S_v} \right).$$

(A.2.13)

The variance is

$$<\delta^2 \hat{Z}_{DR}> = \left(\frac{10}{\ln 10}\right)^2 \left(\frac{<\delta^2 \hat{S}_h>}{S_h^2} + \frac{<\delta^2 \hat{S}_v>}{S_v^2} - 2\frac{<\delta \hat{S}_h \delta \hat{S}_v>}{S_h S_v} \right).$$

(A.2.14)

`

96

The variances of powers are obtained from (A.2.10). The covariance $< \delta \hat{S}_h \delta \hat{S}_v >$ equals $< \delta \hat{P}_h \delta \hat{P}_v >$ because S and P differ by constant noise. The covariance $< \delta \hat{P}_h \delta \hat{P}_v >$ is

$$< \delta \hat{P}_h \delta \hat{P}_v >= < \hat{P}_h \hat{P}_v > -P_h P_v = \frac{1}{M^2} \sum_{m,n=1}^{M} <H_{2m-1}^* H_{2m-1} V_{2n}^* V_{2n} > -P_h P_v =$$

$$\frac{1}{M^2} \sum_{m,n=1}^{M} <H_{2m-1}^* H_{2m-1} >< V_{2n}^* V_{2n} > + \frac{1}{M^2} \sum_{m,n=1}^{M} <H_{2m-1}^* V_{2n} >< V_{2n}^* H_{2m-1} > -P_h P_v .$$

The latter factorized string is written because H_m and V_m are zero mean Gaussian signals (see, e.g., Whalen 1971, section 4.1). Substitution of (A.2.7) – (A.2.9) into the latter equation yields

$$< \delta \hat{S}_h \delta \hat{S}_v >= \frac{S_h S_v}{M^2} \rho_{hv}^2 \sum_{m,n=1}^{M} | \rho\{[2(m-n)+1]T\} |^2 . \qquad \text{(A.2.15)}$$

Denoting

$$m_{I1} = M[\sum_{m,n=1}^{M} | \rho\{[2(m-n)+1]T\} |^2]^{-1} \qquad \text{(A.2.16)}$$

we write $SD(\hat{Z}_{DR})$ for the AHV mode as,

$$SD(\hat{Z}_{DR}) = \frac{10}{\ln 10 M^{1/2}} \left(\frac{2SNR_h+1}{SNR_h^2} + \frac{2SNR_v+1}{SHR_v^2} + \frac{2}{m_I} - \frac{2\rho_{hv}^2}{m_{I1}} \right)^{1/2} \text{(dB)}. \quad \text{(A.2.17)}$$

For the SHV mode (Melnikov and Zrnic, 2007):

$$SD(\hat{Z}_{DR}, SHV) = \frac{10}{\ln 10 M^{1/2}} \left(\frac{2SNR_h+1}{SNR_h^2} + \frac{2SNR_v+1}{SHR_v^2} + \frac{2(1-\rho_{hv}^2)}{m_{I0}} \right)^{1/2} \text{(dB)}, \quad \text{(A.2.18)}$$

with

$$m_{I0} = \left(1 + 2 \sum_{m=1}^{M-1} (1-m/M) | \rho(mT) |^2 \right)^{-1} . \qquad \text{(A.2.19)}$$

We compare $SD(\hat{Z}_{DR})$ in AHV and SHV modes for the same dwell time which means that M in (A.2.17) is two times smaller than M in (A.2.18) for uniform pulse sequences.

(A.2.17) and (A.2.18) are quite different: (A.2.17) depends upon $\rho(2mT)$ as it is seen from (A.2.6) whereas (A.2.18) depends on $\rho(mT)$, [see (A.2.19)]. Comparisons of $SD(\hat{Z}_{DR})$ for the same dwell time in AHV and SHV modes for the surveillance and Doppler cuts of the WSR-88Ds are in Fig. A.2.3 for ρ_{hv} =0.98 and SNR > 20 dB. It is seen that for the Doppler sweep, $SD(\hat{Z}_{DR})$ are close at spectrum widths smaller than 6 m s^{-1}. For the surveillance cut, AHV performance is too bad to be used in radar. The symbols in Fig. A.2.3 represent results of signal simulations. One can see that the results are very close to the theoretical curves.
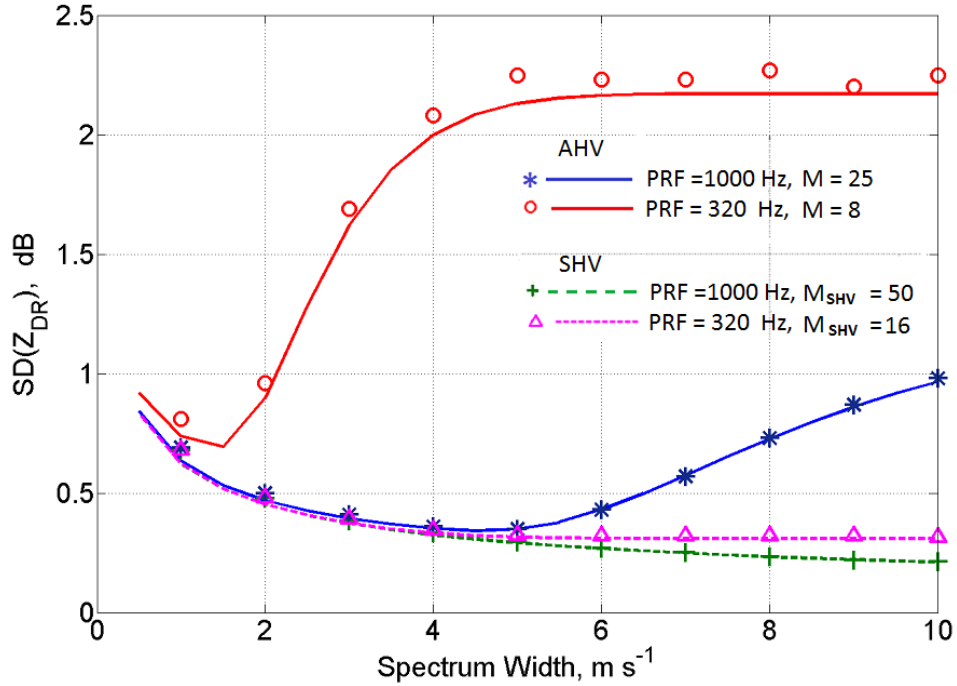

Fig. A.2.3. Theoretical standard deviations of differential reflectivity as a function of spectrum width for AHV (solid lines) and SHV (dash lines) modes for equal dwell times, SNR > 20 dB and ρ_{hv}=0.98. The symbols represent simulation results.

One important conclusion can be drawn from Fig. A.2.3. It is seen that for spectrum widths less than 6 m s^{-1}, and for operation at high PRF, the SD for AHV and SHV modes are equal although the number of samples differ by two times. That means that the SD depends upon the dwell time, which is equal for the modes, but does not depend directly on the number of samples. This can be proven by considering limits of m_{I0}, m_I, and m_{I1}. Begin with m_I. Consider the sum entering in (A.2.16)

$$J = \frac{1}{M} \sum_{m=1}^{M-1} (1 - m/M) \mid \rho(2mT) \mid^2 \qquad (A.2.20)$$

For large m, $\rho(x)$ decreases fast and the sum can be replaces with the following integral:

$$J \approx \frac{1}{M} \int_0^{M-1} (1 - x/M) \, | \, \rho(2x) \, |^2 \, dx \quad . \tag{A.2.21}$$

For Gaussian spectra,

$$|\rho(n)| = \exp[- (4\pi\sigma_v Tn/\lambda)^2/2]. \tag{A.2.22}$$

Substitution the latter into (A.2.21) for large M yields

$$J \approx \frac{\lambda}{16\pi^{1/2}\sigma_v MT} \quad . \tag{A.2.23}$$

For the SHV mode we can apply a similar approximation for (A.2.19) and get

$$J_0 \approx \frac{1}{M_{SHV}} \int_0^{M_{SHV}-1} [1 - x/(M_{SHV})] \, | \, \rho(x) \, |^2 \, dx \quad .$$

For Gaussian spectrum (A.2.22) we have

$$J_0 \approx \frac{\lambda}{8\pi^{1/2}\sigma_v M_{SHV}T} \quad . \tag{A.2.24}$$

For the same dwell time, i.e., $M_{SHV} = 2M$, and (A.2.24) and (A.2.23) become equal. Thus for moderate spectrum widths, SD depends only upon the dwell time. That is why the green and blue lines in Fig. A.2.3 are close to each other at such spectrum widths.

The SD for AHV mode increases beyond $\sigma_v = 6$ m s^{-1}. This is because approximation (A.2.21) does not hold for such spectrum widths and the main addends in (A.2.16) (with $m = n$) become

$$m_{I1} \approx M[\sum_{m,n=1}^{M} | \, \rho(T) \, |^2]^{-1} = | \, \rho(T) \, |^{-2} \, . \tag{A.2.25}$$

$SD(\hat{Z}_{DR})$ in (A.2.17) is inversely proportional to square root of m_{I1} thus its dependence is proportional to $|\rho(T)|$. At large spectrum widths, $|\rho(T)|$ is small so the negative contribution in (A.2.17) decreases and the total value increases. This increase we observe in $SD(\hat{Z}_{DR})$ at large widths (the blue line in Fig. A.2.3).

For the surveillance cut (the red line in Fig. A.2.3) the normalized spectrum widths are not small so SD becomes large at moderate widths. Thus it is hard to justify the use of Z_{DR} measurements in the surveillance sweep.

A2.4. Statistics of the differential phase

99

To calculate statistical properties of the differential phase estimate in the AHV mode, begin with the perturbation equation derived from (A.2.4) expressed in radians:

$$\delta\hat{\Phi}_{DP} = \frac{1}{2}\arg[\,\delta(\hat{R}_a\hat{R}_b^*)] = \frac{1}{2}\text{Im}\left(\frac{\hat{R}_a}{R_a}\right) + \frac{1}{2}\text{Im}\left(\frac{\hat{R}_b^*}{R_b^*}\right), \qquad (A.2.26)$$

where the right-hand equation is written according to (3.3) from Melnikov and Zrnic (2004). From (A.2.26) we obtain the variance:

$$<\delta^2\Phi_{DP}> = \frac{1}{4}<\text{Im}^2\left(\frac{\hat{R}_a}{R_a}\right)> + \frac{1}{4}<\text{Im}^2\left(\frac{\hat{R}_b^*}{R_b^*}\right)> + \frac{1}{2}<\text{Im}\left(\frac{\hat{R}_a}{R_a}\right)\text{Im}\left(\frac{\hat{R}_b}{R_b}\right)>$$

Using the following identities that hold for any complex x and y,

$$\text{Im}^2(x) = \frac{1}{2}[|x|^2 - \text{Re}(x^2)], \quad \text{Im}(x)\text{Im}(y) = \frac{1}{2}[\text{Re}(xy^*) - \text{Re}(xy)],$$

we write

$$8<\delta^2\Phi_{DP}> = <\left|\frac{\hat{R}_a}{R_a}\right|^2> - \text{Re}<\left(\frac{\hat{R}_a}{R_a}\right)^2> + <\left|\frac{\hat{R}_b^*}{R_b^*}\right|^2> - \text{Re}<\left(\frac{\hat{R}_b}{R_b}\right)^2> +$$

$$2\,\text{Re}<\left(\frac{\hat{R}_a\hat{R}_b}{R_aR_b}\right)> - 2\,\text{Re}<\left(\frac{\hat{R}_a\hat{R}_b^*}{R_aR_b^*}\right)>. \qquad (A.2.27)$$

To make the number of products in calculations of these variances and covariances equal, we add an additional pulse in the H-channel, i.e., H_{M+1} shown in Fig. A.2.4 with the dash line. This additional pulse does not change the statistics of estimates noticeably but simplifies calculations significantly. The pulse allows calculating one more product for $\hat{R}_b^*$, i.e., $H_{M+1}\,V_M^*$, and makes the number of products in $\hat{R}_b^*$ equal to the one for $\hat{R}_a$, i.e., M.
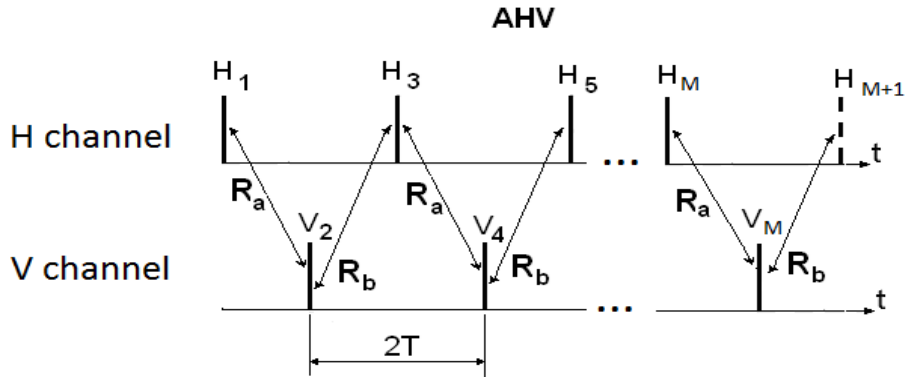
AHV

Fig. A.2.4. Calculations of R_a and R_b; an additional pulse H_{M+1} shown with the dash line.

For the first term in (A.2.27) we have

$$<|\hat{R}_a|^2> = \frac{1}{M^2} \sum_{m,n=1}^{M} <H^*_{2m-1}V_{2m}H_{2n-1}V^*_{2n}> = \frac{1}{M^2} \sum_{m,n=1}^{M} <H^*_{2m-1}V_{2m}><H_{2n-1}V^*_{2n}> +$$

$$\frac{1}{M^2} \sum_{m,n=1}^{M} <H^*_{2m-1}H_{2n-1}><V_{2m}V^*_{2n}> = S_h S_v \rho_{hv}^2 |\rho(T)|^2 + \frac{(S_h+N_h)(S_v+N_v)}{M} +$$

$$\frac{S_h S_v}{M^2} \sum_{m,n=1}^{M} |\rho[(2n-2m)T]|^2$$

It follows from (A.2.3) and (A.2.9) that $|R_a|^2 = S_h S_v \rho_{hv}^2 |\rho(T)|^2$ so the first term in (A.2.27) can be written as,

$$\frac{<|\hat{R}_a|^2>}{|R_a|^2} = 1 + \frac{SNR_h + SNR_v}{M \; SNR_h SNR_v \rho_{hv}^2 |\rho(T)|^2} + \frac{S_h S_v}{M m_I \rho_{hv}^2 |\rho(T)|^2} \, . \qquad (A.2.28)$$

The second term on right side of (A.2.27) can be obtained from the following:

$$\frac{<\hat{R}_a^2>}{R_a^2} = \frac{1}{M^2 R_a^2} \sum_{m,n=1}^{M} <H^*_{2m-1}V_{2m}H^*_{2n-1}V_{2n}> = \frac{1}{M^2 R_a^2} \sum_{m,n=1}^{M} <H^*_{2m-1}V_{2m}><H^*_{2n-1}V_{2n}> +$$

$$\frac{1}{M^2 R_a^2} \sum_{m,n=1}^{M} <H^*_{2m-1}V_{2n}><V_{2m}H^*_{2n-1}> =$$

$$1 + \frac{S_h S_v}{M^2 |\rho(T)|^2} \sum_{m,n=1}^{M} |\rho[(2n-2m+1)T]|\,\|\,\rho[(2m-2n+1)T]| \, . \qquad (A.2.29)$$

For symmetric spectra (e.g., the Gaussian spectra), function $|\rho(nT)|$ is an even function. It can be shown that for such spectra

$$\frac{<\hat{R}_b^{*2}>}{R_b^{*2}} = \frac{<\hat{R}_a^2>}{R_a^2} \quad \text{and} \quad \frac{<|\hat{R}_b|^2>}{|R_b|^2} = \frac{<|\hat{R}_a|^2>}{|R_a|^2} \, . \qquad (A.2.30)$$

Equation (A.2.30) can be proven by calculating relations similar to (A.2.28) and (A.2.29). Now we calculate the fifths term on the right hand side of (A.2.27):

$$\frac{<\hat{R}_a\hat{R}_b>}{R_aR_b} = \frac{1}{M^2R_aR_b}\sum_{m,n=1}^{M}<H^*_{2m-1}V_{2m}H_{2n+1}V^*_{2n}> = \frac{1}{M^2R_aR_b}\sum_{m,n=1}^{M}<H^*_{2m-1}V_{2m}><H_{2n+1}V^*_{2n}> +$$

$$\frac{1}{M^2R_aR_b}\sum_{m,n=1}^{M}<H^*_{2m-1}H_{2n+1}><V_{2m}V^*_{2n}> =$$

$$1 + \frac{(SNR_h + SNR_v)\,|\,\rho(2T)\,|}{M\ SNR_h SNR_v \rho^2_{hv}\,|\,\rho(T)\,|^2} + \frac{1}{Mm_{I2}\rho^2_{hv}\,|\,\rho(T)\,|^2}\,, \tag{A.2.31}$$

$$\text{where}\quad m_{I2} = M\left(\sum_{m,n=1}^{M}|\,\rho[(2m-2n-2)T]\,\|\,\rho[(2n-2m)T]\,|\right)^{-1}. \tag{A.2.32}$$

The last term in (A.2.27) can be calculated similarly:

$$\frac{<\hat{R}_a\hat{R}^*_b>}{R_aR^*_b} = 1 + \frac{1}{Mm_{I1}\,|\,\rho(T)\,|^2}\,. \tag{A.2.33}$$

Substitution (A.2.28) − (A.2.33) into (A.2.27) yields

$$SD(\Phi_{DP}) = \frac{1}{2M^{1/2}\rho(T)\rho_{hv}}\left(\frac{SNR_h[1+|\,\rho(2T)\,|]+SNR_v[1+|\,\rho(2T)\,|]}{SNR_h SNR_v} + \right.$$

$$\left.\frac{1}{m_{I1}} - \frac{\rho^2_{hv}}{m_{I3}} + \frac{1}{m_{I2}} - \frac{\rho^2_{hv}}{m_{I1}}\right)^{1/2} \tag{A.2.34}$$

where

$$m_{I3} = M\left(\sum_{m,n=1}^{M}\rho[(2m-2n+1)T]\rho^*[(2n-2m+1)T]\right)^{-1}.$$

For the SHV mode, the standard deviation of Φ_{DP} is (Melnikov and Zrnic, 2007)

$$SD(\Phi_{DP}, SHV) = \frac{1}{(2M)^{1/2}\rho_{hv}}\left(\frac{SNR_h + SNR_v + 1}{SNR_h\ SNR_v} + \frac{1-\rho^2_{hv}}{m_{I0}}\right)^{1/2}\ \text{(rad)} \tag{A.2.35}$$

It can be seen that for small spectrum widths, i.e., for $\rho(T)$ and $\rho(2T)$ close to 1, m_{In} in (A.2.34) is close to m_{I0} and $SD(\Phi_{DP}, AHV)$ becomes equal to $SD(\Phi_{DP}, SHV)$. This can also be seen from the right panel in Fig. A.2.5 at small spectrum widths. It is seen from Fig. A.2.5 that in the Doppler mode at $\sigma_v < 6$ m s^{-1}, statistical errors in the differential phase are about equal for the AHV and SHV modes. But for larger spectrum width the

errors in the AHV mode increase fast. This is caused by $\rho(T)$ in the denominator of (A.2.34) similar to the $SD(\hat{Z}_{DR})$ in the previous section. For the surveillance sweep (the left panel in Fig. A.2.5), errors in the AHV mode become unacceptably large at $\sigma_v > 2$ m s^{-1} and the estimates become useless.
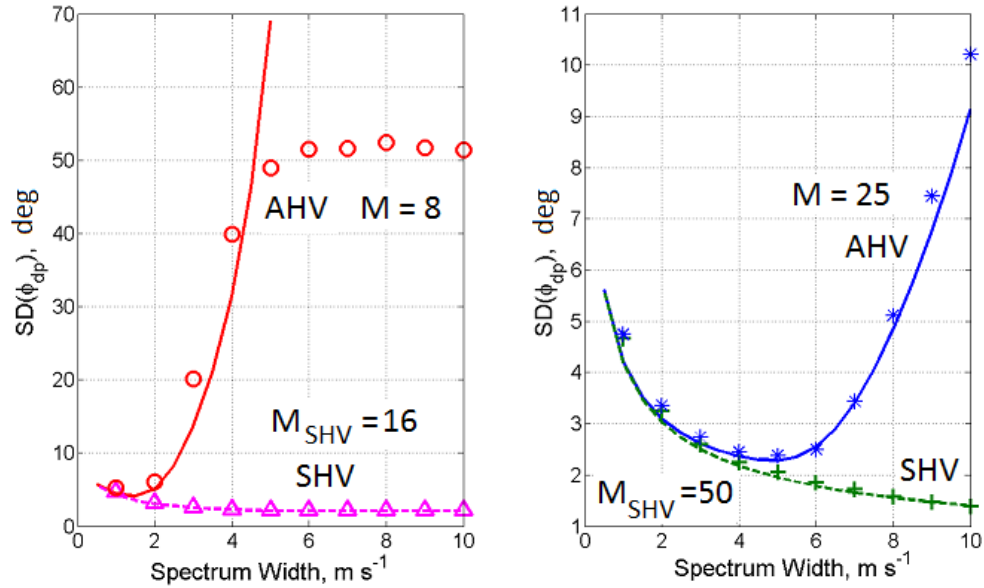

Fig. A.2.5. Theoretical standard deviations of the differential phase as a function of spectrum width for AHV (solid lines) and SHV (dash lines) modes using equal dwell times. The symbols are simulation results. The left panel corresponds to the surveillance cut of the WSR-88D (PRF = 320 Hz) and the right panel is for the Doppler cut with PRF = 1000 Hz, SNR > 20 dB. In either case $\rho_{hv}=0.98$.
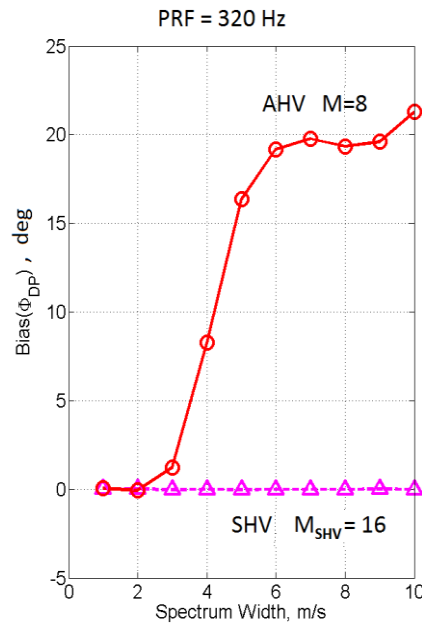
Fig. A.2.6. Bias of the differential phase as a function of spectrum width for AHV (solid lines) and SHV (dash lines) modes for equal dwell times. The symbols are simulation results with lines connecting points. The surveillance cut of the WSR-88D (PRF = 320 Hz), SNR > 20 dB, $\Phi_{DP0} = 70^o$. Correlation coefficient ρ_{hv}=0.98.

There is a bias of Φ_{DP} estimate in the AHV mode and its values are shown in the bottom panel in Fig. A.2.6. The bias results from large fluctuations of the estimate and some initial setting of Φ_{DP}. The system differential phase in the WSR-88D is measured with a procedure described by Zrnic et al., 2006. The initial differential phase, Φ_{DP0}, in WSR-88D is set at about 20-30°. This value prevents aliasing of differential phase at nearest cloud edges which otherwise would occur at low SNR. This value is set for SHV configuration implemented with the radars. For radar with AHV mode the aliasing interval is 180° (as opposed to 360°), the fluctuations of Φ_{DP} would be very large in the surveillance sweep (see the left panel in Fig. A.2.6) thus phase aliasing would occur regardless of Φ_{DP0}. The Φ_{DP} aliasing can cause strong biases in measured Φ_{DP}, such as shown in Fig. A.2.6 (bottom panel for $\Phi_{DP0} = 70^o$). One can see that even for such a big initial differential phase, the bias becomes large at $\sigma_v > 3$ m s^{-1}. The strong Φ_{DP} bias results in a "saturation effect" seen in the left upper panel in Fig. A.2.6 at $\sigma_v > 4$ m s^{-1}. The perturbation analysis does not account for Φ_{DP} aliasing and that's why the theoretical curve in the left panel (the red line) does not show the "saturation" effect.

A2.5. Statistics of the copolar correlation coefficient

The estimate of the modulus of correlation coefficient $\hat{\rho}_{hv}$ is calculated in the AHV mode according to (A.2.5). The Doppler correlation coefficient $\hat{\rho}(2T)$ in (A.2.5) can be estimated in the H and V channels as

$$\hat{\rho}(2T) = \frac{1}{2}[\hat{\rho}_h(2T) + \hat{\rho}_v(2T)] \text{ or } \hat{\rho}(2T) = [\hat{\rho}_h(2T)\hat{\rho}_v(2T)]^{1/2},$$

(A.2.36)

where $\hat{\rho}_h(2T)$ and $\hat{\rho}_v(2T)$ are the Doppler coefficients in the H and V channels. (36) assumes that the shapes of Doppler spectra in the channels are the same, but they are different in power which is quantified by differential reflectivity. The coefficients are calculated as follows

$$\hat{\rho}_h(2T) = \frac{\hat{R}_h(2T)}{\hat{S}_h}, \qquad \hat{R}_h(2T) = \frac{1}{M}\sum_{m=1}^{M} H^*_{2m-1}H_{2m+1},$$

$$\hat{\rho}_v(2T) = \frac{\hat{R}_v(2T)}{\hat{S}_v}, \qquad \hat{R}_v(2T) = \frac{1}{M}\sum_{m=1}^{M} V^*_{2m}V_{2m+2}. \qquad \text{(A.2.37)}$$

In the last equation in (A.2.37) it is assumed that one more pulse is added to V pulse sequences to make the number of product equal M. This is similar to the H pulse sequence shown in Fig. A.2.4 with the dash line and discussed in the previous section. Our calculations with two representations of $\hat{\rho}(2T)$ in (A.2.36) show that they are practically equal and we consider herein the second equation in (A.2.36). Then the estimate of the correlation coefficient is written as,

$$\hat{\rho}_{hv} = \frac{|\hat{R}_a| + |\hat{R}_b|}{2(\hat{S}_h \hat{S}_v)^{3/8}[\hat{R}_h(2T)\hat{R}_v(2T)]^{1/8}} . \tag{A.2.38}$$

We see that $\hat{\rho}_{hv}$ depends upon six estimates and to calculate its statistics, we have to calculate variances and covariances of six variables. That is the standard deviation of $\hat{\rho}_{hv}$ depends on six variances and fifteens covariances so the full analysis is too cumbersome hence we present herein simulation results (Fig. A.2.7). The behavior of the curves is similar to the dependences of errors in differential phase (Fig. A.2.6).
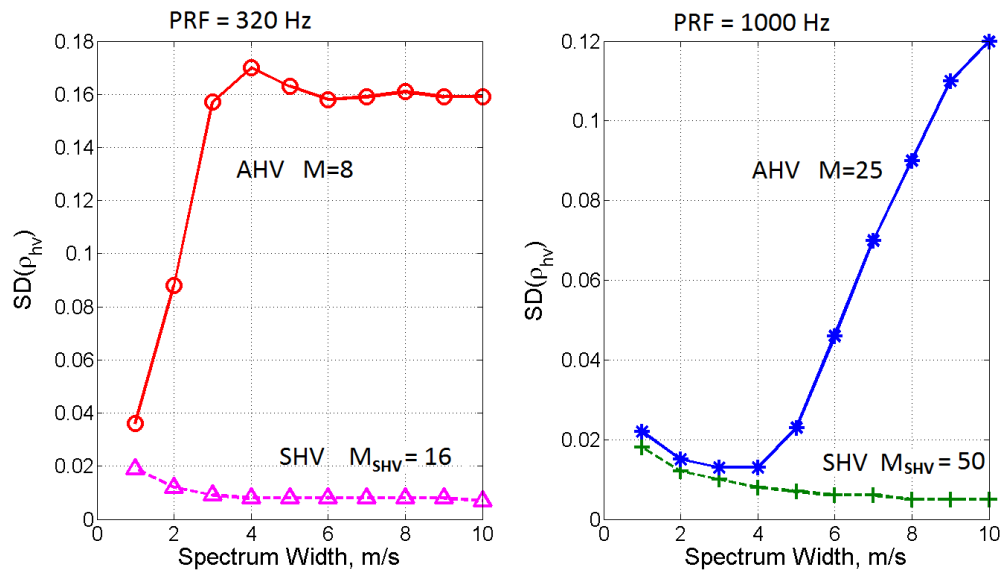

Fig. A.2.7. Standard deviation of the correlation coefficient as a function of spectrum width for AHV (circles and stars) and SHV (triangles and pluses) modes for equal dwell times. The lines approximate the simulation results. The left panel corresponds to the surveillance cut of the WSR-88D (PRF = 320 Hz) and the right panel is for the Doppler cut with PRF = 1000 Hz, SNR > 20 dB. In either case $\rho_{hv}=0.98$.

In the surveillance sweep, errors in $\hat{\rho}_{hv}$ are large at any spectrum widths (the left panel in Fig. A.2.7) so the AHV mode cannot be used for this sweep. For the Doppler mode,

errors in $\hat{\rho}_{hv}$ rapidly increase at $\sigma_v > 4$ m s^{-1} so the use of this estimate might be questioned.

The increase of SD($\hat{\rho}_{hv}$) with increasing spectrum width is not the only drawback in the AHV mode. Our simulations show significant negative biases in the estimate (Fig. A.2.8). In the surveillance sweep, the bias becomes large practically at any spectrum widths. In the Doppler sweep, the bias becomes unacceptable at $\sigma_v > 7$ m s^{-1}. The presence of biases and significant SD make the estimate problematic for using in the AHV mode.

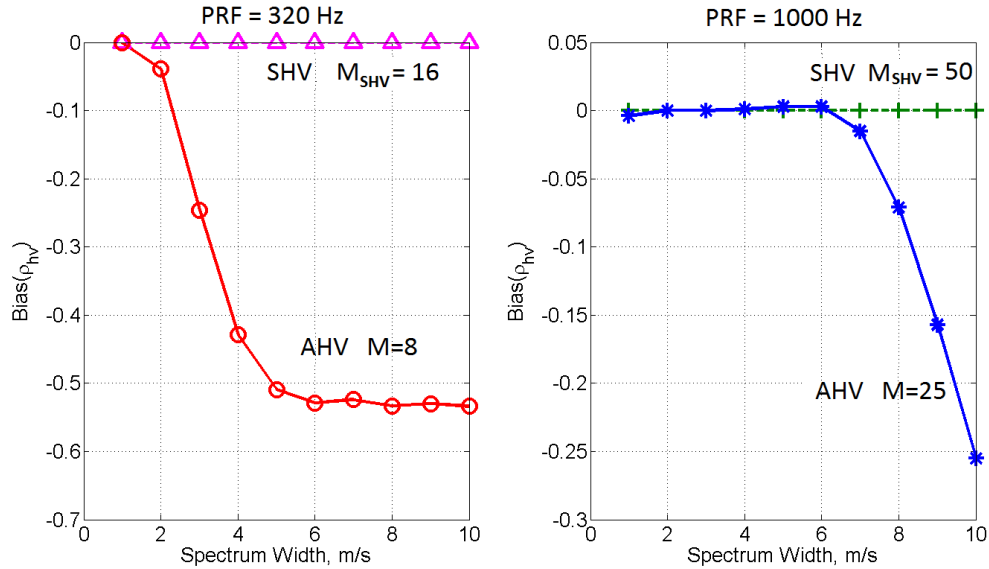Fig. A.2.8. Bias of the correlation coefficient as a function of spectrum width for AHV (circles and stars) and SHV (triangles and pluses) modes for equal dwell times. The lines connect points obtained from simulations. The left panel corresponds to the surveillance cut of the WSR-88D (PRF = 320 Hz) and the right panel is for the Doppler cut with PRF = 1000 Hz, SNR > 20 dB. In either case ρ_{hv}=0.98.

Appendix B
Spectrum Allocation

Excerpts from Chapter 5, in a National Telecommunication and Information Administration (NTIA, 2012) manual, given in this appendix contain criteria pertinent to the development of a MPAR for weather radar operations. This Appendix is for reader's convenience and should not be used in place of the NTIA manual. Of interest for MPAR designers is the possibility of transmitting multiple pulses at different center frequencies and yet be within the bounds presently allocated to the operation of the WSR-88D. The section headings below are those corresponding to the ones found in the NTIA manual. Comments inserted by the authors of this online report are printed in italic font and are not part of the NTIA manual.

5.5. Radar Spectrum Engineering Criteria (RSEC)
5.5.1 General including RSEC-A

Radars are classified in five groups A to E but the groups that concern the weather radar are B and D having the following characteristics listed in the RSEC Table.

Group B
Radars having a rated peak power of more than 1 kW but not more than 100 kW and operating between 2900 MHz and 40 GHz.

Although most WSR-88D and the FAA's ARS-9(11) radar operate in the 2700-2900 MHz band, two WSR-88Ds operate in the band 2900 to 3000 MHz. Furthermore, although the peak power transmitted by the WSR-88D is larger than 100 kW, the MPAR might use pulse compression and in this case the MPAR Group B as well as Group D criteria as described below would apply.

Criteria B ---See 5.5.2 of the NTIA manual

Group D
All fixed radars in the 2700-2900 MHz band
Criteria D ---See 5.5.4 of the NTIA manual

The WSR-88Ds principally belong to the group D of the RSEC emission criteria (only two WSR-88Ds operate in the band 2900-3000). Definition of rise time and bandwidths are presented in Figs.B.1 and B.2. Figure numbers are given to be consistent with this appendix and are not those given in the RSEC.

Pulse Characteristics and Emissions Mask

Figure 1 shows a radar pulse and where the pulse rise time (t_r) and pulse width (t) are calculated. Figure 2 shows the radar emission bandwidth and emission levels for Criteria B, C, and D.
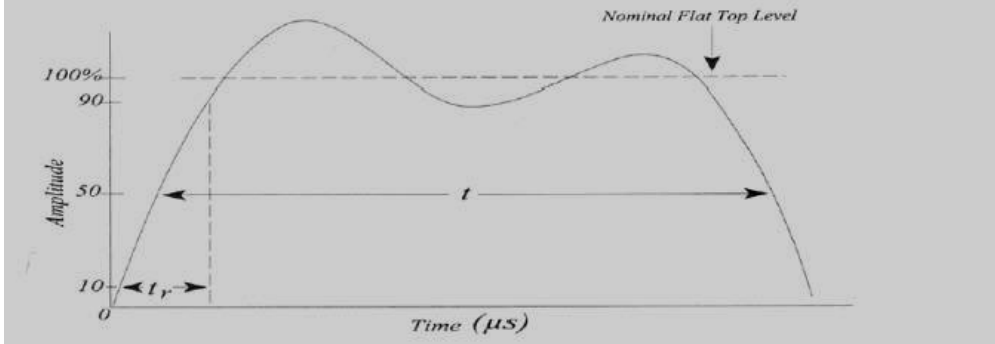

Fig. B.1 Determination of t and t_r.
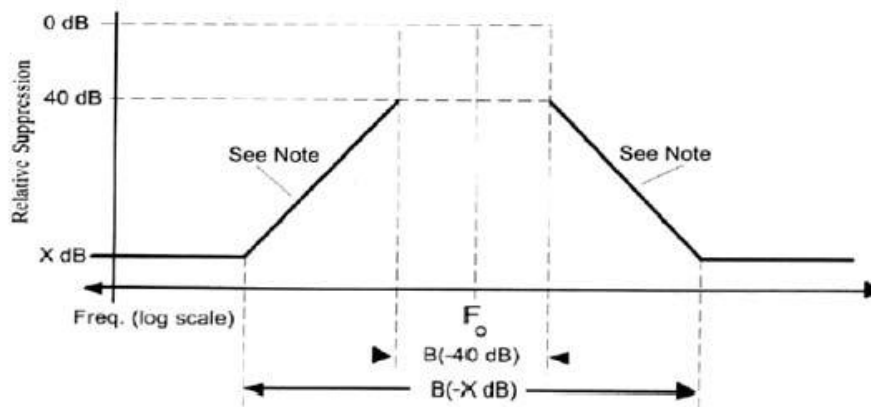
NOTE: The roll-off slope, S, from the –40 dB to -X dB points is at 20 dB per decade for Criteria B and C, and 40 to 80 dB per decade for Criteria D. The maximum emission spectrum level between the –40 dB and -X dB points for S dB per decade slope is described by the formula:

$$\text{Suppression (dB)} = - S \times \log \left| \frac{F - F_o}{\frac{1}{2}B(-40dB)} \right| - 40$$

$$\text{Where:} \quad \frac{1}{2}B(-40dB) \leq \left| F - F_o \right| \leq \frac{1}{2}B(-XdB)$$

and: F is the frequency at which suppression is calculated

and: $B(-XdB) = (10^a) B(-40dB)$

$$a = \frac{X - 40}{S}$$

Fig. B.2 Radar Emission Bandwidth and Emission Levels

Symbols Used:

B = emission bandwidth, in MHz.

Bc = bandwidth of the frequency deviation. (The total frequency shift during the pulse duration) in MHz.

Bd = bandwidth of the frequency deviation (peak difference between instantaneous frequency of the modulated wave and the carrier frequency)--(FM/CW radar systems).

Bs = maximum range in MHz over which the carrier frequency will be shifted for a frequency hopping radar.

d = pulse compression ratio = emitted pulse duration/compressed pulsed duration (at 50% amplitude points).

Fo = operating frequency in MHz. For non-FM pulse radars the peak of the power spectrum; for FM pulse radars the average of the lowest and highest carrier frequencies during the pulse.

N = total number of chips (subpulses) contained in the pulse. (N = 1 for non-FM and FM pulse radars.)

PG = processing gain (dB).

Pp = peak power (dBm).

PRR = pulse repetition rate in pulses per second.

Pt = maximum spectral power density –dBm/kHz.

t = emitted pulse duration in μ sec. at 50% amplitude (voltage) points. For coded pulses the pulse duration is the interval between 50% amplitude points of one chip (sub-pulse). The 100% amplitude is the nominal flat top level of the pulse (see Fig. 1).

tr = emitted pulse rise time in μ sec. from the 10% to the 90% amplitude points on the leading edge. See Fig.B1. For coded pulses it is the rise time of a sub-pulse; if the sub-pulse rise time is not discernible, assume that it is 40% of the time to switch from one phase or sub-pulse to the next.

tf = emitted pulse fall time in μ sec. from the 90% to the 10% amplitude points on trailing edge. See Fig.B1.

5.5.2 Criteria B

These criteria will only apply if the MPAR needs to operate in the 2900 to 3000 MHz band. These criteria are not listed here.

5.5.4 Criteria D

5.5.4.3 Radar Emission Bandwidth

The emission bandwidth for radars at the antenna input shall not exceed the following limits:

5.5.4.3.1 For Non-FM pulse radars (including spread spectrum or coded pulse radars)[3]:

$$B(-40dB) = \frac{6.2}{\sqrt{t_r t}}$$

For non-FM pulse radars a pulse rise time, t_r, or fall time, t_f, of less than $0.1t$ shall be justified.

---

[3] If t_f is less than t_r, t_f is to be used in place of t_r when performing the emission bandwidth calculation.

*For the WSR-88D having a **specified** pulse width of 1.57 μs , and a rise time of 0.15 μs , the maximum B(-40 dB) computes to be 12.78 MHz. This emission bandwidth at the -40 dBc level satisfies the required maximum allowed 14.5 MHz bandwidth stipulated in an NWS document (ROC, 2012, p.5-216).*

5.5.4.3.2 For FM-pulse radars (intentional FM)[3]:

$$B(-40dB) = \frac{6.2}{\sqrt{t_r t}} + 2(B_c + \frac{0.105}{t_r})$$

For FM pulse radars with pulse rise time, t_r, or fall time, t_f, of less than 0.1 microsecond, an operational justification for the short rise time shall be provided.

5.5.4.3.3 For FM pulse radars (intentional FM) with frequency hopping[3, 4]:

For FM pulse radars (intentional FM) with frequency hopping, but with pulse rise time, tr, of less than 0.1 microsecond, an operational justification for the short rise time shall be provided.

$$B(-40dB) = \frac{6.2}{\sqrt{t_r t}} + 2(B_c + \frac{0.105}{t_r}) + B_s$$

5.5.4.3.4 For frequency hopping radars using non-FM pulses (including spread spectrum or coded pulses)[3, 4]:

$$B(-40dB) = \frac{6.2}{\sqrt{t_r t}} + B_s$$

For this category of radars, an operational justification shall be provided if the pulse rise time, t_r, is less than 0.01 microseconds.

The following 4 paragraphs show that, given the RSEC maximum allowed 14.5 MHz bandwidth at the -40 dBc level, and using the criterion given in this section, we could transmit 3 shaped pulses at three different center frequencies that fit within the maximum allowed bandwidth. This should permit nearly simultaneous transmission of these three frequencies along three beams in different directions and simultaneous reception from these directions effectively giving us three radars in one! Alternatively it could provide us with 3 independent estimates of meteorological parameters along a single beam which also could speed up data acquisition.

As an example, assume non-frequency hopping radar such as the WSR-88D, a rise time of 0.15 μs , and a transmitted pulse width of 1.57 μs . Then the criteria of section 5.5.4.3.1 applies and B(-40 dBc) computes to be about 12.78 MHz. Although a pulse

---

[4] These formulas yield the total composite B(-40 dB) bandwidth of a frequency hopping radar as if all channels included within B_s were operating simultaneously. Individual channels have a B(-40 dB) radar emission bandwidth given by the equations in paragraphs 5.5.4.3.1 or 5.5.4.3.2 of sections 5.5.2, 5.5.3, and 5.5.4.

with this rise time meets the constraints imposed by the NTIA, we cannot add other pulses at different center frequencies.

However, if the shape of the pulse is such that a longer rise time is achieved, then the pulse bandwidth for the pulse is less and two or more pulses at different center frequencies can be transmitted without exceeding the maximum allocated bandwidth.

For example, if the transmitted pulse has a half cosine amplitude shape, the rise time computes to be 0.487t. Thus for the t = 1.57 μs pulse width transmitted by the WSR-88D in the short pulse mode, the first term in the above equation computes to be about 5.7 MHz. Assume echo samples are independent if the echoes are from a pair of transmitted pulses having frequency separation equal to or greater than their bandwidth at the -40 dB level. For a half cosine pulse, it is shown the emission bandwidth at the -40 dB level is about 3.6 MHz (Murray, 1970)[5]. It can be shown that a 3 pulse spectrum, evenly spaced 4.4 MHz in the bandwidth of 14.5 MHz, satisfies the RSEC allocated maximum bandwidth. That is,

$$B(-40dB) = \frac{6.2}{\sqrt{t_r t}} + B_s = 5.7 + 2 \times 4.4 = 14.5 \text{ MHz}$$

It is concluded that by transmitting and receiving pulses at F_0s separated by 4.4 MHz each along separate directions, data acquisition time can be reduced by a factor of three. Furthermore, having a separation of 4.4 instead of 3.6 MHz, there is more independence between echo samples from the three transmitted frequencies.

5.5.4.4 Emission Levels[6]

5.5.4.4.1 With the exception of CW and FM/CW radars, the radar emission level at the antenna input shall be no greater than the values obtainable from the curve In Figure B2. At the frequencies $\pm$ B(-40 dB)/2 displaced from f_0 the level shall be at least 40 dB below the maximum value. Beyond the frequencies $\pm$ B(-40 dB)/2 from f_0, the emission level(s), with the exception of harmonic frequencies, shall be below the 40 dB per decade (S = 40) roll-off lines in Fig.B2 down to a -X dB level that is 80 dB below the maximum spectral power density. All harmonic frequencies shall be at a level that is at least 60 dB below the maximum spectral power density.

---

[5] Murray, J. P., 1970: Electromagnetic Compatibility. Chapter 29 in "Radar Handbook", Skolnik, Ed., McGraw Hill, NY.

[6] For frequency hopping radars, the radar spectrum shall not intrude into adjacent spectrum regions of the high or low side of the allocation band, defined by B_s, more than would occur if the radar were fixed tuned at carrier frequencies equivalent to the end values of B_s and was complying with the constraints given by paragraphs 4.1 and 4.2 of Sections 5.5.2 and 5 .5.4.

Appendix C

Matched filter and Pulse compression

Because the WSR-88D uses a matched filter receiver, and because the MPAR might be using pulse compression, the detection capability of a radar using pulse compression is compared to one using a matched filter.

First define a short unit duration τ_u to be used to measure the lengths of a pulse to which a matched filter is applied, i.e., $\tau_m = k\tau_u$ (where k is a multiplying factor which need not be an integer). The τ_u will also be the length of the compressed pulse.
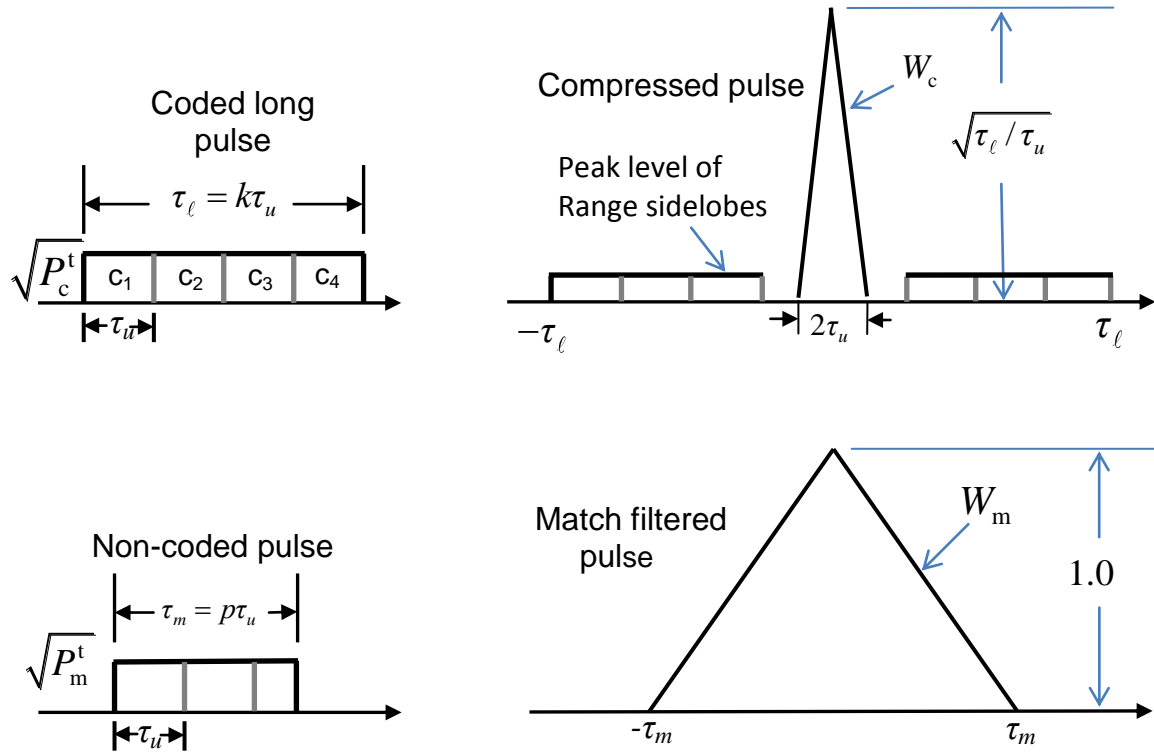

Fig. C.1 Conceptual drawings. top: a long pulse and its compressed shape. bottom: A non-coded pulse and its response at the output of a matched filter. The shapes on the right are also the voltage range-weighting functions.

Consider the matched filter case and a rectangular pulse as in Fig. C.1. The voltage amplitude weighting function at the output of the matched filter has triangular shape and the linear (right part with origin shifter to $-\tau_m$ to simplify integration) has the dependence between 0 and τ_m given by

$$W_m = \frac{t}{\tau_m} \tag{C.1}$$

To shorten notation we will use mainly the range-time (t and τ) rather than distance in the equations and discussion. We assume uniform reflectivity η (per unit range-time) so that the integral under the range weighting function is proportional to the received power. The

integral of W_m^2 between (0 and τ_m) multiplied by 2 (because of symmetry) produces the power P_{m} at the output of the matched filter. That is

$$P_{\mathrm{m}} \propto 2P_m^t \eta \int_0^{\tau_m} W_m^2 dt = 2P_m^t \eta \int_0^{\tau_m} \frac{t^2}{\tau_m^2} dt = \frac{2}{3} P_m^t \tau_m \eta \ . \tag{C.2}$$

In (C.2) peak transmitted power is P_m^t and other terms that appear in the radar equation are ignored as they have no bearing on the results.

Next consider the long coded pulse. Assume after pulse compression the voltage range-weighting function W_c has a triangular shape (as in Fig. C.1) and base width of $2\tau_u$. Note that the impulse response function for pulse compression must have a width approximately equal to τ_u, i.e., it is inversely proportional to the bandwidth of the coded pulse. From this and power considerations one can obtain the range-weighting function. The range sidelobes are ignored in the subsequent computations. Then like in the matched filter case let's shift the origin to $-\tau_u$ so that the right side of the range weighting function can be expresses as

$$W_{\mathrm{c}} = \sqrt{\frac{\tau_\ell}{\tau_u}} \frac{t}{\tau_u} \ . \tag{C.3}$$

Integration of W_c^2 between 0 and τ_u and multiplication by 2 and by appropriate parameters produces the power P_c from scatterers within the range weighting function.

$$P_{\mathrm{c}} \propto 2P_c^t \eta \int_0^{\tau_u} |W_{\mathrm{c}}|^2 dt = \frac{2}{3} P_c^t \eta \tau_\ell \ . \tag{C.4}$$

Of interest is the ratio of SNRs for the matched filter and compressed pulse. Let these be denoted with SNR_{m} and SNR_{c}. The receiver bandwidth for the matched pulse is $1/\tau_{\mathrm{m}}$ and the bandwidth for the coded pulse must be $1/\tau_{\mathrm{u}}$ to achieve this compression at both the transmitter side and the receiver. The white noise powers are proportional to these bandwidths and thus the ratio of SNRs becomes

$$\frac{SNR_{\mathrm{m}}}{SNR_{\mathrm{c}}} = \frac{P_{\mathrm{m}}^t}{P_{\mathrm{c}}^t} \frac{\tau_m^2}{\tau_\ell \tau_u} \ . \tag{C.5}$$

This compact equation is relevant for comparing performance of pulse compression (on MPAR) with the current matched filter on the WSR-88D. It is very convenient because it relates the transmitted powers to pulse durations and it is applicable to single pulse sensitivity comparisons.

References

AL-Rashid, Y., R. Nuthalapati, F.X. McGreagy, D., Kryzak and S. Bachman, 2012: Improving cross polarization for MPAR via orthogonal waveforms. 28th Conference on Interactive Information Processing Systems (IIPS), Poster at AMS annual meeting, New Orleans, LA.

Aumann, H. M., A. J. Fenn, and F. G. Willwerth, 1989: Phased Array Antenna Calibration and Pattern Prediction Using Mutual Coupling Measurements, IEEE Trans. on Antennas and Prop., **37,** July, 844-850.

Balanis, C. A., 2005: *Antenna Theory- analysis and design*. 3nd edition, John Wiley & Sons, Inc., Hoboken, New Jersey, 1117 pp.

Brandes, E., G. Zhang, and J. Vivekanandan, 2003: An evaluation of a drop distribution-based rainfall estimator, J. Appl. Meteor., 42(5), 652-660.

Bringi, V. N., R. Hoferer, D. A. Brunkow, R. Schwerdtfeger, V. Chandrasekar, S. A. Rutledge, J. George, P. C. Kennedy, 2011: Design and Performance Characteristics of the New 8.5-m Dual-Offset Gregorian Antenna for the CSU–CHILL Radar. *J. Atmos. Oceanic Technol.*, **28**, 907–920. doi: http://dx.doi.org/10.1175/2011JTECHA1493.1

Brookner, E., Editor, 1988: *Aspects of Modern Radar.* Artech House, Boston, MA. 574 pp.

Brookner, E., 2006: Phased Arrays and Radars--- Past, Present and Future. *Microwave Jo.*, 24-46.

Brunkow, D. V. N. Bringi, P. C. Kennedy, S. A. Rutledge, V. Chandrasekar, E. A. Mueller, and R. K. Bowie, 2000: A Description of the CSU-CHILL National Radar Facility, *J. Atmos. and Oceanic Tech.,* **17,** 1596-1608.

Bucci, J. N., H.S. Owen, K.A. Woodward, and C.M. Hawes, 1997: Validation of pulse compression techniques for meteorological functions. IEEE Tr. Geosci. Remote Sens., **35,** 507-523.

Cho, J. and S. Duffy, 2011: Multifunction Phased Array Radar (MPAR). MIT Lincoln Laboratory Report, July, 21 pp.

Curtis, C. D., 2009: Exploring the capabilities of the agile beam phased array weather radar. Dissertation, The Graduate College, University of Oklahoma, Norman, OK. 187 pp.

Curtis, C. D. and J. Meier "National Weather Radar Testbed *Antenna Pattern Measurement (2010-B)* ,National Severe Storms Laboratory Internal Repot Memo, December 3, 2009, 27pp.

DiFranco, J.V., and W.L. Rubin 1980: Radar Detection. Artech House. p. 654.

Doviak, R. J., and D. S. Zrnić, 2006: *Doppler Radar and Weather Observations*, Dover Publications, 562 pp.

Doviak, R. J., and D. S. Zrnić, 1998: WSR-88D Radar for Research and Enhancement of Operations: Polarimetric Upgrades to Improve Rainfall Measurements NOAA/NSSL Report, 110 pp.

Doviak, R. J., V. Bringi, A. Ryzhkov, A. Zahrai, and D. S. Zrnić, 2000: Considerations for Polarimetric Upgrades to Operational WSR-88D Radars. *Jo. Atmos. and Oceanic Tech.*, **17,** March, 257-278.

Doviak, R. J., L. Lei, G. Zhang, J. Meier, and C. Curtis, 2011: Comparing Theory and Measurements of Cross-polar Fields of a Phased-Array Weather Radar. *IEEE Geosci. & Remote Sens. Ltrs.*, **8**, 1002-1006.

Fang, M., R.J. Doviak, and V. Melnikov, 2004: Spectrum width measured by WSR-88D: error sources and statistics of various weather phenomena. *Jour. Atmos. Oceanic Technol.,* **21,** 888-904.

Galletti, M., and D. S. Zrnić, 2011: Bias in copolar correlation coefficient caused by antenna radiation patterns. *IEEE Trans. Geosci. Remote Sens.,* **49,** 2274-2284.

Heinselman, P. L., and S. M. Torres, 2011: High-temporal resolution capabilities of the National Weather Radar Testbed phased-array radar. *Jo. Appl. Meteor. and Climat.,* **50**, 579-593.

Heinselman, P. L., D. L. Priegnitz, K. L. Manross, T. M. Smith, and R. W. Adams, 2008: Rapid sampling of severe storms by the National Weather Radar Testbed phased-array radar. *Weather and Forecast.* Amer. Meteor. Soc., **23**, 808-824.

Hopf, A., J. L. Salazar, R. H. Medina, V. Venkatesh, E. J. Knapp, S. Fraiser, and D. J. McLaughlin, 2009: CASA Phased Array System Description, Simulation and Products. IEEE International Symposium on Geoscience and Remote Sensing, Cape Town, South Africa.

Hubbert, J.C., V.N. Bringi, and D. Brunkow, 2003: Studies of the polarimetric covariance matrix. Part I: Calibration methodology. *J. Atmos. Oceanic Technol.*, **20,** 696-706.

Hubbert J., S. M. Ellis, M. Dixon, and G. Meymaris, 2010: Modeling, Error Analysis, and Evaluation of Dual-Polarization Variables Obtained from Simultaneous Horizontal and Vertical Polarization Transmit Radar. Part I and II. *J. Atmos. Oceanic Technol.* **27**, 1583-1607.

Jones, E. M. T., 1954: Paraboloid Reflector and Hyperboloid Lens Antennas, *IRE Trans. Antennas & Prop.*, July, pp.119-127.

Jordan, E. C. and K. G. Balmain, 1968: *Electromagnetic Waves and Radiating Systems*, Prentice Hall, Inc., Englewood Cliffs, NJ, 753 pp.

Jung, Y., G. Zhang, and M. Xue, 2008a: Assimilation of simulated polarimetric radar data for a convective storm using ensemble Kalman filter. Part I: Observation operators for reflectivity and polarimetric variables. Mon. Wea. Rev., 136(6), 2228–2245.

Jung, Y., M. Xue, G. Zhang, and J. Straka, 2008b: Assimilation of simulated polarimetric radar data for a convective storm using ensemble Kalman filter. Part II: Impact of polarimetric data on storm analysis. Mon. Wea. Rev., 136(6), 2246–2260.

Jung, Y., M. Xue, and G. Zhang, 2010a: Simulations of polarimetric radar signatures of a supercell storm using a two-moment bulk microphysics scheme. J. Appl. Meteor. Climat., 49(1), 146-163.

Jung, Y., M. Xue, and G. Zhang, 2010b: Simultaneous estimation of microphysical parameters and atmospheric state using simulated polarimetric radar data and ensemble Kalman filter in the presence of observation operator error. Mon. Wea. Rev., 138(2),539-562.

Lei L., G. Zhang, and R. J. Doviak, 2012: Bias Correction for Polarimetric Phased-Array Radar with Idealized Aperture and Patch Antenna Elements. Accepted by the IEEE Trans. Geosci, and Remote Sensing.

Lei L., G. Zhang, and R. J. Doviak, 2012: Theoretical Analysis of Polarization Characteristics for Planar and Cylindrical Phased Array Radars. AMS General Meeting in New Orleans, January, 2012.

Liu, L., V.N. Bringi, V. Chandrasekar, E.A. Mueller, and A. Mudukutore, 1994: Analysis of the copolar correlation coefficient between horizontal and vertical polarizations. *J. Atmos. Oceanic Technol.* **11**, 950 – 963.

Ludwig, A. C., 1973: The Definitions of Cross Polarizations, *IEEE Trans. on Antennas and Propagation,* Jan., pp.116-118.

Maese, T., J. Melody, M. Kobil, and T. McNellis, 2001: At-sea collection of environmental data using a tactical shipborne phased array radar.   Integrated Observing Systems – 5th symposium, AMS, Albuquerque, NM.

Matrosov S.Y., R. F. Reinking, R. A. Kropfli, et al 2001: On the use of radar depolarization ratios for estimating shapes of ice hydrometeors in winter clouds, *Journal of Applied Meteorology*, 40(3), 479-490

Melnikov, V., and D. S. Zrnic, 2004: Simultaneous transmission mode for the polarimetric WSR-88D: Statistical biases and standard deviations of polarimetric variables. NOAA/NSSL Interim report. 83 pp. (Available online at www.cimms.ou.edu/~schuur/jpole/WSR-88D_reports.html).

Melnikov, V. M., and D. S. Zrnić, 2007: Autocorrelation and cross-correlation estimators of polarimetric variables. *J. Atmos. Oceanic Technol*., **24,** 1337-1350.

Meymaris, G., J. K. Williams, and J. C. Hubbert (2009): Performance of a proposed hybrid spectrum width estimator for the NEXRAD ORDA. 25th International Conference on Interactive Information and Processing Systems for Meteorology, Oceanography and Hydrology, AMS, Phoenix, AZ, USA.

McLaughlin, D. J., E. A. Knapp, Y. Wang, and V. Chandrasekar, 2009: Distributed Weather Radar Using X-Band Active Arrays. IEEE A&E Systems Magazine, July, 21-26.

NTR, 1991: NEXRAD Technical Requirements, NEXRAD Joint System Program Office (SPO1), Silver Spring, MD.

NTIA, 2012: Manual of Regulations and Procedures for Federal Radio Frequency management (Red book), Chapter 5 "Spectrum Standards" 36 pp. www.ntia.doc.gov/

Nusrat, Y. and D. J. Stensrud, 2010: Impact of Phased-Array Radar Observations over a Short Assimilation Period: Observing System Simulation Experiments Using an Ensemble Kalman Filter. *Mon. Wea. Rev.*, **138**, 517–538. doi: http://dx.doi.org/10.1175/2009MWR2925.1

NSSL, 1997-2012: Reports on Signal Design and Processing Techniques for WSR-88D Ambiguity Resolution, Parts 1-15. http://cimms.ou.edu/rvamb/reports.htm

Randall, M., J. Lutz, and J. Fox, 1997: S-POL's High Isolation Mechanical Polarization Switch. 28th *Conference on Radar Meteorology*. Austin, TX, AMS, Boston, MA. 252-253.

ROC, 2006: Critical Item Development Specification for Transmitter (B2, CI-03). Document No. 2830003 Pt.1, WSR-88D Radar Operations Center (ROC), 2227 W. Lindsey St., Suite 1500, Norman, OK 73069.

ROC, 2012: Technical Manual; Operations and Maintenance Instructions; Transmitter System, change 7, NWS EHB 6-511, 15 June 2012, 819 pp. Document available from Radar Operations Center (ROC) Norman, OK.

Ryzhkov, A. V., S. E. Giangrande, V. M. Melnikov, and T. J. Schuur, 2005a: Calibration issues of dual-polarization radar measurements. *J. Atmos. Oceanic, Technol.,* **22,** 1138-1155.

Sachidananda, M,, and D. S. Zrnić, 1985: ZDR measurement consideration for a fast scan capability radar. *Radio Sci.*, **20**, 907-922.

Sachidananda, M., and D. S. Zrnić, 1989: Efficient processing of alternately polarized radar signals. *J. Atmos. Oceanic Technol.* **6**, 235–247.

Salazar J. L., E. J. Knapp, R. H. Medina, A. P. Hopf, and D. J. McLaughlin, 2010: Scanning Performance of the CASA Solid State Phase-Tilt Radar Antenna Array. IEEE Inter. Symp. on Phased Array Systems and Technology., 8pp.

Seliga, T.A., and V.N. Bringi, 1976: Potential use of radar differential reflectivity measurements at orthogonal polarizations for measuring precipitation. *J. Applied Meteor.*, **15**, 69-76

Smith, P.L, 1986: On the sensitivity of weather radars. *Jour. Atmos. Oceanic Technol.*,**3,** 704-713.

Smith, P., J. Davis, E. Im, J. Lazo, D. McLaughlin, R. Palmer, S. Rutledge, S. Sandgathe, R. Serafin, M. Wolfson, C. Marshall, 2008: Evaluation of the Multifunction Phased Array Radar Planning Process, *National Research Council Report*, August.

Torres, S., C. D. Curtis, and J. R. Cruz, 2004: Pseudo whitening of weather radar signals to improve spectral moment and polarimetric variable estimates at low signal-to-noise. *IEEE Trans. Geosci. Remote Sens*., **42,** 941–949.

Torres, S., S. Bachman, and D. S Zrnic, 2007: Signal design and processing techniques for wsr-88d ambiguity resolution: Staggered PRT and updates to the SZ-2 algorithm. National Severe Storms Laboratory Report part 11. p. 146. Available at, http://cimms.ou.edu/rvamb/Documents/Report_11.pdf

TRMM Data User Handbook. Earth Observation Center, National Space Development Agency of Japan [Available online at http://www.eorc.jaxa.jp/TRMM/document/text/handbook_e.pdf].

Whalen, A.D., 1971. *Detection of signals in noise*. Academic Press. 411 pp.

Weadon, M., P. L. Heinselman, D. Forsyth, W. E. Benner, G. S. Torok, and J. Kimpel, 2009: Multifunction phased-array radar. *Bull. Amer. Meteor. Soc.*, **90**, 385-389.

Weber, M. E., J. Y. N. Cho, J. S. Herd, J. M. Flavin, W. E. Benner, and G. S. Torok, 2007: The next generation multi-mission U. S. Surveillance radar network. *Bull. Amer. Meteor. Soc.*, **88**, 1739-1751.

Wolfson, R. I., and C. F. Cho, 1980: A wideband low-sidelobe, polarization agile array antenna. *IEEE International Radar Conf.* Arlington, VA. 284-287.

Wurman, J. and M. Randall, 2001:"An inexpensive, mobile, rapid-scan radar," *30th International Conference on Radar Meteorology.*, P3.4.

Yu, Tian-You, M. Orescanin, D. S. Zrnić, and D. Forsyth, 2007: Beam Multiplexing Using the Phased-Array Weather Radar, *J. Atmos. Oceanic Technol.* **24**, 616–626.

Zahrai, A., and D. S. Zrnić, 1993: The 10-cm-wavelength polarimetric weather radar at NOAA's National Severe Storms Laboratory. *Jour. Atmos. Oceanic. Technol.,***10,** 649-662.

Zhang, G., and R. J. Doviak, 2007: Spaced-Antenna Interferometry to Measure Crossbeam Wind, Shear, and Turbulence: Theory and Formulation. *Jo. Oceanic and Atmos. Tech.*, Nov. 791-804. DOI: 10.1175/JTECH2004.1

Zhang, G., and R. J. Doviak, 2008: Spaced-Antenna Interferometry to Detect and Locate Sub-Volume Inhomogeneities of Reflectivity: An Analogy with Monopulse Radar. *Jo. Oceanic and Atmos. Tech.*, Nov. 1921-1938. DOI: 10.1175/2008JTECHA1055.1

Zhang, G., J. Sun, and E. A. Brandes, 2006: Improving parameterization of rain microphysics with disdrometer and radar observations. J. Atmos. Sci., 63 (4): 1273-1290.

Zhang, G., R. J. Doviak, D. S. Zrnić, J. Crain, D. Staiman, and Y. Al-Rashid, 2009: Phased Array Radar Polarimetry for Weather Sensing: A Theoretical Formulation for Bias Corrections. *IEEE Trans. Geo. Sci.& Remote Sens.***47**, 3679-3689.

Zhang, G., Y. Li, R. J. Doviak, D. Priegnitz, J. Carter, and C. Curtis, 2011a: Multi-patterns of the National Weather Radar Testbed Mitigate Clutter Received via Sidelobes, *J. Atmos. Ocean. Tech.,* **28**(3), 401-409.

Zhang, G., R. J. Doviak, D. S. Zrnić, R. Palmer, Lei Lei, and Y. Al-Rashid, 2011b: Polarimetric Phased-Array Radar for Weather Measurement: A Planar or Cylindrical Configuration? *Jo. Oceanic and Atmos. Tech.*, Jan. 63-73. DOI: 10.1175/2010JTECHA1470.1

Zhang, P., D. Zrnić, and A. Ryzhkov, 2012: Partial beam blockage correction using dual-polarization measurements. Submitted *J. Atmos. Oceanic Technol.,*

Zrnić, D.S., 1991: Complete polarimetric and Doppler measurements with a single receiver radar. *J. Atmos. Oceanic Technol.* **8**, 159-165.

Zrnić, D.S., 2007: Phase codes for separation of range overlaid echoes. Poster at the 33rd International Conference on radar meteorology, Cairns, Australia, AMS.

Zrnić, D. S., and R. J. Doviak, 2005: System Requirements for Phased Array Weather Radar. NSSL report 23 pp. http://publications.nssl.noaa.gov/mpar_reports/

Zrnić, D.S., V. M. Melnikov, and A.V. Ryzhkov, 2006: Correlation coefficients between horizontally and vertically polarized returns from ground clutter. *J. Atmos. Oceanic Technol,.***23**, 381-394.

Zrnić, D.S., V.M. Melnikov, and J.K. Carter, 2006: Calibrating differential reflectivity on the WSR-88D. *J. Atmos. Oceanic Technol.* **23**, 944-951.

Zrnić, S.D., V.M. Melnikov, and I. Ivic, 2008: Processing to obtain polarimetric variables on the ORDA. NSSL report: Do not destroy – version, pp.54. http://publications.nssl.noaa.gov/wsr88d_reports/

Zrnić, D. S., G. Zhang, R. J. Doviak, 2011: Bias Correction and Doppler Measurement for Polarimetric Phased-Array Radar. *IEEE Trans. Geo. Sci.& Remote Sens.***49**, 843-853.

Zrnić, D.S., N. Balakrishnan, A. V. Ryzhkov, and S. Durden, 1991: Use of copular correlation coefficient for probing precipitation at nearly vertical incidence. IEEE Trans. GRS*,* **32**, 740-748.

Zrnić, D., S., V. M. Melnikov, J. K. Carter, and I. Ivic, 2007: Calibrating Differential Reflectivity on the WSR-88D, Part II (.doc, 331 kB), NOAA/NSSL Report, 16 pp. (updated 27 Nov 2007)

Zrnić, D. S., R. J. Doviak, G. Zhang, and A. Ryzhkov, 2010: Bias in differential reflectivity due to cross-coupling through the radiation patterns of polarimetric weather radars, *J. Atmos. Oceanic Technol.,* **27,** 1624-1637.

Zrnić, D. S., Kimpel, J. F., Forsyth, D. E., Shapiro, A., Crain, G., Ferek, R., Heimmer, J., Benner, W., McNellis, T. J. and Vogt, R. J., 2007: Agile-beam Phased array radar for weather observations. *Bull. Amer. Meteor. Soc.,* **88**, 1753-1766.